

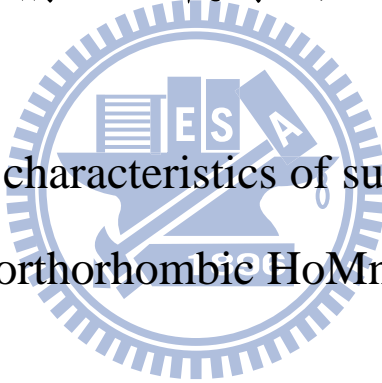
國立交通大學

電子物理系所

博士論文

多鐵性正交結構欽錳氧薄膜之磁電特性研究

Magnetoelectric characteristics of substrate-stabilized
multiferroic orthorhombic HoMnO_3 thin films



研究生：林宗漢

指導教授：莊振益 教授

中華民國九十九年七月

多鐵性正交結構欽錳氧薄膜之磁電特性研究
Magnetoelectric characteristics of substrate-stabilized
multiferroic orthorhombic HoMnO_3 thin films

研究生：林宗漢

Student : Tjung-Han Lin

指導教授：莊振益教授

Advisor : Prof. Jenh-Yih Juang

國立交通大學

電子物理系所

博士論文



A Dissertation
Submitted to Department of Electrophysics
College of Science

National Chiao Tung University
in Partial Fulfillment of the Requirements
for the Degree of
Doctor of Philosophy

in

Electrophysics

July 2010

Hsinchu, Taiwan, Republic of China

中華民國九十九年七月

多鐵性正交結構鈦錳氧薄膜之磁電特性研究

研究生：林宗漢

指導教授：莊振益 教授

國立交通大學

電子物理系所

中文摘要

本論文主要研究具有 *E-type* 反鐵磁有序磁結構之多鐵性正交結構鈦錳氧薄膜之磁有序誘發鐵電特性等物理性質。我們首先以固態燒結法製備出具有六方結構的稀土元素錳氧化物（離子半徑較小之鈦元素）；並利用 X-ray 繞射儀及超導量子干涉儀(SQUID)來分析靶材之晶體結構與磁相變等特性。另一方面，為了探索其正交結構磁電耦合之基本物理特性，本研究乃以製備具良好晶軸取向之薄膜為初期之首要目標。實驗結果顯示藉由選擇鈦酸鋇(110)、鋁鋁氧(110)、與鈦酸鋇(100)三種基板，我們可分別製備出具單一軸向之 *a*、*b*、與 *c* 軸薄膜；除此之外，亦藉由上述匹配之基板來調變鈦錳氧薄膜正交結構之晶格常數，進而利用這些薄膜來進行相關磁電特性的量測以確認磁電耦合的機制是否存在，並與理論預測做比較。

Magnetoelectric characteristics of substrate-stabilized multiferroic orthorhombic HoMnO_3 thin films

Student: Tjung-Han Lin

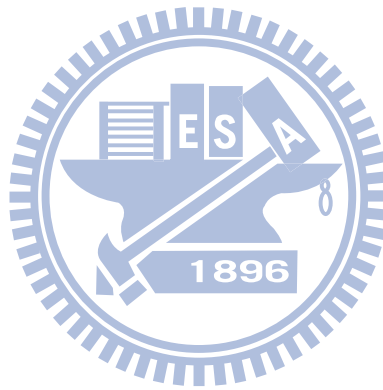
Advisor: Prof. Jenh-Yih Juang

Department of Electrophysics
National Chiao Tung University



This dissertation is aimed primarily at exploring the manifestations of magnetic ordering induced ferroelectricity expected in the E -type multiferroic orthorhombic HoMnO_3 . We first prepare the hexagonal HoMnO_3 bulk synthesized by conventional solid-state reaction processes. The structural and magnetic characteristics of these samples were examined by x-ray diffraction and superconducting quantum interference device (SQUID) to ensure the stoichiometry of the material. Since within the frameworks of various microscopic mechanisms the magnetic ordering and associated ferroelectricity are intimately related to specific crystallographic orientations, it is thus essential to obtain well-aligned orthorhombic HoMnO_3 (o -HMO) thin films capable of revealing the relevant properties along respective crystallographic orientations. To this respect, we have carefully calculated the in-plane lattice mismatch and chose $\text{SrTiO}_3(110)$, $\text{LaAlO}_3(110)$, and $\text{SrTiO}_3(100)$ as the substrates for preparing the a -, b -,

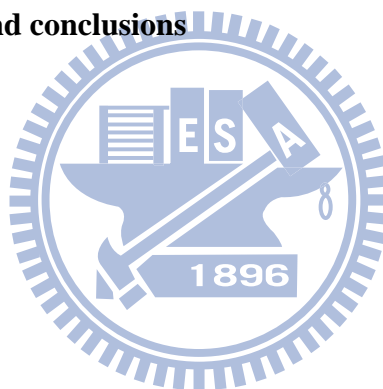
and c -axis-oriented o -HMO thin films. Moreover, the external strain force originated from the epitaxial relation between these substrates and thin films during deposition can also serve as an excellent method in slightly modifying the lattice parameters with desired crystal structures. Finally, the magnetic ordering anisotropy and the ferroelectricity in these epitaxial o -HMO thin films were investigated to check whether or not the predicted marked enhancement of the magnetoelectric effect does indeed exist in these E -type multiferroic perovskite manganites.



Contents

| | |
|---|----|
| Abstract (in Chinese) | i |
| Abstract (in English) | ii |
| Contents | iv |
| List of Figures | vi |
| Chapter 1 Introduction | 1 |
| 1.1 The discovery of manganites with gigantic magnetoelectric effect | 1 |
| 1.2 Origin of the magnetism-induced ferroelectricity in multiferroic orthorhombic $RMnO_3$ | 6 |
| 1.2.1 Spiral magnetism | 6 |
| 1.2.2 Collinear magnetism | 9 |
| 1.3 Survey of the magnetic phase diagram versus R^{3+} -ion radius in the perovskites $RMnO_3$ family | 11 |
| 1.4 Motivation | 13 |
| 1.5 Organization of this dissertation | 15 |
| References | 16 |
| Chapter 2 Exchange interactions and environmental effects in perovskite manganites | 18 |
| 2.1 Introduction | 18 |
| 2.2 Superexchange | 18 |
| 2.3 Double exchange | 19 |
| 2.4 Crystal field and Jahn-Teller effect | 21 |
| 2.5 Tolerance Factor and E -phase magnetic structure | 23 |
| References | 26 |
| Chapter 3 Experimental procedures | 27 |
| 3.1 Preparation and characterization of polycrystalline sample of hexagonal $HoMnO_3$ | 27 |
| 3.1.1 Introduction | 27 |
| 3.1.2 Experimental | 28 |
| 3.1.3 Results and discussion | 28 |
| 3.2 Epitaxial stabilization of oxide thin films | 32 |
| 3.2.1 The b -axis-oriented o - $HoMnO_3$ thin films | 35 |
| 3.2.2 The c -axis-oriented o - $HoMnO_3$ thin films | 36 |
| 3.2.1 The a -axis-oriented o - $HoMnO_3$ thin films | 36 |
| References | 38 |
| Chapter 4 Magnetoelectric properties of orthorhombic $HoMnO_3$ thin films with various orientations | 40 |
| 4.1 Anomalous magnetic ordering in b -axis-oriented $HoMnO_3$ thin films | 40 |
| 4.1.1 Probing the anisotropic characterization of orthorhombic $HoMnO_3$ thin films | 40 |
| 4.1.2 Results and Discussion | 41 |
| 4.1.3 Summary | 45 |

| | | |
|------------------|---|----|
| 4.2 | Strain-induced effects on antiferromagnetic ordering and magnetocapacitance in orthorhombic HoMnO ₃ thin films | 46 |
| 4.2.1 | Directly probing the magnetoelectric coupling in orthorhombic HoMnO ₃ thin films | 46 |
| 4.2.2 | Results and Discussion | 48 |
| 4.2.3 | Summary | 54 |
| 4.3 | Magnetism-induced ferroelectric polarization in the <i>c</i> -axis-oriented orthorhombic HoMnO ₃ thin films | 55 |
| 4.3.1 | Introduction | 55 |
| 4.3.2 | Results and Discussion | 57 |
| 4.3.3 | Summary | 63 |
| 4.4 | Magnetic and electric properties of the <i>a</i> -axis-oriented orthorhombic HoMnO ₃ thin films | 64 |
| 4.4.1 | Introduction | 64 |
| 4.4.2 | Results and Discussion | 65 |
| 4.4.3 | Summary | 72 |
| | References | 73 |
| Chapter 5 | Summary and conclusions | 76 |
| | Biographical notes | 78 |
| | Acknowledgements | 80 |



List of Figures

- | | | |
|----------|--|----|
| Fig. 1.1 | Schematic crystal structure of cubic perovskite ABO_3 (Left) and BO_6 octahedron (Right) in a perovskite structure. | 2 |
| Fig. 1.2 | Magnetic phase diagram for $RMnO_3$ as a function of the ionic radius of R (r_R). | 3 |
| Fig. 1.3 | Crystal structures of $LaMnO_3$ and $HoMnO_3$. Spin (arrows) and orbital (lobes) ordered features are also illustrated. The stack of spin and orbital order along the c axis is staggered and uniform order, respectively, for both the compounds. | 3 |
| Fig. 1.4 | (a) In-plane arrangement of Mn and O atoms. Arrows denote the direction of spins and AFM-coupled zigzag spin chains are highlighted by shaded areas. (b) Arrows show the directions of the ionic displacements for Mn (left) and O (right) in AFM- E . The thick arrows at the bottom show the direction of the resulting displacements of Mn and O sublattices and P. | 5 |
| Fig. 1.5 | Ordering of Mn-spins in multiferroic $TbMnO_3$ in (a) the high temperature SDW phase below $T_N = 41$ K and (b) in the ferroelectric cycloidal phase below $T_L = 28$ K. | 6 |
| Fig. 1.6 | (a) The bc -plane of the spin structure and positions occupied by the O ions (red circles). (b) The relations of the TM-O-TM cluster model (TM: transition-metal) with the rod-type $d_{3x^2-r^2}/d_{3y^2-r^2}$ staggered orbital order under a noncollinear spin configuration (m_y and m_z are the magnetic spins) with the associated electric polarization P_s . δy and δz denote the pd -hybridization. | 7 |
| Fig. 1.7 | (a) Magnetic unit cells of the E -phase domain in $HoMnO_3$. The arrows on the Mn atoms denote the directions of their spins. The FE displacements are not shown, but the direction of P is indicated [12]. (b) Atomic displacements in FE $HoMnO_3$, as obtained by the difference of atomic coordinates in optimized AFM- E spin configuration (length of arrows in arbitrary units). In the ab -plane, the AFM- E spin arrangement is also shown with black (right) and white (left) Mn atoms. (c) AFM-coupled zigzag spin chains are highlighted by shaded areas. The black-rimmed arrow at the right shows the direction of the resulting displacements of O sublattices [11]. (d) Thin blue vertical arrows denote the direction of Mn spins in the ‘straight’ Mn chains of the magnetic E -type ordering, cf. Fig. 1.7(b). Double exchange drives the Mn–O–Mn angle away from 180° when spins are antiparallel and towards it when spins are parallel. Orange vertical arrows indicate the resulting oxygen displacements; the direction of the ferroelectric polarization is indicated on the right of the chain by the red arrow. This picture applied to the E -type manganites gives a net electrical polarization indicated in the panel of Fig 1.7(b). | 10 |
| Fig. 1.8 | Orbital ordering temperatures of $RMnO_3$ as a Function of the in-plane Mn-O-Mn bond angle. | 11 |

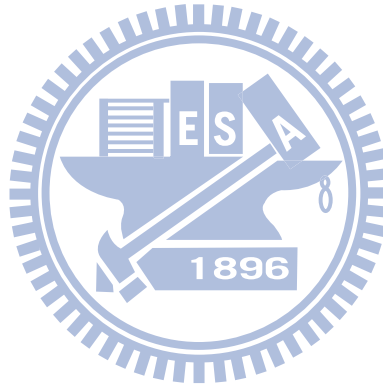
| | | |
|----------|--|----|
| Fig. 1.9 | Evolution of the lattice structure in $RMnO_3$ as a function of the size of the rare earth (RE). | 13 |
| Fig. 2.1 | (a) The overlap between the wave functions of $O^{2-} 2p$ and $Mn^{3+} 3d$ states for the superexchange interaction. (b) When two Mn^{3+} ions are being brought up to an O^{2-} ion from a large distance, the spin moments of two Mn^{3+} ions are random relation and of oxygen ion is zero for net moment, due to the filled shells. When a manganese ion with an up(\uparrow) spin is bound on the oxygen ion, the parallel spin of oxygen repels one another and forces another manganese to have a down(\downarrow) spin. | 19 |
| Fig. 2.2 | (a) and (b) The schemes of the double exchange mechanism which involves the conduction-electrons-hopping process. From [4, 8]. (c) The effective hopping (t_{eff}) of an e_g electron jumping between two nearest-neighbor Mn ions (reproduced from Ref. [8]). (d) Sketch of a spin-canted state, as discussed by de Gennes. | 21 |
| Fig. 2.3 | Illustration of how the crystal-field of the MnO_6 octahedron splits the five-fold degenerate $3d$ levels, and how the Jahn-Teller distortion of the MnO_6 octahedron further results in the non-degeneracy in the e_g and t_{2g} levels. | 23 |
| Fig. 2.4 | (a) The $Pbnm$ orthorhombic cell of $RMnO_3$. Black, white, and gray spheres represent O, Mn, and Ho atoms, respectively. From [12]. (b) ab in-plane view of MnO_2 planes, showing the large octahedral distortions and zigzag spin ordering. Solid lines mark the in-plane projected unit cell. (c) The simple sine-wave magnetic structure of $HoMnO_3$ for $T_L < T < T_N$ (d) The E -phase magnetic structure below T_L . | 25 |
| Fig. 3.1 | The x-ray diffraction patterns of hexagonal $HoMnO_3$ powder at room temperature. | 29 |
| Fig. 3.2 | (a) Temperature evolution of the zero-field-cooled susceptibility (ZFC- $\chi(T)$) with an applied magnetic field of 100 Oe. The inset shows the temperature-dependent inverse magnetic susceptibility. The lines indicate the Curie Weiss high-temperature extrapolation. (b) The ZFC and FC curves of $\chi(T)$ near the spin reorientation transition of Mn^{3+} . The inset shows the ZFC and FC curves of $\chi(T)$ around AF ordering of Ho^{3+} magnetic moments. | 31 |
| Fig. 3.3 | Schematics of a typical PLD process: a ceramic target is placed in a vacuum chamber and then a pulsed laser beam is focused onto the surface of the solid target. The strong absorption of the electromagnetic radiation by the solid surface leads to explosive evaporation of the target materials. The evaporated materials essentially form highly energetic and ionized plasma, often referred as "laser plume". | 33 |

| | | |
|----------|---|----|
| Fig. 3.4 | Illustration for describing the experimental processes carried out in this thesis. | 35 |
| Fig. 3.5 | The schematics of the in-plane arrangements between the <i>o</i> -HMO thin films and substrates. (a) <i>o</i> -HMO (0 <i>k</i> 0)/LAO(110): <i>c</i> -axis and <i>a</i> -axis of <i>o</i> -HMO are aligned with LAO[001] and LAO[1 $\bar{1}$ 0], respectively; (b) <i>o</i> -HMO (00 <i>l</i>)/STO(001): <i>a</i> - <i>b</i> diagonal of <i>o</i> -HMO is aligned randomly with STO [010] substrate direction, one expects that a twin-like structure might occur in these <i>o</i> -HMO (00 <i>l</i>) films; and (c) in-plane schemes of <i>o</i> -HMO thin films on STO(110) showing that the <i>c</i> -axis of <i>o</i> -HMO is aligned with STO[001], but <i>a</i> -axis or <i>b</i> -axis can be randomly aligned with STO[1 $\bar{1}$ 0]. | 37 |
| Fig. 4.1 | (a) The typical θ -2 θ diffraction pattern of <i>o</i> -HMO films grown on LAO(110) substrate. The inset in (a) shows the rocking curve of the <i>o</i> -HMO (020) peak. (b) The azimuthal ϕ -scans of the (110) peak of the <i>o</i> -HMO films, displaying the nearly ideal alignment of crystallographic orientations between film and substrate. | 42 |
| Fig. 4.2 | The AFM image of a 180 nm-thick <i>o</i> -HMO film deposited on LAO(110) substrate. The arrows indicate the growth direction of <i>o</i> -HMO grains. | 43 |
| Fig. 4.3 | (a) The zero-field-cooled temperature-dependent magnetizations (ZFC- <i>M</i> (<i>T</i>)) for <i>o</i> -HMO film probed along different crystal orientations with an applied magnetic field of 100 Oe. (b) The ZFC- <i>M</i> (<i>T</i>) along the <i>c</i> -axis measured at 100 Oe and 500 Oe. The inset in (b) shows full temperature range of the FC- and ZFC- <i>M</i> (<i>T</i>) measured at 500 Oe. Notice the 30 K anomalous ordering along the <i>c</i> -axis and the significant suppression of it by applying merely 500 Oe. | 45 |
| Fig. 4.4 | The XRD results of the <i>o</i> -HMO thin films grown on Nb:STO(001) substrates. (a) The θ -2 θ scans (intensity plotted in logarithmic scale) reveal that HMO films are indeed orthorhombic with nearly perfect <i>c</i> -axis oriented characteristic. The inset shows the rocking curve of the <i>o</i> -HMO (004) peak. (b) The ϕ -scan plot of the (202) peak of the <i>o</i> -HMO films indicates a clear fourfold symmetry, suggesting that the film is well-aligned along (001)-orientation, however, is of <i>ab</i> mixing character in film plane. | 49 |
| Fig. 4.5 | The temperature dependent magnetization (<i>M</i> (<i>T</i>)) of the <i>o</i> -HMO probed along the <i>c</i> -axis and the <i>ab</i> -plane. (a) The ZFC (solid symbols) and FC (open symbols) <i>M</i> (<i>T</i>)'s measured with a magnetic field of 100 Oe applying along the <i>c</i> -axis and in the <i>ab</i> -plane. Both reveal an AFM transition temperature of 43.2 K. (b) The enlarged version of the ZFC curves displayed in (a). A magnetic ordering near 34.6 K is evident in the <i>c</i> -axis. | 50 |
| Fig. 4.6 | The field-dependent magnetization (<i>M</i> - <i>H</i>) measured at four temperatures. The hysteretic behavior exhibited when $T < T_N$ | 52 |

- indicates the presence of weak ferromagnetism. The inset shows the results in larger scale.
- Fig. 4.7 The dielectric constant as a function of temperature measured along the c -axis of the o -HMO film. Significant suppression of the enhancement and peak temperature by the applied field are evident. The inset shows that the dielectric enhancement is non-hysteretic in temperature. 53
- Fig. 4.8 The XRD diffraction patterns of the o -HMO thin films grown on STO(001) substrates. (a) The typical θ - 2θ scans (intensity plotted in logarithmic scale) reveal that HMO films are indeed orthorhombic with nearly perfect c -axis oriented characteristic. The inset in (a) shows the rocking curve of the o -HMO (004) peak. (b) The azimuthal ϕ -scans (intensity plotted on a logarithmic scale) of the (202) peak of the o -HMO films, displaying the nearly ideal alignment of crystallographic orientations between film and substrate. The inset of (b) is a $2 \times 2 \mu\text{m}^2$ AFM topographic image of a 180 nm-thick o -HMO film deposited on STO(001) substrate. 58
- Fig. 4.9 (a) The zero-field-cooled temperature-dependent magnetizations (ZFC- $M(T)$) for o -HMO film probed along the c -axis and the ab -plane with an applied magnetic field of 100 Oe. Both reveal an AF transition temperature of 44.2 K. The inset in (a) shows the FC- and ZFC- $M(T)$ over the whole temperature range measured along the c -axis at 500 Oe. (b) The ZFC- $M(T)$ along the c -axis measured at 100 Oe and 500 Oe. (For the sake of clarity the 500 Oe curve is slightly shifted.) The 0.2 K difference seen in T_N for the 100 Oe and 500 Oe results is mainly due to different measuring temperature intervals used during measurements. As shown in the upper-right inset, when we change the temperature interval from 2 K to 1 K and re-measure part of the 100 Oe curve (indicated by the square frame), it evidently displays exactly the same T_N as seen on the 500 Oe curve measured with the same temperature interval. The lower-left inset shows that the similar feature also occurs for o -HMO/Nb-STO film with a magnetic field of 500 Oe. 60
- Fig. 4.10 P - E hysteresis loops of the o -HMO thin film grown on Nb-doped SrTiO₃(001) substrates measured at various temperatures. The inset shows the remnant polarization obtained by pulsed polarization measurement at various temperatures. 61
- Fig. 4.11 (a) The XRD θ - 2θ scan of the o -HMO thin film grown on Nb:STO(110) substrate, showing that the film is single-phase a -axis-oriented orthorhombic perovskite manganites (in $Pbnm$ space group settings). The inset in (a) shows a rocking curve measured around the o -HMO (200) peak. (b) The ϕ -scans of the same film displayed in (a), showing the nearly perfect in-plane alignments between film and substrate. 67
- Fig. 4.12 The zero-field-cooled (ZFC) $\chi(T)$ of the o -HMO films probed along the respective crystalline axis with an applied field of 100 68

Oe. The inset shows the temperature-dependence of first derivative of magnetization with respect to T measured with a 1000 Oe magnetic field along the c -axis.

- Fig. 4.13 An enlarged vision of magnetic-field dependent magnetization (M - H) curves measured at 60, 35, 27, and 23.5 K. The inset shows a clear hysteretic behaviour displayed at 10 K indicating the presence of weak ferromagnetism. 69
- Fig. 4.14 (a) The dielectric constant (ϵ_r) as a function of temperature for o -HMO film evaluated from our measurements when cooling (closed symbols) and warming (open symbols) the sample. The left inset shows the temperature-dependent inverse relative permittivity. The right inset shows the schematic cross-section view of the survey. 70
- Fig. 4.15 The electric-field dependent polarization (P - E) hysteresis loops for the o -HMO/Nb:STO(110) measured at 40, and 13 K. 71



Chapter 1

Introduction

1.1 The discovery of manganites with gigantic magnetoelectric effect

The mineral CaTiO_3 found in the Ural Mountains, gave its name perovskite to a large group of compounds which have been playing important roles in condensed matter physics and subjected to extensive investigations over the past several decades [1]. Among them, the perovskite manganites RMnO_3 (R =rare earth) are of particular interests because of the rich variety of intriguing emergent properties have been demonstrated to arising from the subtle interplays among the charge, spin, orbital, and lattice degree of freedoms. Colossal magnetoresistance (CMR) and charge ordering in hole-doped LaMnO_3 have been the subjects of great interest for the last decade, while recent discoveries of multiferroicity in TbMnO_3 [2] and DyMnO_3 [3] have created additional excitements in the studies of manganites. These electronic behaviors are all strongly dependent on the underlying lattices, and detailed knowledge on how the properties and structure evolve with the size of the rare-earth ions is expected to provide significant insights into the complex physics of manganites.

In the crystal structure of cubic perovskite (ABO_3), the A ion is residing at the eight corners of the cube, as depicted by the violet spheres shown in left panel of Fig. 1.1. On the other hand, the B ion (shown as the dark-blue sphere) is sitting at the body-center and forms an octahedron with the six nearest neighbored oxygen ions residing at the center of the six faces (red circles). The right panel of Fig. 1.1 shows the ideal cubic perovskite structure of LaMnO_3 , and one can envisage it as being consisted of a cubic array of the corner-shared BO_6 octahedrons. However, the assumption of rigidity of perovskite structure is no longer valid, if the central atom B is Jahn-Teller active, such as Cu^{2+} ($3d^9$), Mn^{3+} ($3d^4$), and Cr^{2+} ($3d^4$). For these ions, the Jahn-Teller effect is equivalent to the orbital ordering of e_g states. These states are doubly degenerated in a perfect octahedral coordination of the transition metal ions. Lifting this degeneracy by lowering the symmetry is the essence of the Jahn-Teller effect.

Perovskite $RMnO_3$ compounds are insulators with the orthorhombic structure (space group: $Pbnm$), where the distortion from the ideal cubic structure arises from two sources [5, 6]. One is the mismatch of R-O and Mn-O equilibrium bond lengths. In addition, the most significant effect on the crystal structure introduced by decreasing the ionic radius (r_R) is an enhancement of the cooperative rotation of the MnO_6 octahedra characterized by the decrease of Mn-O-Mn bond angle. By considering detailed structure of the most relevant ingredient, the MnO_6 octahedron, as a function of ionic size of the rare earth elements, Goto *et al.* [3] demonstrated that, with the decreasing r_R , the lattice constant is varied by Jahn-Teller distortion and Mn-O-Mn bond angle decrease from 155.1° ($LaMnO_3$) to 140.4° ($LuMnO_3$) [5]. This, in turn, gives rise to an evolutionary transition in the magnetic structure by changing the antiferromagnetic (AF) order from A -type (Mn moments ferromagnetically coupled within a - b plane and inter-planar coupling is AF) to E -type (Fig. 1.2 and 1.3).

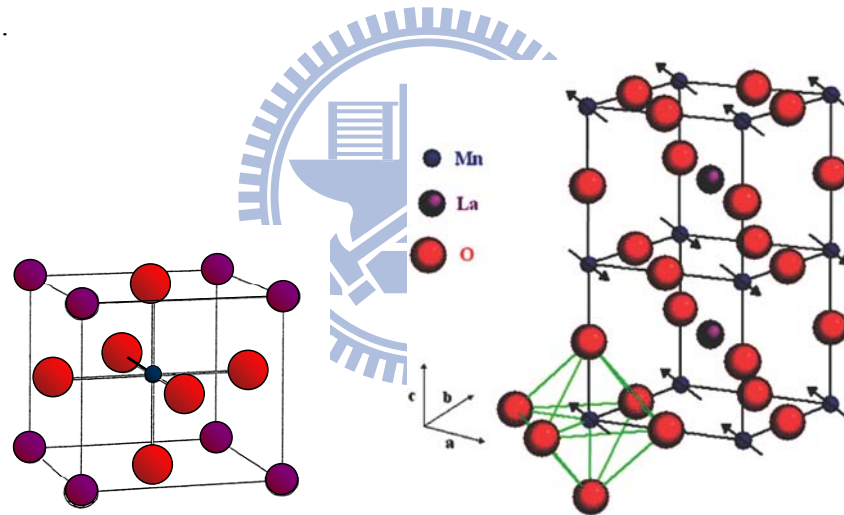


Figure 1.1 Schematic crystal structure of cubic perovskite ABO_3 (Left) and BO_6 octahedron (Right) in a perovskite structure. Adopted from [4].

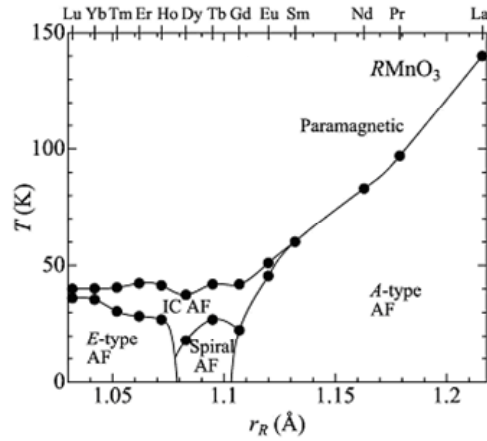


Figure 1.2 Magnetic phase diagram for $RMnO_3$ as a function of the ionic radius of R (r_R). Adopted from [5].

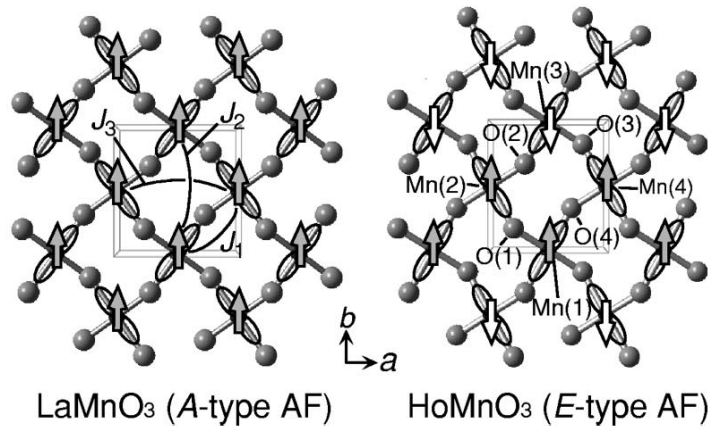


Figure 1.3 Crystal structures of $LaMnO_3$ and $HoMnO_3$. Spin (arrows) and orbital (lobes) ordered features are also illustrated. The stack of spin and orbital order along the c axis is staggered and uniform order, respectively, for both the compounds. Adopted from [6].

The path by which the magnetic structure varies with temperature turns out to play the key role of exhibiting the magnetism-induced “improper ferroelectricity”. In the A -type AF regime, it has been demonstrated that the paramagnetic Mn moments first convert into an incommensurate (IC) AF structure below the Néel temperature (T_N) and then enter a reordered commensurate helical spin structure below a lock-in transition temperature (T_L) for $R = \text{Eu, Gd, Tb, and Dy}$ [3]. The transition to the helical magnetic structure evidently breaks the spatial inversion symmetry thus allowing the ferroelectric polarization to

accompany. This microscopic understanding not only nicely explains the colossal magneto-capacitance concurring with the ICM to CM transition in DyMnO_3 [3] but also the intimate magneto-electric coupling in TbMn_2O_5 [7]. Subsequent theoretical studies by Katsura *et al.* [8, 9] pointed out that the electric polarization is primarily induced by the microscopic noncollinear magnetic structure via spin-orbital interaction. Mostovoy [10] reached the similar conclusions using the Ginzburg-Landau phenomenological approach. Noncollinear magnetic structures are stabilized due to either competing interactions (frustrations) or anisotropies generated by spin-orbit coupling, which leads to reduced transition temperatures and weaker order parameters. The magnitude of polarization P ($< 1000 \mu\text{C}/\text{m}^2$ in TbMnO_3 [2]) is also affected by its weak coupling to magnetism. In a quest for higher P , a recent model Hamiltonian study [11] concentrated on the collinear antiferromagnetic- E ($AFM-E$) spin configuration, where ferromagnetic zigzag spin chains in the ab -plane are antiferromagnetically coupled with respect to both adjacent zigzag chains in the b -direction (see left panel of Fig. 1.4) and out-of-plane stacked chains. Picozzi and Sergienko *et al.* [11] argued that the symmetry of the spin zigzag chain magnetic E -phase in orthorhombic perovskites with a net displacement allows the formation of a polar axis along the a -axis (right panel of Fig. 1.4). Moreover, they further predict that the polarization (\mathbf{P}) induced by the E -phase magnetic order can be up to 2 orders of magnitude higher than that obtained in the helical improper magnetic ferroelectrics (IMF's) [11-14]. In this regard, collinear IMF's may prove to be more promising for future applications as they are less prone to the obstacles mentioned above.

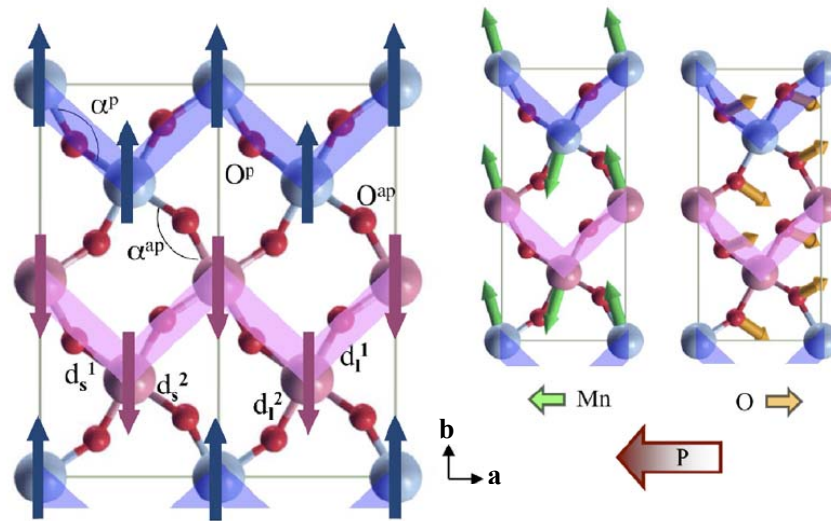
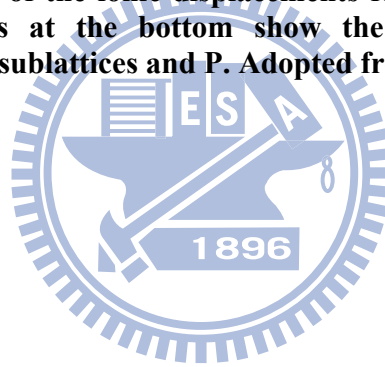


Figure 1.4 (a) In-plane arrangement of Mn and O atoms. Arrows denote the direction of spins and *AFM*-coupled zigzag spin chains are highlighted by shaded areas. (b) Arrows show the directions of the ionic displacements for Mn (left) and O (right) in *AFM-E*. The thick arrows at the bottom show the direction of the resulting displacements of Mn and O sublattices and P. Adopted from [11].



1.2 Origin of the magnetism-induced ferroelectricity in multiferroic orthorhombic $RMnO_3$

1.2.1 Spiral Magnetism

While in the $RMnO_3$ series the basic multiferroic properties appear to be governed by the Mn magnetism, several observations point to a complex role played by the rare earth in these materials. On the orthorhombic side of the perovskite manganites [5], $TbMnO_3$ was the first to bring about the unprecedented attention for its spontaneous electrical polarization reported by Kimura et al. [2]. The magnetic ordering in the $TbMnO_3$ perovskite exhibits three distinctive transitions. The first occurs at $T_N \sim 41$ K where Mn-spins order in a longitudinal spin-density-wave (SDW) propagating along the b -direction with a propagated wave vector $(0, q_{Mn}, 0)$ (see Fig. 1.5(a)). At lower temperatures, the second ordering occurs at $T_L = 28$ K (the value of q_{Mn} is locked into a constant of 0.28 [15]) and here Mn-spins develop a component along the c -axis that has a phase difference of $\pi/2$ compared to the b -axis component, thus resulting in a cycloidal Mn spin order as shown in Fig. 1.5(b). Indeed it is below T_L where a spontaneous polarization along the c -axis develops [2]. Such a close relationship between the lattice modulation and ferroelectricity is common to the so-called “improper magnetic ferroelectrics (IMF’s)”. On further cooling, the magnetic moments of Tb ions, show a quasi-long-range ordering below $T_N^{Tb} = 7$ K [15].

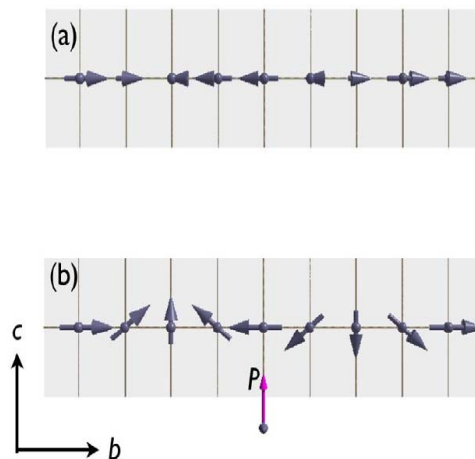


Figure 1.5 Ordering of Mn-spins in multiferroic $TbMnO_3$ in (a) the high temperature SDW phase below $T_N = 41$ K and (b) in the ferroelectric cycloidal phase below $T_L = 28$ K. Adopted from [16].

Ferroelectricity in these frustrated manganites results from the antisymmetric Dzyaloshinski–Moriya (DM) interaction which is a relativistic correction to the usual super-exchange and its strength is proportional to the spin–orbit coupling constant [17]. The DM interaction between two spins, S_i , S_j separated by r_{ij} is defined as $r_{ij} \times S_i \times S_j$ and favors non-collinear spin-ordering such as cycloids or helices. The spontaneous ferroelectric polarization, \mathbf{P}_s , can be expressed in terms of parameters that characterize the spin cycloid, namely, $\mathbf{P}_s \propto m_y m_z (\mathbf{e}_x \times \mathbf{Q})$ ((see Fig. 1.6(a) & (b)), where m_y and m_z are the amplitude of the spins along the b - and c -axis, respectively; \mathbf{e}_x is a unit vector along the axis of rotation of Mn-spins and \mathbf{Q} is the magnetic propagation vector [10, 17]. This phenomenological description as well as the theoretical framework based on the spin-current model has been very successful in predicting the size and direction of the polarization in the multiferroic manganites [8]. For example for $R = \text{Tb}$, the propagation vector is along the b -axis while Mn-spins rotate around the a -axis, predicting a spontaneous polarization parallel to the c -axis as indeed has been observed ($P \sim 800 \mu\text{C}/\text{m}^2$ [2]).

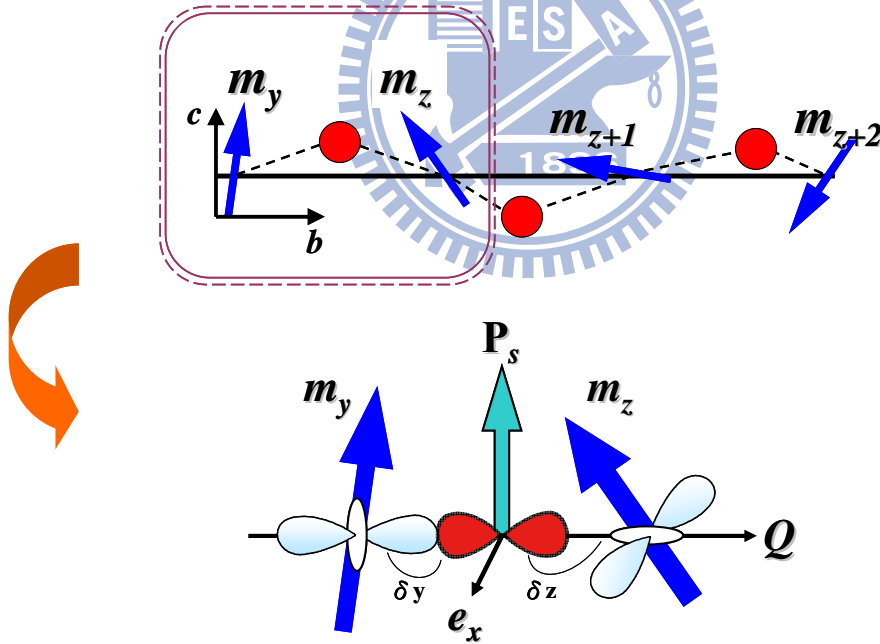


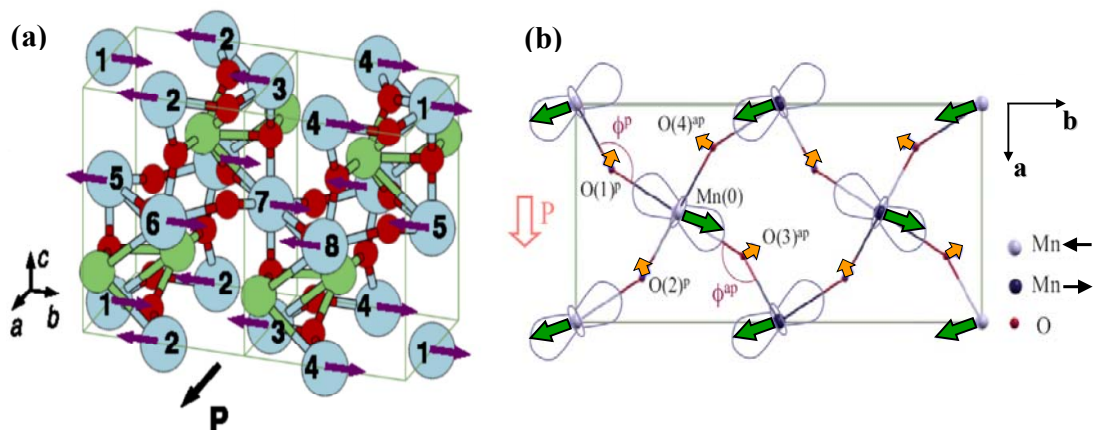
Figure 1.6 (a) The bc -plane of the spin structure and positions occupied by the O ions (red circles). (b) The relations of the TM-O-TM cluster model (TM: transition-metal) with the rod-type $d_{3x^2-r^2}/d_{3y^2-r^2}$ staggered orbital order under a noncollinear spin configuration (m_y and m_z are the magnetic spins) with the associated electric polarization \mathbf{P}_s . δ_y and δ_z denote the pd -hybridization.

Later, other equivalent model [18] based on spin-orbital interaction predicted an important mechanism of spin-polarization coupling and showed that spin spiral structure may induce the electric polarization. This could explain the origin of electric polarization in spiral magnets like TbMnO_3 with an estimated value of polarization which was very much consistent with the experimental observations. In all of these theoretical descriptions, the magnetoelectric effect is mainly originated from the symmetry-breaking magnetic transformation [19]. Thus, for spontaneous polarization to occur, these two magnetic-orders can only be non-collinear. Within the context of these scenarios, the polarization will not occur in the incommensurated phase because the collinear neighboring spins will result in zero cross product between \mathbf{S} and \mathbf{Q} . Nevertheless, in helical spin array non-zero polarization is expected. Supporting this view of TbMnO_3 is the novel phenomenon, which we call “magnetic-field-induced electric polarization flop,” where the direction of ferroelectric polarization can be switched from the c to the a -axis by the application of magnetic field [2, 20]. However, it is noted that usually a strong magnetic field is needed to change the spin symmetry of AFM state. Thus, the microscopic magnetoelectric behavior could be controlled only with relatively high fields. Similar feature was observed in other noncollinear multiferroics and some of them revealed reversible and memory effect [7].

1.2.2 Collinear Magnetism

In the perovskite manganite family $RMnO_3$ (space group $Pbnm$), the magnetic E -phase was first reported for $R=Ho$ as a result of magnetic structure refinement by neutron diffraction [21]. The E -type magnetic structure of this multiferroic, forming at temperatures below $T_L \sim 26-30$ K [21-23], is schematically shown in Fig. 1.7(a). As can be seen also in Fig. 1.7(b) & (c), the antiferromagnetic (AF) E -type phase of manganites is characterized by in-plane zigzag ferromagnetic (FM) chains antiferromagnetically coupled to neighboring chains; the out-of-plane coupling is AF as well.

Within the context of the non-collinear (spiral) magnetism-induced FE, the collinear AF shouldn't be able to result in the complex magnetoelectric polarization described above. In 2004, Lorenz et al. reported the anomaly dielectric behavior in orthorhombic $YMnO_3$ and $HoMnO_3$ materials prepared by high-temperature high-pressure synthesis [22]. The results have led to the scientists to reconsider the role of collinear AF in magnetoelectric effect. Sergienko et al. [12] by considering mechanisms other than spin-orbit interaction have estimated the polarization of the E -type $RMnO_3$ can have up to "2" orders of magnitude enhancement over that of the spiral phase $TbMnO_3$. The polarization in this case is induced along the a -axis in $Pbnm$ space group setting. In their calculation [12], the polarization was estimated about $5000-120000 \mu C/m^2$ which is compatible with the hexagonal $RMnO_3$.



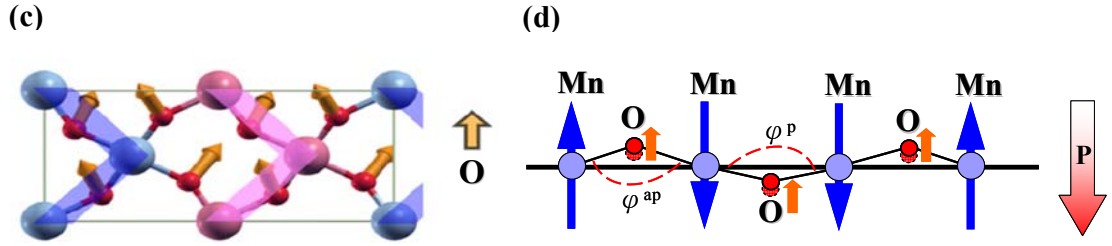


Figure 1.7 (a) Magnetic unit cells of the *E*-phase domain in HoMnO₃. The arrows on the Mn atoms denote the directions of their spins. The FE displacements are not shown, but the direction of P is indicated [12]. (b) Atomic displacements in FE HoMnO₃, as obtained by the difference of atomic coordinates in optimized *AFM-E* spin configuration (length of arrows in arbitrary units). In the *ab*-plane, the *AFM-E* spin arrangement is also shown with black (right) and white (left) Mn atoms. (c) *AFM*-coupled zigzag spin chains are highlighted by shaded areas. The black-rimmed arrow at the right shows the direction of the resulting displacements of O sublattices [11]. (d) Thin blue vertical arrows denote the direction of Mn spins in the ‘straight’ Mn chains of the magnetic *E*-type ordering, cf. Fig. 1.7(b). Double exchange drives the Mn–O–Mn angle away from 180° when spins are antiparallel and towards it when spins are parallel. Orange vertical arrows indicate the resulting oxygen displacements; the direction of the ferroelectric polarization is indicated on the right of the chain by the red arrow. This picture applied to the *E*-type manganites gives a net electrical polarization indicated in the panel of Fig 1.7(b).

As shown in Fig. 1.7(b) & (c), the oxygens are shifted away from their original position at the center of Mn–Mn bonds, due to the strong tilting of MnO₆ octahedra. Furthermore, it is noteworthy that in the case of double exchange between Mn ions the oxygen would move toward the same direction: in this situation the ferromagnetic exchange increases with the Mn–O–Mn angle stretching towards 180°, see Fig. 1.7(d). This mechanism is based on the interplay between electron hopping and elastic energy in distorted perovskites, and it can lead to ferroelectricity with a sizable polarization. Indeed, the latter was confirmed by means of first-principles calculations performed on orthorhombic-HoMnO₃ (*o*-HMO), which gave an estimated polarization of 60000 $\mu\text{C}/\text{m}^2$. The largest value reported so far for magnetism-induced ferroelectricity. Although *o*-HMO was considered here as a test case, we believe that their findings on the dual nature of ferroelectricity- as arising from a symmetry breaking induced by magnetic order- have a wider range of validity for the family of IMF’s [13], where both the lattice and electronic degrees of freedom should be taken into account accurately since they are simultaneously relevant.

1.3 Survey of the magnetic phase diagram versus R^{3+} -ion radius in the perovskites $RMnO_3$ family

As depicted in Fig. 1.3, magnetic frustration in $RMnO_3$ perovskite manganites can be induced by structural tuning of the nearest neighbor (NN) (J_1) and next-nearest-neighbor (NNN) (J_2) Mn magnetic interactions [6]. The variation of the size of the R -ion directly modifies the Mn–O–Mn bond angles (shown in Fig. 1.8) and modulates the strength of the super-exchange interaction between Mn-ions. In $LaMnO_3$ the antiferro-type ordering of singly occupied $Mn^{3+} 3d_{3x^2-r^2}$ and $3d_{3y^2-r^2}$ orbitals produces ferromagnetic (FM) interactions within the ab -plane of the perovskite lattice (A-type magnetic structure) while the coupling between planes is antiferromagnetic (AF). As the size of the trivalent R cation decreases, the A-type phase becomes frustrated. As can be seen also in Fig. 1.8, this is highlighted by the steady decrease of T_N from 140 K for $R = La$ to ~ 40 K for $R = Eu$. This behavior, which is ascribed to progressive weakening of J_2 with respect to J_1 [6], leads to a commensurate AF ordering within the ab -plane of the perovskite lattice for $R = Ho$ (E-type magnetic structure) [21].

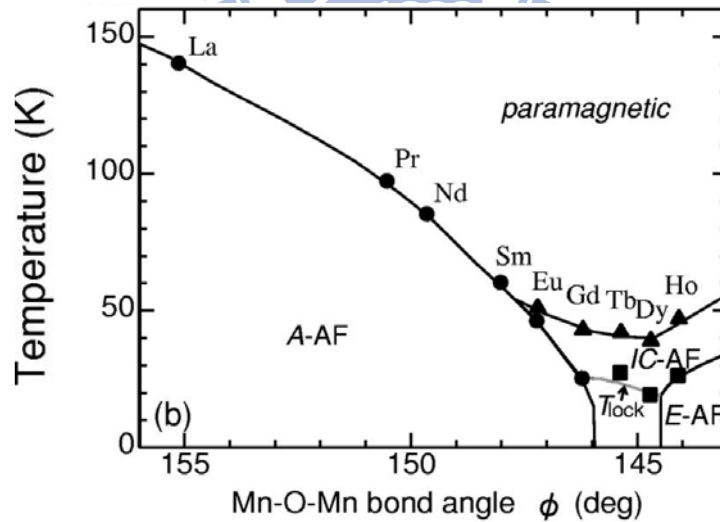
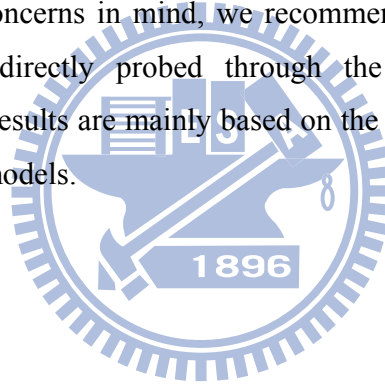


Figure 1.8 Orbital ordering temperatures of $RMnO_3$ as a Function of the in-plane Mn-O-Mn bond angle. Adopted from [6].

On the other hand, Zhou and Goodenough [24] have recently reported the evolution of Néel temperature (T_N) and crystal structure for the entire family of $RMnO_3$ perovskites ($R=La-Lu$), and concluded that the relevant competition is between the t -orbital and e -orbital spin-spin interactions within each Mn-O-Mn bond in the ab plane, rather than the antiferromagnetic (AF) NNN interaction as proposed by Kimura *et al.* [6]. Furthermore, they argued [24] that the Jahn-Teller (JT) distortion plays the dominant role in determining T_N in the A -type phase, and both the JT distortion and T_N become insensitive to a change in r_R for $R=Ho-Lu$ with the E -type structure. While further studies are clearly needed to clarify the controversial arguments, we suggest that more detailed experiments for E -type of orthorhombic perovskites are required before additional theories are put forth: The expected temperature profiles of magnetization for E -type do not appear in Ref. 6 and 26, and the large scatter in the reported structural parameters [24, 25] can lead to misleading interpretations. With these concerns in mind, we recommend that the complete magnetic phase diagram should be directly probed through the magnetic measurements on high-quality samples. These results are mainly based on the data themselves rather than on the details of the theoretical models.



1.4 Motivation

The crucial and yet controversial issues involved in the improper ferroelectricity of the collinear E -type magnetic structure remain unsettled. The magnetic structures derived from two previous neutron diffraction investigations [21, 26] seemed to support the prevailing of an ICM-to-CM AFM transition necessitated for a macroscopic polarization based on the mechanisms proposed by Sergienko [11] and Picozzi *et al.* [12-13]. However, the expectation of two orders of magnitude higher polarization in the E -type structure can not be verified in the case of o -HMO [23]. It is likely that the polycrystalline nature of these samples is the primary reason [22, 23]. Therefore, high quality single crystals of the E -type manganites are needed to resolve the improper ferroelectricity in more details. Unfortunately, under ambient conditions, rare earth perovskite manganites compounds with $R=Y, Ho, Er, Tm, Yb, Lu, Sc$ exhibit hexagonal crystallographic structures, in contrast to those REs with larger ionic radius which display orthorhombic perovskite structure (Fig. 1.9). Consequently, the few available reported results on polycrystalline or powder samples [5] may not be adequate to reveal the exact orientation correlations between the obtained polarization and the ordering spins. Lorenz *et al.* [23] further suggested that investigations on the FE properties of the E -phase multiferroic manganites might have to be realized by using thin films grown on appropriate substrates, while large single crystals of the compounds are not available.

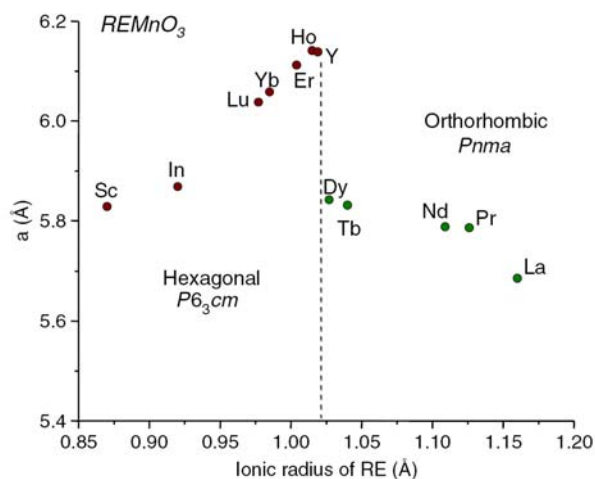


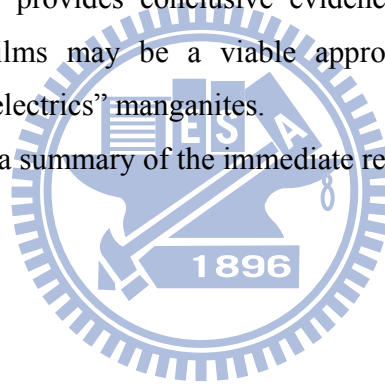
Figure 1.9 Evolution of the lattice structure in $RMnO_3$ as a function of the size of the rare earth (RE). From [27].

In recent years, the magnetoelectric (ME) coupling has been considered as the key to the promising multifunctional applications that could lead to the development of novel electronic devices [28-30]. In view of the practical applications, it is necessary to obtain these multiferroics in the form of thin films, as well. However, up to now, there have been only few studies on multiferroic thin films [31]. Quite recently, the orthorhombic $RMnO_3$ (R=Dy, Tb, Gd) phases were reported to be fabricated in metastable hexagonal thin film forms artificially grown on Pt(111)/Al₂O₃(0001) and YSZ(111) substrates [32-35]. In that event, it could be possible to stabilize hexagonal $RMnO_3$ into a metastable orthorhombic phase by using a suitable substrate. As shown in Fig. 1.9, HoMnO₃ is an end member of the hexagonal manganites, it would be an ideal candidate to engineer into orthorhombic thin films and to search for emerging physical properties.

Since within the frameworks of various microscopic mechanisms the magnetic ordering and associated ferroelectricity are intimately related to specific crystallographic orientations, consequently in order to gain more insight toward understanding these intriguing physical properties, it is essential to obtain samples capable of revealing the relevant properties along the respective crystallographic orientations. Therefore, in this study, we will concentrate primarily on manufacturing suitable thin film samples of the *E*-type magnetic structure of orthorhombic HoMnO₃ (*o*-HMO). In this scenario, more detailed information about the magnetoelectric behaviors of *o*-HMO would definitely help us to disclose conundrum expected for the collinear *E*-type antiferromagnetic manganites, which are unprecedented in the literature.

1.5 Organization of this dissertation

- (a) In chapter 2, we will describe the basic concepts and origin of magnetism for the perovskite-structured manganites $RMnO_3$. The related magnetic and lattice modulations in the perovskite-structured $RMnO_3$ will be also discussed here.
- (b) In chapter 3, the structural, magnetic properties, and microstructure of polycrystalline samples of the hexagonal $HoMnO_3$ (h -HMO) are presented. On the other hand, we will discuss the feasible routes in obtaining the orthorhombic $HoMnO_3$ from the thermodynamically stable h -HMO phases by epitaxial stabilization.
- (c) In chapter 4, we verify the role of substrate in stabilizing orthorhombic HMO (o -HMO) thin films. Furthermore, various substrates for the preparation of o -HMO specimens will be systematically studied and some outstanding issues will be clarified. The work presented in this chapter provides conclusive evidences about that the o -HMO of E -phase epitaxial thin films may be a viable approach to observing the so-called “improper magnetic ferroelectrics” manganites.
- (d) In chapter 5, we will give a summary of the immediate results in this dissertation.



References

- [1] J. B. Goodenough & J. M. Longo, *Crystallographic and Magnetic Properties of Perovskites and Perovskite-Related Compounds*, Springer Verlag, 1970.
- [2] T. Kimura, T. Goto, H. Shintani, K. Ishizaka, T. Arima, and Y. Tokura, *Nature (London)* **426**, 55 (2003).
- [3] T. Goto, T. Kimura, G. Lawes, A. P. Ramirez, and Y. Tokura, *Phys. Rev. Lett.* **92**, 257201 (2004).
- [4] 張維仁，國立交通大學博士論文 (2006).
- [5] M. Tachibana, T. Shimoyama, H. Kawaji, T. Atake, and E. Takayama-Muromachi, *Phys. Rev. B* **75**, 144425 (2007).
- [6] T. Kimura, S. Ishihara, H. Shintani, T. Arima, K. T. Takahashi, K. Ishizaka, and Y. Tokura, *Phys. Rev. B* **68**, 060403(R) (2003).
- [7] N. Hur, S. Park, P. A. Sharma, J. S. Ahn, S. Guha, and S. -W. Cheong, *Nature (London)* **429**, 392 (2004).
- [8] H. Katsura, N. Nagaosa, and Alexander V. Balatsky, *Phys. Rev. Lett.* **95**, 057205 (2005).
- [9] H. Katsura, Alexander V. Balatsky, and N. Nagaosa, *Phys. Rev. Lett.* **98**, 027203 (2007).
- [10] M. Mostovoy, *Phys. Rev. Lett.* **96**, 067601 (2006).
- [11] S. Picozzi, K. Yamauchi, B. Sanyal, I. A. Sergienko, and E. Dagotto, *Phys. Rev. Lett.* **99**, 227201 (2007).
- [12] I. A. Sergienko, C. Sen, and E. Dagotto, *Phys. Rev. Lett.* **97**, 227204 (2006).
- [13] K. Yamauchi, F. Freimuth, S. Blügel, and S. Picozzi, *Phys. Rev. B* **78**, 014403 (2008).
- [14] C.-Y. Ren, *Phys. Rev. B* **79**, 125113 (2009).
- [15] R. Kajimoto, H. Yoshizawa, H. Shintani, T. Kimura, and Y. Tokura, *Phys. Rev. B* **70**, 012401 (2004).
- [16] N. Aliouane, O. Prokhnenko, R. Feyerherm, M. Mostovoy, J. Stremper, K. Habicht, K. C. Rule, E. Dudzik, A. U. B. Wolter, A. Maljuk and D. N. Argyriou, *J. Phys.: Condens. Matter.* **20** 434215 (2008).
- [17] S.-W. Cheong and M. Mostovoy, *Nat. Mater.* **6**, 13 (2007).
- [18] C. Jia, S. Onoda, N. Nagaosa, and J. H. Han, *Phys. Rev. B* **76**, 144424 (2007).

- [19] M. Kenzelmann, A. B. Harris, S. Jonas, C. Broholm, J. Schefer, S. B. Kim, C. L. Zhang, S.-W. Cheong, O. P. Vajk, and J. W. Lynn, *Phys. Rev. Lett.* **95**, 087206 (2005).
- [20] T. Kimura, G. Lawes, T. Goto, Y. Tokura, and A. P. Ramirez, *Phys. Rev. B* **71**, 224425 (2005).
- [21] A. Muñoz, M. T. Casáis, J. A. Alonso, M. J. Martínez-Lope, J. L. Martínez, and M. T. Fernández-Díaz, *Inorg. Chem.* **40**, 1020 (2001).
- [22] B. Lorenz, Y. Q. Wang, Y. Y. Sun, and C. W. Chu, *Phys. Rev. B* **70**, 212412 (2004).
- [23] B. Lorenz, Y. -Q. Wang, and C. W. Chu, *Phys. Rev. B* **76**, 104405 (2007).
- [24] J.-S. Zhou and J. B. Goodenough, *Phys. Rev. Lett.* **96**, 247202 (2006).
- [25] J. B. Goodenough, *Phys. Rev. B* **74**, 014422 (2006).
- [26] H. W. Brinks, J. Rodríguez-Carvajal, H. Fjellvåg, A. Kjekshus, and B. C. Hauback, *Phys. Rev. B* **63**, 094411 (2001).
- [27] W. Prellier, M. P. Singh, and P. Murugavel, *J. Phys.: Condens. Matter* **17**, R803 (2005).
- [28] M. I. Bichurin, D. Viehland, and G. Srinivasan, *Journal of Electroceramics* **19**, 243 (2007).
- [29] C.-W. Nan, M. I. Bichurin, S. Dong, D. Viehland, and G. Srinivasan, *J. Appl. Phys.* **103**, 031101 (2008).
- [30] Y. Zhang, Z. Li, C. Deng, J. Ma, Y. Lin, and C.-W. Nan, *Appl. Phys. Lett.* **92**, 152510 (2008).
- [31] R. Ramesh, and Nicola A. Spaldin, *Nat. Mater.* **6**, 21 (2007).
- [32] J.-H. Lee, P. Murugavel, D. Lee, T. W. Noh, Y. Jo, M.-H. Jung, K. H. Jang, and J.-G. Park, *Appl. Phys. Lett.* **90**, 012903 (2007).
- [33] J.-H. Lee, P. Murugavel, H. Ryu, D. Lee, J. Y. Jo, J. W. Kim, H. J. Kim, K. H. Kim, Y. Jo, M.-H. Jung, Y. W. Oh, Y.-W. Kim, J. G. Yoon, J.-S. Chung, and T. W. Noh, *Adv. Mater.* **18**, 3125 (2006).
- [34] D. Lee, J.-H. Lee, P. Murugavel, S. Y. Jang, T. W. Noh, Y. Jo, M.-H. Jung, Y. D. Ko, and J.-S. Chung, *Appl. Phys. Lett.* **90**, 182504 (2007).
- [35] D. Lee, J.-H. Lee, S. Y. Jang, P. Murugavel, Y. D. Ko, and J.-S. Chung, *Journal of Crystal Growth* **310**, 829 (2008).

Chapter 2

Exchange interactions and environmental effects in perovskite manganites

2.1 Introduction

From the hydrogen atom with one electron to heavier atoms with multiple-electrons, the electron-electron interaction is playing the essential role in giving rise to a wide variety of physical properties. However, it might also be the most difficult one to understand due to the many possible acting ways of the Coulomb force between electrons. One of the important effects, which can lift the degeneracy of states with different total spins is called the "*exchange interaction*". In many-electron systems, the exchange Hamiltonians are difficult to derive from the first principle so one often takes a pragmatic approach in solid state physics to keep the Hamiltonian in simple form and to fit experiments. The exchange energy forms an important part of the total energy of many molecules and of covalent bond in many solids. Heisenberg showed that the exchange energy between atom i and j , with spin angular momentum $\mathbf{S}_i\hbar/2\pi$ and $\mathbf{S}_j\hbar/2\pi$ respectively, is given by $E_{\text{ex}} = -2J_{ij}\mathbf{S}_i\cdot\mathbf{S}_j$ (J is the exchange integral and \mathbf{S} is for electron spin). If J_{ij} is positive, E_{ex} is the minimum when the spins are parallel and the maximum when they are anti-parallel. If J_{ij} is negative, the lowest energy state results from anti-parallel spins.

2.2 Superexchange

The kinetic exchange mechanism of antiferromagnetism is sufficient for the qualitative understanding of most insulating antiferromagnets. The source of kinetic exchange is the hopping of electrons from site to site, restrained only by Coulomb repulsion. Furthermore, the hopping between two states with parallel spins is prohibited by the Pauli exclusion principle. However, most antiferromagnetic insulators are transition metal compounds, in which the d -electrons of the cations are separated by large anion (i.e. O^{2-} ion), and the hopping between the orbitals of the cation d -electrons seems rather indirect and unlikely to take place. The effect of kinetic exchange can be enhanced via the covalent

mixing between the cation and the anion orbitals. This mechanism of indirect exchange is called *superexchange*. An idealized situation is shown in the Fig 2.1(a). The overlap between d and p orbitals gives rise to a covalent mixing which allows the nominally p electrons to partially reoccupy the cations. As displayed in the Fig 2.1(b), the \downarrow spin p -electron can hop to the left, cation A , and thus d -spins are either in the parallel $\downarrow\downarrow$ or anti-parallel $\uparrow\downarrow$ configuration. According to the Pauli exclusion principle, the spin in manganese must be anti-parallel to the mediating one. The oxygen ion becomes the excited state with an unpaired spin, which can be, in turn, paired with the other neighboring manganese. As a whole, these two neighboring manganese ions are thus effectively coupled by the oxygen ions and result in an antiferromagnetic interaction.

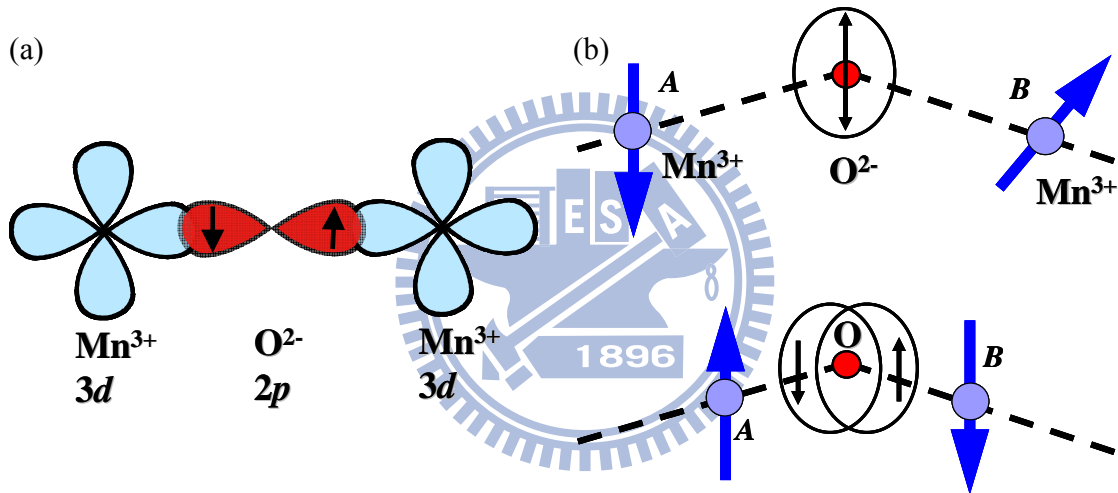


Figure 2.1 (a) The overlap between the wave functions of $O^{2-} 2p$ and $Mn^{3+} 3d$ states for the superexchange interaction. (b) When two Mn^{3+} ions are being brought up to an O^{2-} ion from a large distance, the spin moments of two Mn^{3+} ions are random relation and of oxygen ion is zero for net moment, due to the filled shells. When a manganese ion with an up(\uparrow) spin is bound on the oxygen ion, the parallel spin of oxygen repels one another and forces another manganese to have a down(\downarrow) spin.

2.3 Double exchange

The concept of the double-exchange (DE) interaction was introduced by Zener [1-3] in order to explain the ferromagnetism exhibited in some perovskite manganites. Zener interpreted the ferromagnetism as arising from an indirect coupling between the t_{2g} localized spins of manganites via “conducting electrons”. The manganites were addressed

explicitly that the conduction electrons are the e_g electrons [1]. Moreover, Zener further reasoned that the transfer must be through the oxygen ion between the manganese ions, and argued that the true transfer occurs through an actual “double-exchange” of electrons. This mechanism is schematically depicted in Fig. 2.2(a) & (b). It simply amounts to a simultaneous transfer of an electron from the Mn^{3+} site to the central oxide ion and an electron from the oxide ion to the Mn^{4+} site [4], such that the net transfer is of an electron from left Mn to right Mn. It is also interesting to remark, as Zener did, that the mechanism leading to ferromagnetism that he found should not be confused with the “superexchange” idea, which also uses oxygen as a bridge between manganese ions. Zener indicated correctly that the superexchange interaction leads to an antiferromagnetic alignment of spins, as the above-mentioned paragraph. The seminal work of Zener was extended by Anderson and Hasegawa [5], who studied the proposed mechanism in greater detail. Perhaps the most often-quoted portion of the work constructed by Anderson and Hasegawa is that the effective hopping t_{eff} of an e_g electron jumping between two nearest-neighbor Mn ions can be sketched as $t_{\text{eff}} = t \cos(\theta_{ij}/2)$, where θ_{ij} is the relative angle between the site i and j spins, as shown in Fig. 2.2(c). These simple effective hopping ideas provided plausible interpretations for the obtained research results on manganites in the early days. However, currently it is well known that more elaborate theories are needed to explain the complexity of the phase diagrams of these compounds, as well as the CMR effect.

Continuing this introduction to theoretical ideas proposed in the early days for manganites, it is also interesting to address the spin-canted state constructed by de Gennes [6], as the possible stable-state obtained by doping an antiferromagnetic state with holes and electrons (see Fig. 2.2(d)). This spin-canted idea has been extensively used by experimentalists until very recently, every time they observed some coexistence of ferromagnetic and antiferromagnetic features (the spin-canted state has a net moment, coexisting with a staggered distribution of spins perpendicular to that net moment). On the other hand, it has been proposed [7] that, in the hexagonal phase of HoMnO_3 , canting of the Mn^{3+} spins out of the basal xy plane can drastically reduce the magnetic symmetry and hence induce magnetoelectric effect. Thus, in order to check whether truly canted states can be stabilized in manganites at zero magnetic fields, this issue will be discussed in the context of the orthorhombic HoMnO_3 thin films.

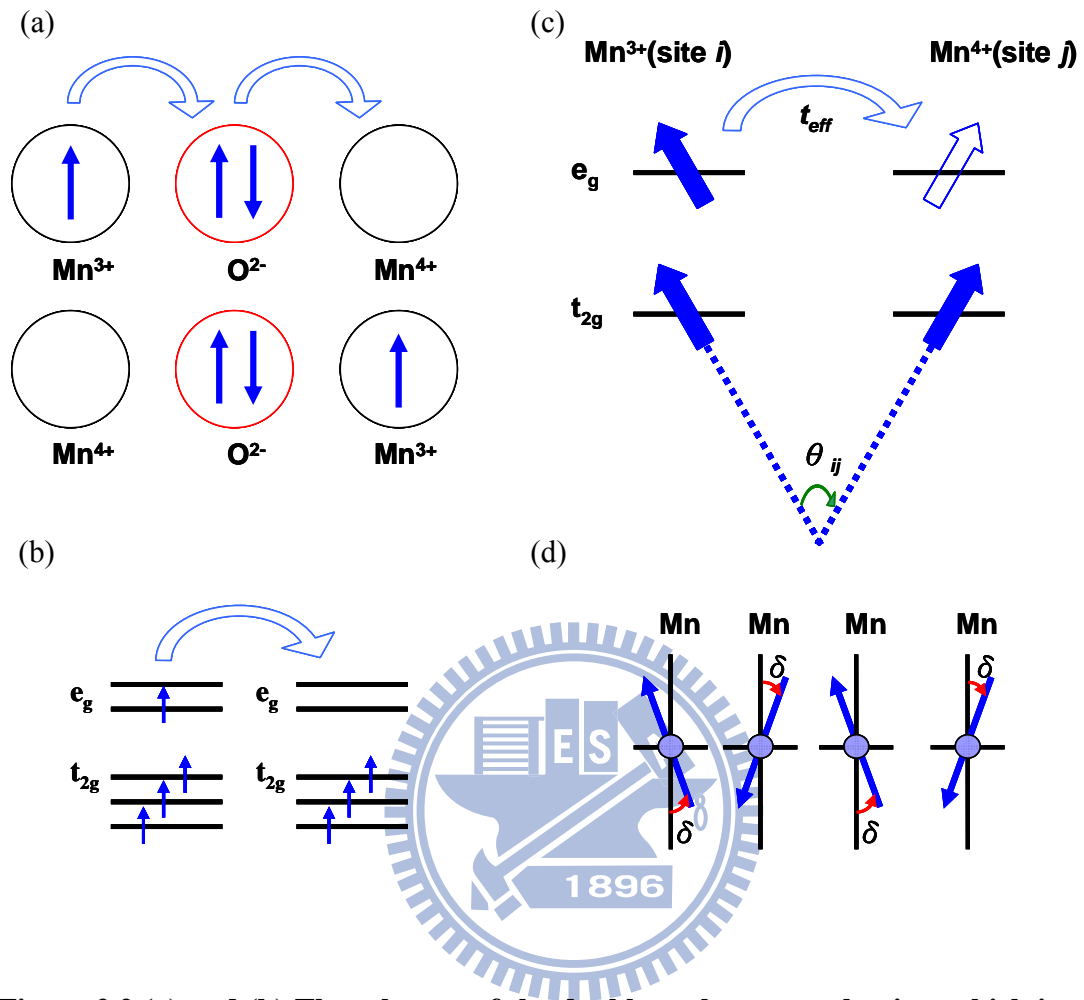


Figure 2.2 (a) and (b) The schemes of the double exchange mechanism which involves the conduction-electrons-hopping process. From [4, 8]. (c) The effective hopping (t_{eff}) of an e_g electron jumping between two nearest-neighbor Mn ions (reproduced from Ref. [8]). (d) Sketch of a spin-canted state, as discussed by de Gennes (reproduced from Ref. [4]).

2.4 Crystal field and Jahn-Teller effect

In most perovskite structured transition metal oxides, the ions of Mn, Cu, or other elements in the transition-metal row of the Periodic Table have an active d -shell with five degenerate levels. The degeneracy is present due to rotational invariance within the angular momentum $l=2$ subspace, as we learned from the elementary quantum mechanics. In vacuum, any direction or axis is the same as any other. The situation drastically changes once the ions are part of a crystal structure, since now the directions of the crystal axes are

certainly special compared with other directions. Fully rotational invariance is lost, but a subgroup remains. This effect results in a particular splitting of the five $l=2$ levels (*called the crystal-field splitting*), which is very important for the physics of transition-metal oxides. Fig. 2.3 schematically illustrates how the crystal field splits the $3d$ orbitals into the t_{2g} (the threefold degenerate orbitals d_{xy} , d_{yz} , and d_{zx}) and e_g (the twofold degenerate orbitals

$$d_{x^2-y^2} \text{ and } d_{3z^2-r^2}) \text{ levels with an energy separation usually expressed as } 10Dq = \frac{5}{3} \frac{Ze \langle r^4 \rangle}{a^5},$$

where Z is the atomic number of the ligand ion, e is the electron charge, a is the distance between manganese and oxygen ions, r is the coordinate of the $3d$ orbital, and $\langle \rangle$ denotes the average value by the radial wave function of the $3d$ orbital, respectively [9]. In a crystal field resulted from an octahedral structure, the main differences between e_g set and t_{2g} set are the directions that the orbitals are pointing, with the former directing straight at the ligands and the latter directing between the ligands. Hence, as an obvious consequence of charge repulsion in the electrostatic crystal field model, the e_g electrons are having a higher energy level and stronger hybridization with the O $2p$ orbitals than the t_{2g} electrons.

In the cubic symmetry considered in the previous paragraph, the splitting due to the crystal-field effect leads to an e_g doublet and a t_{2g} triplet. The remaining degeneracy is usually broken by the lattice motion. The ligand ions surrounding the transition-metal ion under consideration (i.e. the oxygen ions around manganese) can slightly readjust their locations, creating an asymmetry between the different directions that effectively removes the degeneracy. The lifting of degeneracy owing to the orbital-lattice interaction is called the Jahn-Teller co-operative effect. Assuming that the octahedron is elongated along the z -direction, as illustrated in the lower-middle panel of Fig. 2.3, the two oxygen ions in the z -axis are shifted away from the central ion, comparing with the oxygen ions in the x - y plane. An electron in the $3z^2-r^2$ orbital is less repelled by other charges so lying at lower energy level than one in the x^2-y^2 orbital. Vice versa, the compression along the z -axis will lower the energy level of the x^2-y^2 orbital and raise the energy of the $3z^2-r^2$ level. As is evident in the Fig. 2.3, the twofold degenerate e_g level, with x^2-y^2 and $3z^2-r^2$ orbital, is split into non-degenerate levels by the tetragonal distortion. The distributions of the five d -orbital electron clouds are also schematically displayed in the right most panel of Fig. 2.3.

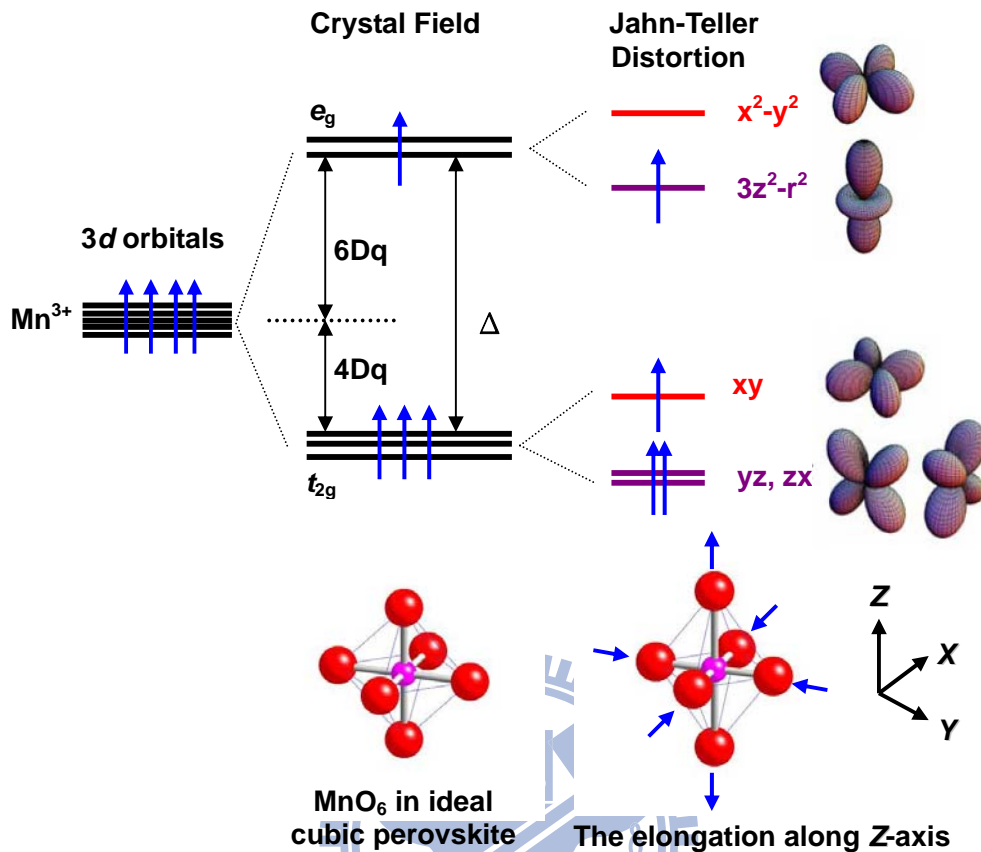


Figure 2.3 Illustration of how the crystal-field of the MnO_6 octahedron splits the five-fold degenerate 3d levels, and how the Jahn-Teller distortion of the MnO_6 octahedron further results in the non-degeneracy in the e_g and t_{2g} levels (reproduced from Ref. [4, 8]).

2.5 Tolerance Factor and E -phase magnetic structure

The “tolerance factor” plays an important role in perovskite manganites and related materials. It is a geometrical factor defined as $\Gamma = d_{R-O} / (\sqrt{2}d_{Mn-O})$. Here, d_{R-O} is the distance between the rare-earth-site and the nearest oxygen and d_{Mn-O} is the shortest distance between Mn and oxygen (remember that the La ion is at the center of a cube with Mn in the vertices and O in between the Mn ions). Since for an undistorted cube with a straight Mn-O-Mn link, $d_{R-O} = \sqrt{2}$ and $d_{Mn-O} = 1$, in units of the Mn-O distance, thus one will have $\Gamma = 1$ in this perfect system. However, sometimes the rare-earth ions are too small to fill the space in the cube centers and for this reason the oxygens tend to move

toward the center, reducing d_{R-O} (in general, d_{Mn-O} also changes at the same time) and leading to a smaller tolerance factor ($\Gamma < 1$) with the angle of the Mn-O-Mn bonding θ smaller than 180° [9]. The hopping amplitude for carriers to move from Mn to Mn naturally decreases as θ is reduced from 180° . As a consequence, as the tolerance factor decreases, the tendency of charge localization increases due to the reduction in the carrier mobility. This has been ubiquitously observed experimentally in many Mn oxides.

The unit cell in the E -type orthorhombic phase shows the $Pbnm$ symmetry (with 20 atoms/unit cell and choosing c -direction as the longest axis), with enormous distortion with respect to the ideal cubic perovskite (see Fig. 2.4 (a)): due to the Jahn-Teller instability shown by the Mn^{3+} ion, with electronic configuration $d^4 (t_{2g}^3 e_g^1)$, oxygen octahedrons are highly distorted and tilted (the average Mn-O-Mn angle is close to 144° for $HoMnO_3$, to be compared with the much larger value of $\sim 155^\circ$ in $LaMnO_3$). We recall that for the magnetic structure of orthorhombic $HoMnO_3$ (o -HMO), the Mn atoms with parallel spins form zigzag chains in the ab -plane, with the chain links equal to the nearest-neighbor Mn-Mn distance (see Fig. 2.4 (b)). The neighboring zigzag chains in the b -direction have anti-parallel spins. Therefore, the important issue, related to the origin of the incommensurate [10] ordering at $T_N=40-47.5$ K [11] (as sketched schematically in Fig. 2.4(c)), is also probably in connection with the weakening of the direct superexchange interactions due to the distortion of the perovskite structure. Furthermore, the periodic relation between the magnetic and crystal structure is described by the propagation vector $\mathbf{k} = (0, k_b, 0)$, which indicates the transition to an incommensurate magnetic structure ($k_b=0.4$ at 40 K) [11]. As temperature diminishes, its value progressively increases and reaches $k_b=0.5$ around $T\sim 30$ K. This implies the transition to a commensurate magnetic structure defined by $\mathbf{k} = (0, 1/2, 0)$. The commensurate propagation parameter ($k_b=0.5$) remains stable down to $T\sim 1.8$ K. Fig 2.4(c) and (d) show that the equal-spin E -phase structure can be obtained from the simple sine-wave structure by locking-in its modulation vector $k_b=0.5$ about $T\sim 30$ K (*called the lock-in temperature (T_L)*) and fine-tuning its phase.

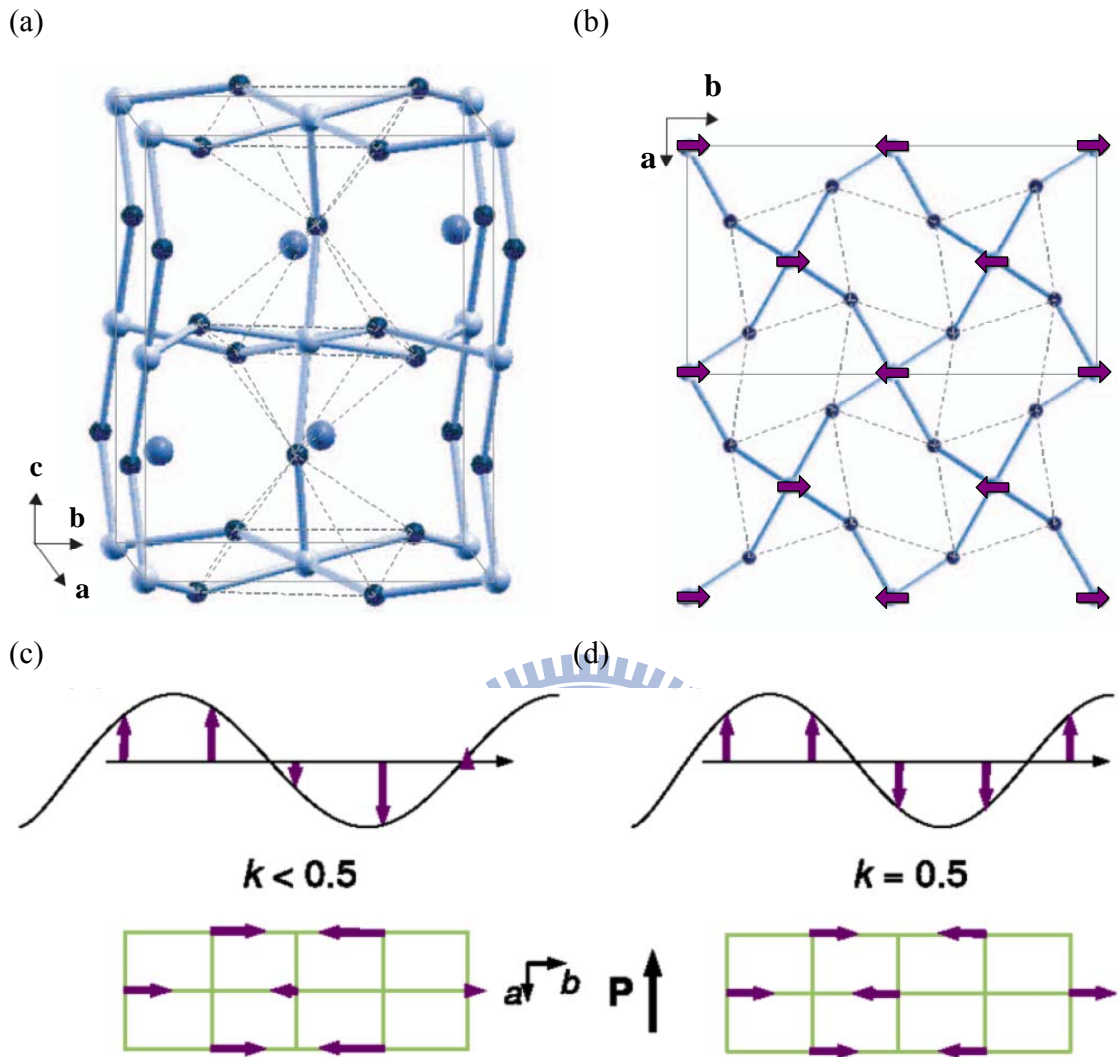


Figure 2.4 (a) The $Pbnm$ orthorhombic cell of $RMnO_3$. Black, white, and gray spheres represent O, Mn, and Ho atoms, respectively. From [12]. (b) ab in-plane view of MnO_2 planes, showing the large octahedral distortions and zigzag spin ordering. Solid lines mark the in-plane projected unit cell. (c) The simple sine-wave magnetic structure of $HoMnO_3$ for $T_L < T < T_N$ (d) The E -phase magnetic structure below T_L . Adopted from [13].

References

- [1] C. Zener, Phys. Rev. **81**, 440 (1951)..
- [2] C. Zener, Phys. Rev. **83**, 299 (1951).
- [3] C. Zener, Phys. Rev. **82**, 403 (1951).
- [4] E. Dagotto *et al.*, “*Nanoscale Phase Separation and Colossal Magnetoresistance: The Physics of manganites and Related Compounds*”, Springer Publishing Company, Inc., 2003, Chap. 2.
- [5] P. W. Anderson and H. Hasegawa, Phys. Rev. **100**, 675 (1955).
- [6] P.-G. de Gennes, Phys. Rev. **118**, 141 (1960).
- [7] B. Lorenz, A.P. Litvinchuk, M.M. Gospodinov, and C.W. Chu, Phys. Rev. Lett. **92**, 087204 (2004)
- [8] 謝志昌，國立交通大學博士論文 (2008).
- [9] B. H. Kim and B. I. Min, Phys. Rev. B **80**, 064416 (2009).
- [10] The term of incommensuration (ICM) means that the spin ordering periodicity is not compatible in a rational manner to the periodicity of the underlying crystal structure.
- [11] A. Muñoz, M. T. Casáis, J. A. Alonso, M. J. Martínez-Lope, J. L. Martínez, and M. T. Fernández-Díaz, Inorg. Chem. **40**, 1020 (2001).
- [12] S. Picozzi, K. Yamauchi, G. Bihlmayer and S. Blügel, Phys. Rev. B **74**, 094402 (2006).
- [13] I. A. Sergienko, C. Sen, and E. Dagotto, Phys. Rev. Lett. **97**, 227204 (2006).

Chapter 3

Experimental procedures

3.1 Preparation and characterization of polycrystalline sample of hexagonal HoMnO_3

3.1.1 Introduction

Multiferroic rare-earth manganites have attracted special attention because of the coexistence of ferroelectric and magnetic orders. This phenomenon resulting from the coupling and mutual interferences of magnetism, ferroelectricity, and/or ferroelasticity has evidently given rise to significant magnetoelectric (ME) effect, which might prove to have profound application potential in the next generation electronics. In particular, it has been demonstrated that, in some multiferroic magnetoelectrics, the magnetization and ferroelectric polarization can be respectively modulated and controlled by electric and magnetic fields. For this reason, information may thus be stored both in the magnetic and electric polarization instead of just the magnetic polarization, and it may also be retrieved by sensing the magnetic moment or ferroelectric polarization. A thorough understanding of the underlying physics of the coupling between these two orders may thus yield the possibility of developing novel devices that will improve memory storage densities.

Rare-earth manganites, RMnO_3 , have an orthorhombic perovskite structure for $\text{R}=\text{La-Dy}$. For rare-earth cation with smaller ionic radius (such as those from Ho to Lu, Y and Sc), the structure changes to a hexagonal structure (space group $P6_3cm$) consisting of layers of corner-sharing distorted and tilted MnO_5 triangular bi-pyramids. These hexagonal manganites can be transformed into the orthorhombic perovskite phases by annealing under high pressure [1, 2]. The early studies carried out on hexagonal manganites showed that they exhibit the feature of geometrical frustration caused by the anti-ferromagnetic ordering of the Mn-spins within a planar triangular lattice with Néel temperature (T_N) ranging from 70 to 130 K [3]. Furthermore, they undergo a ferroelectric transition at high temperatures (600-900 K) [4-6] and negligible interactions between the magnetic and ferroelectric orders are expected. On the contrary, in the orthorhombic perovskites, there is a coexistence of magnetic ordering and ferroelectricity at lower temperatures. In this respect, with the ionic

size sitting right at the orthorhombic and hexagonal phase boundary of perovskite manganites, the HoMnO_3 (HMO) is an ideal candidate to engineer into orthorhombic thin films and to search for emerging physical properties in the *E*-phase magnetic structure. Thus, it is necessary to obtain pure sample of hexagonal HMO, so as to grow excellent orthorhombic HMO thin films using the pulsed laser deposition technique. It is one of the main aims of this dissertation. In this chapter, the magnetic properties of the hexagonal HMO are revisited, and a detailed study of its thermal evolution down to 2 K is presented to delineate the possible moment reorientation of the Mn spins. The possible ordering of the Ho ions is also probed.

3.1.2 Experimental

Pure polycrystalline hexagonal HoMnO_3 (*h*-HMO) was synthesized by solid-state reaction with the nominal stoichiometric amounts of Ho_2O_3 (99.999%), and MnCO_3 (99.95%) powders. First, Ho_2O_3 were preheated to 400 °C for 12 h to remove the adsorptive mist and the desired stoichiometric mixture of Ho_2O_3 , and MnCO_3 were ground thoroughly in an agate mortar. The precursor powder was heated at 1000 °C in air for 16 h, thus yielding a well-crystallized monophase powder. The mixture was pressed and sintered at 1200 °C for 24 h, then ground and pressed again for the subsequent sintering. After repeating the process for 3-4 times, it was pressed into disk for the final sintering carried out at 1200 °C for 24 hours. We broke this bulk, pressed and reheated until the density of the disk tended to saturate. This process usually costs two to three times. For further measurements referred below, parts of this product were initially remained and characterized by laboratory x-ray diffraction (XRD) for phase identification and assessment of phase purity. The susceptibility of the *h*-HMO samples were examined by Superconducting Quantum Interference Device (SQUID).

3.1.3 Results and discussion

HoMnO_3 (HMO) was obtained as black, well-crystallized powder. As is evident in Fig. 3.1, the observed x-ray diffraction peak patterns can be solely assigned to hexagonal structure (space group: $P6_3cm$) without any trace of impurity or additional phases. The

lattice parameters obtained here are $a:c=6.137(4):11.401(2)$ Å, respectively. The lattice constants were confirmed to be closed to those results for ceramic HMO prepared by the solid-state reaction technique [7, 8].

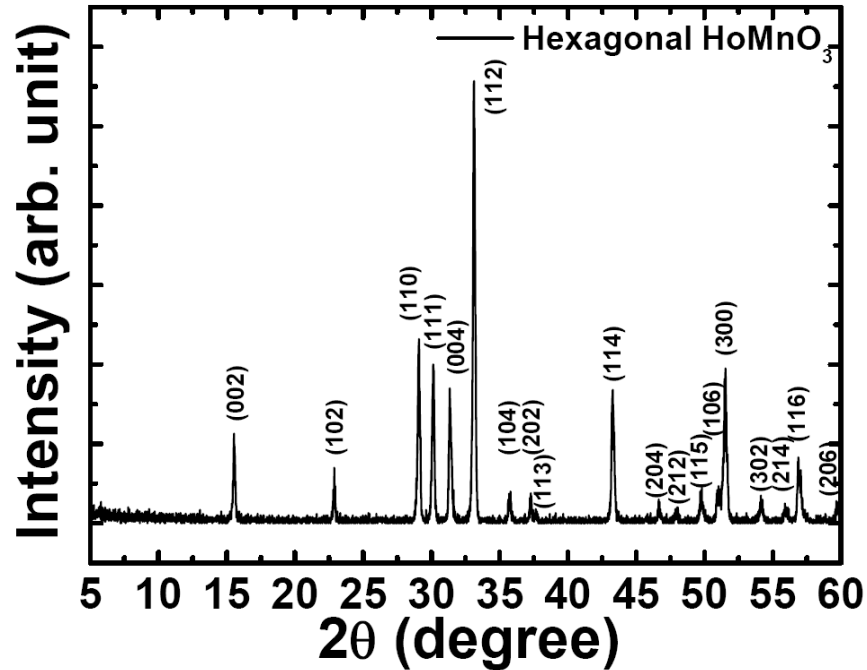
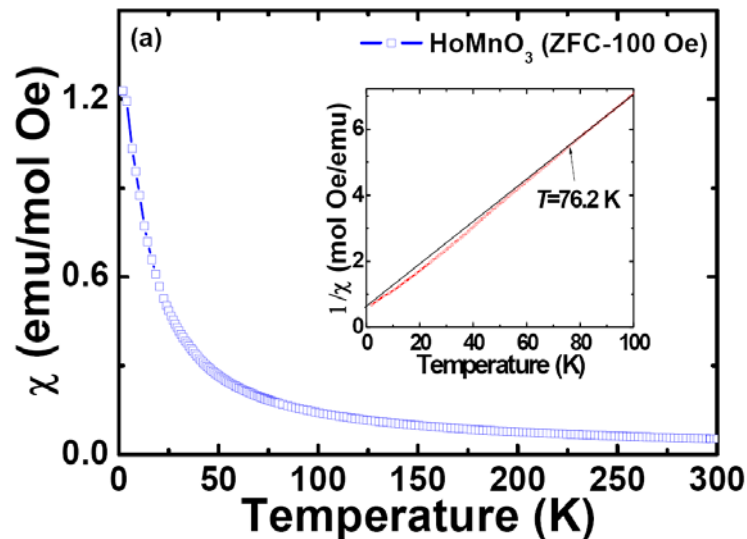


Figure 3.1 The x-ray diffraction patterns of hexagonal HoMnO_3 powder at room temperature. (The bracketed markers correspond to the position of the allowed Bragg reflections.)

In order to unambiguously verify the presence of the magnetic phases in our as-prepared HMO polycrystalline samples, we turn to the preliminary magnetic measurements. Fig. 3.2(a) shows the temperature dependence of the susceptibility ($\chi(T)$) curve measured with an applied magnetic field of 100 Oe under zero-field-cooled (ZFC) condition. The susceptibility increases drastically with decreasing temperature, presumably due to the high paramagnetism of Ho^{3+} magnetic moment [7-10], which might have also masked the possible magnetic transitions for the Mn moments. Thus, we have also plotted the inverse susceptibility against temperature as displayed in the inset of fig. 2(a) to reveal the possible transitions hidden in the paramagnetic background. It is indeed seen that, above 76 K, the linearity of the curve reveals that $\chi(T)$ follows the Curie-Weiss (CW) law in that temperature regime. This curve deviates from the CW law around 76 K, which may be interpreted in terms of the onset of the magnetic order of Mn^{3+} and could be defined as

T_N [7]. Moreover, the second downward deviation of the curve about 40 K suggests that the magnetization is increased by spin-canting as found for *h*-HMO, whose origin is inferred to be the reorientation of Mn magnetic moments [8-9, 11-12]. As can be seen in Fig. 3.2(b), we have shown ZFC and field-cooled (FC) curves in the low-temperature region below 50 K. A noticeable anomaly is observed near 40 K below which the ZFC and FC curves bifurcate. Similar to the data obtained for a single crystal [10], the irreversibility in ZFC and FC curves is observable at the Mn³⁺ spin rotation temperature (T_{SR}) [8] for our specimen at $T_{SR}=40$ K, where Ho³⁺ moments become partially antiferromagnetic (*AF*) ordered [9, 12]. On the other hand, in the inset of Fig. 2(b), near about 4 K ZFC curve shows another anomaly with a sudden decrease in magnetization with decreasing T . This abrupt change corresponds to the temperature of Ho³⁺ *AF* ordering ($T_{Ho}\sim 4$ K) [9], which significantly depends on the cooling condition (i.e., whether the sample is cooled in an applied field or not). It is expected that the Ho atoms adopt an *AF* structure with the moments parallel to the *c*-axis below this transition. However, as far as we know, there were only very few published data that probed the *AF* long range order of rare-earth ion Ho³⁺ at temperatures lower than 4.5 K [10, 12, 13]. This discrepancy can be explained when we consider the effect of random orientation of grains in polycrystalline sample on the magnetic susceptibility.



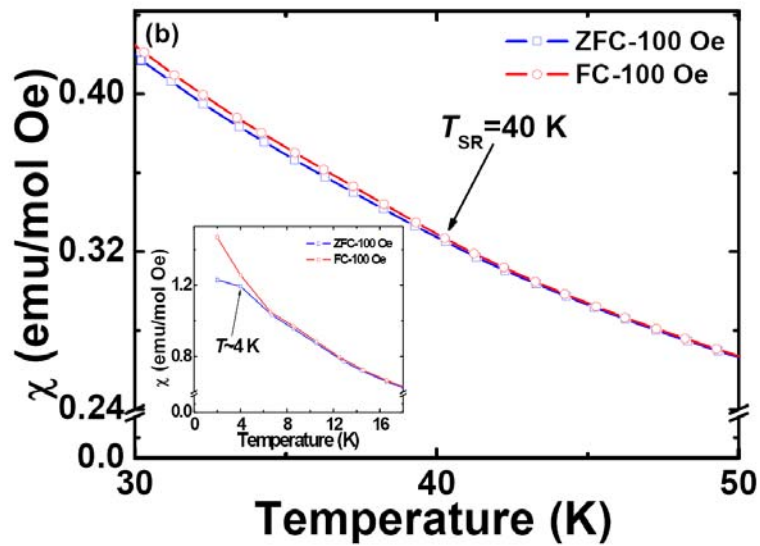
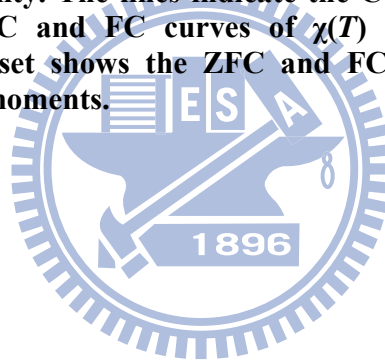


Figure 3.2 (a) Temperature evolution of the zero-field-cooled susceptibility (ZFC- $\chi(T)$) with an applied magnetic field of 100 Oe. The inset shows the temperature-dependent inverse magnetic susceptibility. The lines indicate the Curie Weiss high-temperature extrapolation. (b) The ZFC and FC curves of $\chi(T)$ near the spin reorientation transition of Mn^{3+} . The inset shows the ZFC and FC curves of $\chi(T)$ around AF ordering of Ho^{3+} magnetic moments.



3.2 Epitaxial stabilization of oxide thin films

Epitaxial growth of thin films has been intensively studied over more than half a century. Over the last two-decades, the growth of epitaxial oxide films has become more and more important owing to the discoveries of several prominent multi-elements oxides. The materials of interest are the high T_C superconductors, ferroelectrics, manganites with colossal magnetoresistance, various magnetic oxides, solid electrolytes, wide band-gap luminescent stuff, and others. Interestingly, recent work [14] has shown that two-dimensional electron gases (2DEGs) can also exist at oxide interfaces. These electron gases typically result from reconstruction of the complex electronic structure of the oxides, so that the electronic behavior of the interfaces can differ from the behavior of the bulk. Reports on magnetism [15] and superconductivity [16] in oxide 2DEGs illustrate their capability to encompass phenomena not shown by interfaces in conventional semiconductors. Although new electronic phases formed by electronic reconstruction at oxide interfaces are already fascinating topics from the theoretical point of view, it is especially intriguing that, in recent years, it has become possible to grow a large variety of interfaces with atomic precision by using pulsed laser deposition equipped with reflection high-energy electron diffraction (RHEED).

What is pulsed laser deposition (PLD)? PLD [17] is a physical vapor deposition process for fabricating thin films, which involves evaporation of a solid target in a high vacuum chamber by short (pulse duration ~ 25 ns) and high energy (500 mJ) laser pulses as illustrated in the Fig. 3.3. The most important feature of pulsed-laser-deposition method is that the stoichiometry of the deposited films can be maintained with essentially the same composition as that of the target. This is the result of the extremely high heating rate of the target surface ($\sim 10^8$ K/s) due to pulsed-laser irradiation. It leads to the congruent evaporation of the target irrespective of the vaporization point of the individual constituent element or compound contained in the target. Consequently, high quality samples can be grown reliably in relatively short period of time, typically within 1 hour. Nevertheless, the principle of pulsed-laser deposition is a very complex physical phenomenon. It not only involves the physical process of the laser-material interaction of the impact of high-power pulsed radiation on solid target, but also the formation of the plasma plume with high energetic species and even the transfer of the ablated material through the plasma plume

onto the surface of the heated substrate.

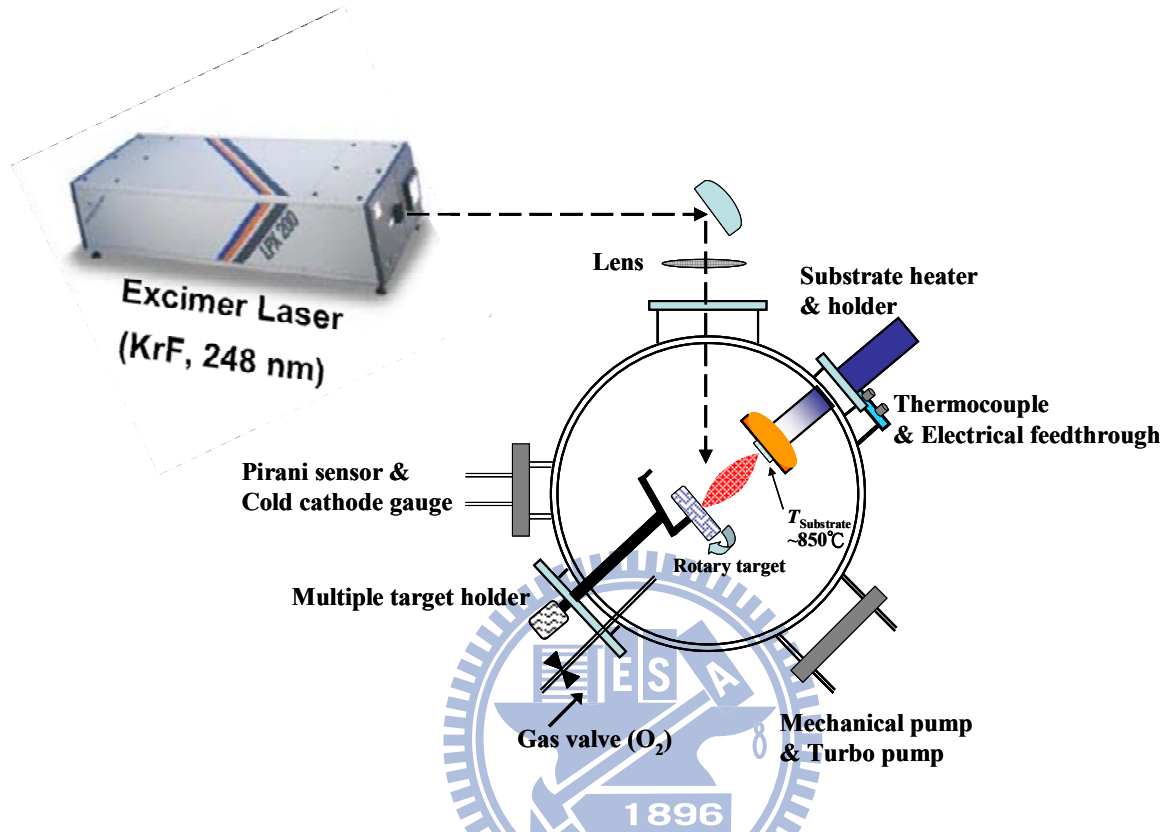


Figure 3.3 Schematics of a typical PLD process: a ceramic target is placed in a vacuum chamber and then a pulsed laser beam is focused onto the surface of the solid target. The strong absorption of the electromagnetic radiation by the solid surface leads to explosive evaporation of the target materials. The evaporated materials essentially form highly energetic and ionized plasma, often referred as “laser plume”.

The structural and dimensional resemblance between the film and the substrate often leads to the formation of coherent or semi-coherent interfaces [18]. The energy of coherent and semi-coherent interfaces is significantly lower than that of non-coherent ones. In this way, the interface formed can affect the choice of the crystallographic structure of the nuclei formed at the early stage of deposition because the system tends to minimize its free energy to reach the equilibrium state. The phenomenon is often referred to as “exptaxial stabilization”, in cases where the composition or crystallographic structure realized in the exptaxial film is different from that of the equilibrium bulk material. In the sequence of $RMnO_3$ compounds, the perovskite phase does not exist under ambient pressure for the rare earth elements with small ionic radius (Y, and Ho-Lu). Polycrystalline *E*-phase magnetic

structure of $RMnO_3$ orthorhombic perovskites was prepared either by high-temperature high pressure [19-21] or by the citrate-based soft chemistry method [22-23]. Nevertheless, the surface contribution to free energy can change the situation- $YMnO_3$ had been reported to adopt the perovskite structure instead of hexagonal one [24].

In this scenario, the epitaxial stabilization of $RMnO_3$ phases ($R=Ho, Y,$ and Lu) in the perovskite form had also been demonstrated to deposit coherently on perovskite $LaAlO_3$ and $SrTiO_3$ substrates by using metal organic chemical-vapor deposition (MOCVD) [25]. However, it is extremely difficult to obtain thin films with distinctly resolved growth directions which are capable of revealing the relevant properties along the respective crystallographic orientations. For instance, the (110)-oriented orthorhombic $HoMnO_3$ (o -HMO) thin films had been reported in Ref. 25. In the latter part of this chapter, we will briefly describe the growth of high-quality (010), (001), and (100)-oriented o -HMO thin films by pulsed laser deposition (PLD). Above-mentioned Fig. 3.3 shows the PLD system for preparing various-orientation o -HMO thin films in this dissertation. Due to the mechanism of pulsed laser deposition [17], the fabricating time of a thin film can be greatly reduced and the complex stoichiometries also can be completely transferred from the target to the substrate provided the optimum deposition pressure and temperature are carefully adjusted. The characteristics of various-orientation o -HMO thin films were examined by these measurable procedure referred to the Fig. 3.4. Additionally, the crystal structure, surface roughness, magnetic properties, and magnetoelectric response of these samples will be presented in the next chapter. The distinctly-oriented o -HMO thin films are epitaxial stabilized on the respective substrates and the details for each one are given as follows.

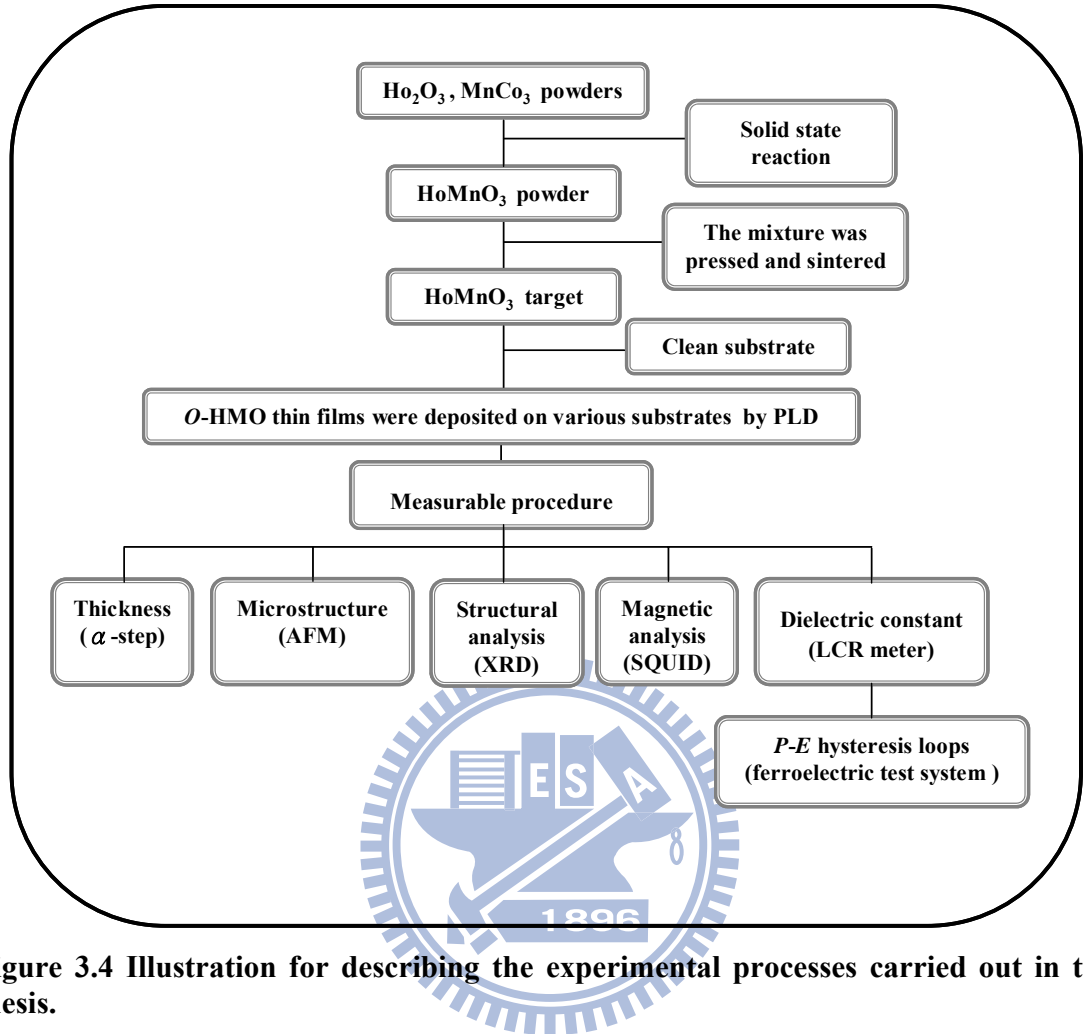


Figure 3.4 Illustration for describing the experimental processes carried out in this thesis.

3.2.1 The *b*-axis-oriented *o*-HoMnO₃ thin films

Because of the small ionic size of the Ho³⁺, *o*-HMO is structurally highly distorted with lattice constants of $a = 5.26 \text{ \AA}$, $b = 5.84 \text{ \AA}$, and $c = 7.36 \text{ \AA}$ (in *Pbnm* setting), respectively [26]. Thus, in order to stabilize the phase and epitaxially grow *o*-HMO films with controllable orientations, it is crucial to select the suitable substrates. In this work, we chose the LAO(110) substrates. The lattice constants along the $[1\bar{1}0]$ and $[001]$ directions of LAO are 5.358 \AA and 7.578 \AA , respectively [27], thus are quite suitable to accommodate the *ac*-plane of *o*-HMO as shown in the Fig. 3.5(a). Sintered ceramic pellet of stoichiometric HoMnO₃ was prepared by conventional solid-state reaction method and used as a target for the subsequent pulsed laser deposition (PLD), which was carried out using a 248 nm KrF excimer laser operated at a repetition rate of 3 Hz with an energy density of

2-4 J/cm². The substrate temperature and oxygen pressure were optimized at $T_s = 850^\circ\text{C}$ and $P(\text{O}_2) = 0.1$ Torr, respectively. The film thickness was around 180 nm. After the deposition, the film was cooled in 600 Torr of oxygen to room temperature with the heater off. These processes have not only successfully grown the pure (0*k*0)-oriented *o*-HMO phase but also improved the in-plane alignment.

3.2.2 The *c*- axis-oriented *o*-HoMnO₃ thin films

As displayed in Fig. 3.5(b), the (00*l*)-oriented HMO thin films were grown on (001) SrTiO₃ (STO) substrates by PLD using a KrF excimer laser (wavelength 248 nm and pulse duration about 30 ns) operating at a repetition rate of 3 Hz and the energy density was around 2-4 J/cm². The oxygen partial pressure during deposition was maintained at 0.1 Torr. The substrate temperature was kept at 850°C for obtaining 180 nm-thick *c*-axis-oriented *o*-HMO thin films deposited on STO substrate. After the deposition, the film was cooled in 600 Torr of oxygen to room temperature with the heater off.

3.2.3 The *a*- axis-oriented *o*-HoMnO₃ thin films

Finally, we turn to the case of the *a*-axis-oriented *o*-HMO thin films grown on the STO(110) substrates. As depicted schematically in Fig. 3.5(c), there are two most likely matching schemes that accommodate the lattice of *o*-HMO on the STO(110) substrate. Since at the lower substrate temperatures the films appear to be mixed with (0*k*0)-phase, we will discuss only the optimized case. For growing the *a*-axis-oriented thin films, a 248 nm KrF excimer laser was operated with an energy density of 2-4 J/cm² at a repetition rate of 3 Hz. During the deposition process, the growth temperature and oxygen pressure were optimized at $T_s = 880^\circ\text{C}$ and $P(\text{O}_2) = 0.1$ Torr, respectively. The film thickness was estimated to be about 100 nm. After the deposition, the film was cooled in 650 Torr of oxygen to room temperature with the heater off. In above-mentioned case, since the film is *a*-axis oriented, the plausible lattice matching schemes would be the one depicted in the left panel of Fig. 3.5(c). Consequently, one expects that not only substrate will favor the growth of (*h*00)-oriented *o*-HMO films but also will result in a nearly perfect epitaxial relationship.

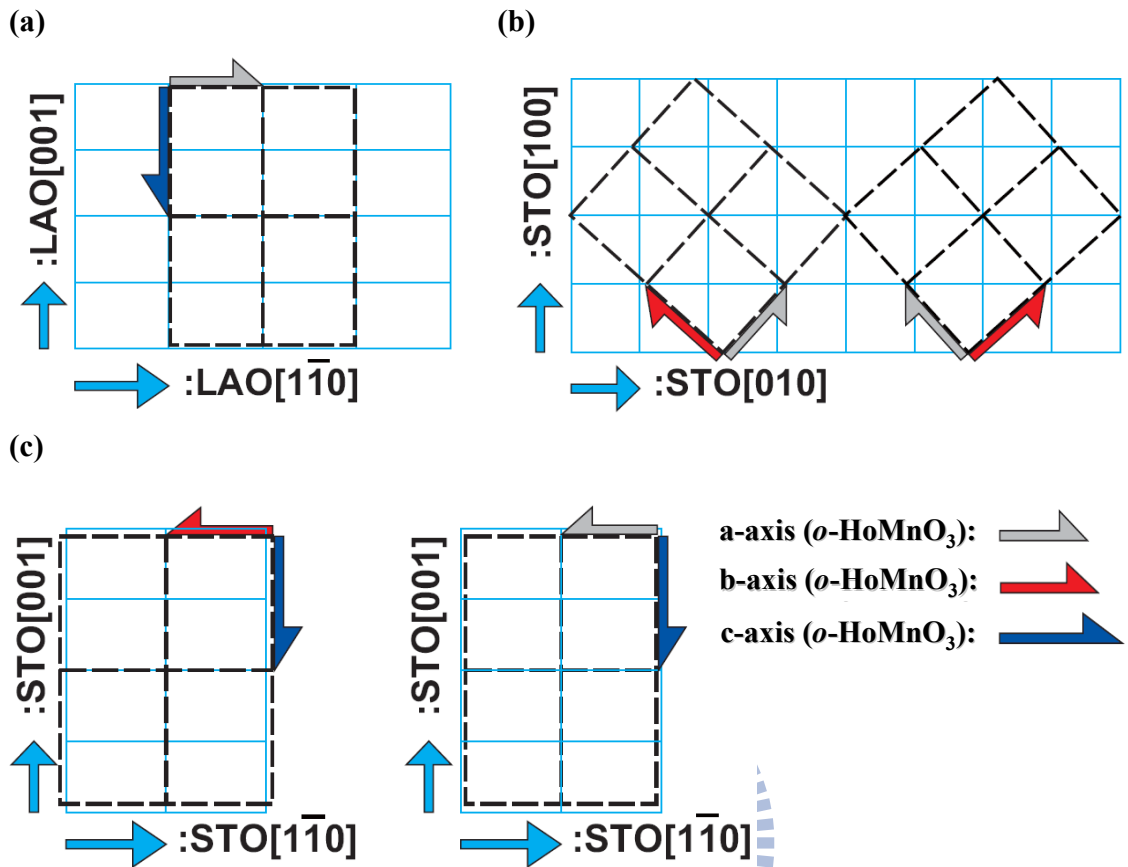


Figure 3.5 The schematics of the in-plane arrangements between the *o*-HMO thin films and substrates. (a) *o*-HMO (0*k*0)/LAO(110): *c*-axis and *a*-axis of *o*-HMO are aligned with LAO[001] and LAO[110], respectively; (b) *o*-HMO (00*l*)/STO(001): *a*-*b* diagonal of *o*-HMO is aligned randomly with STO [010] substrate direction, one expects that a twin-like structure might occur in these *o*-HMO (00*l*) films; and (c) in-plane schemes of *o*-HMO thin films on STO(110) showing that the *c*-axis of *o*-HMO is aligned with STO[001], but *a*-axis or *b*-axis can be randomly aligned with STO[110]. Adopted from [28].

References

- [1] A. Waintal, and J. Chenavas, J. Mater. Res. Bull. **2**, 819 (1967).
- [2] V. E. Wood, A. E. Austin, E. W. Collings, and K. C. Brog, J. Phys. Chem. Solids **34**, 859 (1973).
- [3] W. C. Koehler, H. L. Yakel, E. O. Wollan, and J. W. Cable, Phys. Lett. **9**, 93 (1964).
- [4] G. A. Smolenskii, and I. E. Chupis, Sov. Phys.-Usp. **25**, 475 (1982).
- [5] I. G. Ismaelzade, and S. A. Kizhaev, Sov. Phys. Solid State **7**, 236 (1965).
- [6] N. Iwata, and K. Kohn, J. Phys. Soc. Japan **67**, 3318 (1998).
- [7] K. Yoshii, and H. Abe, J. Solid State Chem. **165**, 131 (2002).
- [8] E. Galstyan, B. Lorenz, K. S. Martirosyan, F. Yen, Y. Y. Sun, M. M. Gospodinov, and C. W. Chu, J. Phys.: Condens. Matter **20**, 325241 (2008).
- [9] A. Munoz, J. A. Alonso, M. J. Martinez-Lope, M. T. Casais, J. L. Martinez, and M. T. Fernandez-Diaz, Chem. Mater. **13**, 1497 (2001).
- [10] A. Midya, P. Mandal, S. Das, S. Banerjee, L. S. Sharath Chandra, V. Ganesan, and S. Roy Barman, Appl. Phys. Lett. **96**, 142514 (2010).
- [11] B. Lorenz, A. P. Litvinchuk, M. M. Gospodinov, and C. W. Chu, Phys. Rev. Lett. **92**, 087204 (2004).
- [12] B. Lorenz, F. Yen, M. M. Gospodinov, and C. W. Chu, Phys. Rev. B **71**, 014438 (2005).
- [13] H. Sugie, N. Iwata, and K. Kohn, J. Phys. Soc. Japan **71**, 1558 (2002).
- [14] A. Ohtomo, and H. Y. Hwang, Nature **427**, 423 (2004).
- [15] A. Brinkmann, M. Huijben, M. Van Zalk, J. Huijben, U. Zeitler, J. C. Maan, W. G. Van Der Wiel, G. Rijnders, D. H. A. Blank, and H. Hilgenkamp, Nature Mater. **6**, 493 (2007).
- [16] N. Reyren, S. Thiel, A. D. Caviglia, L. Fitting Kourkoutis, G. Hammerl, C. Richter, C. W. Schneider, T. Kopp, A.-S. Rüetschi, D. Jaccard, M. Gabay, D. A. Muller, J.-M. Triscone, and J. Mannhart, Science **317**, 1196 (2007).
- [17] D. B. Chrisey and G. K. Hubler, "*Pulsed laser deposition of thin films*", John Wiley & Sons, New York, 1994.
- [18] Fully coherent interfaces are those where there is complete continuity of atomic planes

and lines across the interface between two phases. Semi-coherent interfaces are those in which the disregistry between two crystal structures across the interface is accommodated by periodic misfit dislocations in the interface; A. R. Wildes, J. Mayer, and K. Theis-Bröhl, *Thin Solid Films* **401**, 7 (2001).

- [19] B. Lorenz, Y. -Q. Wang, and C. W. Chu, *Phys. Rev. B* **76**, 104405 (2007).
- [20] F. Ye, B. Lorenz, Q. Huang, Y. Q. Wang, Y. Y. Sun, C. W. Chu, J. A. Fernandez-Baca, P. Dai, and H. A. Mook, *Phys. Rev. B* **76**, 060402(R) (2007).
- [21] B. Lorenz, Y. Q. Wang, Y. Y. Sun, and C. W. Chu, *Phys. Rev. B* **70**, 212412 (2004).
- [22] J.-S. Zhou and J. B. Goodenough, *Phys. Rev. Lett.* **96**, 247202 (2006).
- [23] H. W. Brinks, J. Rodríguez-Carvajal, H. Fjellvåg, A. Kjekshus, and B. C. Hauback, *Phys. Rev. B* **63**, 094411 (2001).
- [24] X. Martí, F. Sánchez, V. Skumryev, V. Laukhin, C. Ferrater, M. V. García-Cuenca, M. Varela, and J. Fontcuberta, *Thin Solid Films* **516**, 4899 (2008).
- [25] A. A. Bosak, A. A. Kamenev, I. E. Graboy, S. V. Antonov, O. Yu. Gorbenko, A. R. Kaul, C. Dubourdieu, J. P. Senateur, V. L. Svechnikov, H. W. Zandbergen, and B. Holländer, *Thin Solid Films* **400**, 149 (2001).
- [26] A. Alonso, M. J. Martínez-Lope, M. T. Casais, and M. T. Fernández-Díaz, *Inorg. Chem.* **39**, 917 (2000).
- [27] S. C. Chae, Y. J. Chang, S. S. A. Seo, T. W. Noh, D.-W. Kim, and C. U. Jung, *Appl. Phys. Lett.* **89**, 182512 (2006).
- [28] C. C. Hsieh, T. H. Lin, H. C. Shih, C.-H. Hsu, C. W. Luo, J.-Y. Lin, K. H. Wu, T. M. Uen, and J. Y. Juang, *J. Appl. Phys.* **104**, 103912 (2008).

Chapter 4

Magnetoelectric properties of orthorhombic HoMnO_3 thin films with various orientations

4.1 Anomalous magnetic ordering in b -axis-oriented HoMnO_3 thin films

In this section, we briefly describe the growth of the orthorhombic HoMnO_3 films with well-aligned crystallographic orientations by using pulsed laser deposition. The nearly perfect b -axis-oriented films provide the opportunity of investigating the orientation-dependent physical property of this material. The temperature dependent magnetization evidently displays an antiferromagnetic ordering near 42 K, irrespective to the direction of applied field. Furthermore, the theoretically expected lock-in transition was clearly observed at around 30 K when field was applied along the c -axis and was undetectable along a - and b -axis. The 30 K-transition was suppressed to 26 K when the applied field increased from 100 Oe to 500 Oe.

4.1.1 Probing the anisotropic characterization of orthorhombic HoMnO_3 thin films

Multiferroic materials with magnetic ordering-induced improper ferroelectricity have been of significant research interest owing to the intriguing underlying physics and the anticipated multifunctional applications for next generation electronics [1-5]. In particular, Sergienko et al. [6] have theoretically predicted that the double-exchange driven polar displacement manifested in the E -type magnetic structure of orthorhombic HoMnO_3 (o -HMO) and possibly other similar compounds might give rise to a ferroelectric polarization orders of magnitude larger than those exhibited in helical magnetic ordering-induced ferroelectricity. Unfortunately, o -HMO is not the thermodynamically stable phase at the ambient conditions, thus the few available reported results were all obtained from polycrystalline samples prepared either by high-temperature high-pressure

synthesis [7-10] or by the citrate-based soft chemistry method [11,12]. For these samples, the neutron scattering [12] showed that *o*-HMO indeed exhibited an incommensurate (IC) antiferromagnetic (*AFM*) transition around 42 K and at lower temperatures the magnetic order locks into a temperature-independent commensurate wave vector as expected. However, the minute ferroelectric polarization ($P \approx 20\text{-}90 \mu\text{C}/\text{m}^2$) derived from pyroelectric current measurements and the suggestive involvement of Ho^{3+} moments in the low temperature dielectric anomalies had stirred debates about the relevant physical mechanisms [7,13]. Since within the frameworks of various microscopic mechanisms the magnetic ordering and associated ferroelectricity are intimately related to specific crystallographic orientations, consequently in order to gain more insight toward understanding these intriguing physical properties, it is essential to obtain samples capable of revealing the relevant properties along the respective crystallographic orientations. In this chapter, we report the magnetization behaviors of the collinear *E*-type magnetic phase with the field applied along the respective crystallographic orientations, which is realized by courtesy of the success of growing the well-aligned *b*-axis-oriented *o*-HMO films on $\text{LaAlO}_3(110)$ (LAO(110)) substrates.

4.1.2 Results and Discussion

Fig. 4.1(a) shows the θ - 2θ XRD scans for the as-deposited *o*-HMO films on LAO(110) substrates. The diffraction peaks reveal pure (020)-oriented *o*-HMO reflections without discernible impurity phase, indicating the formation of a pure *o*-HMO. The inset of Fig. 4.1(a) exhibits the rocking curve of the (020) peak, displaying a full width of half maximum of 0.68° . Furthermore, as shown in Fig. 4.1(b), the ϕ -scan of the (110) reflection of the *o*-HMO displays a clear twofold symmetry, indicating that the films were indeed epitaxial and well-aligned with the substrate. We note that the nearly perfect epitaxial relation between *o*-HMO(110) and LAO(010) peaks shown in Fig. 4.1(b) is quite consistent with the expected lattice mismatches of -2.95 % along the [001] direction and -1.91 % along the $[\bar{1}10]$ direction for growing *o*-HMO on the LAO(110) substrates. The lattice constants obtained here are $a = 5.28 \text{ \AA}$, $b = 5.80 \text{ \AA}$, and $c = 7.51 \text{ \AA}$, respectively. Compare to $a = 5.26 \text{ \AA}$, $b = 5.84 \text{ \AA}$, and $c = 7.36 \text{ \AA}$ for the bulk *o*-HMO, it is clear that the film is

under tensile strain within the ac -plane and compressive along the b -axis, even when its thickness reaches 180 nm.

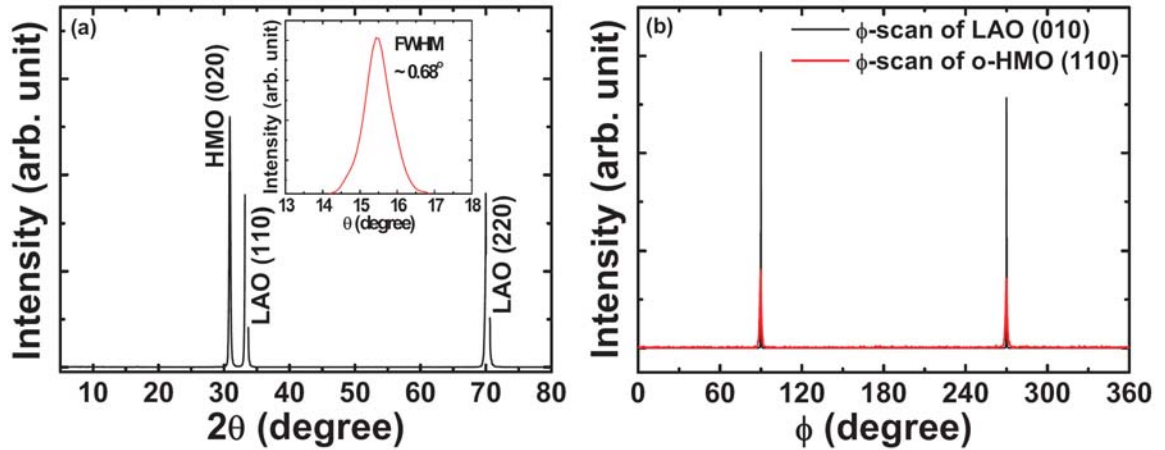


Figure 4.1: (a) The typical θ - 2θ diffraction pattern of o -HMO films grown on LAO(110) substrate. The inset in (a) shows the rocking curve of the o -HMO (020) peak. (b) The azimuthal ϕ -scans of the (110) peak of the o -HMO films, displaying the nearly ideal alignment of crystallographic orientations between film and substrate.

Fig. 4.2 shows the AFM image of the o -HMO displaying the elongated but uniform grain morphology. Since the LAO(110) substrate has slightly larger lattice constants than that of the o -HMO [12], significant in-plane tensile strain is expected to accumulate with increasing film thickness. The fact that no micro-cracks or voids were observed suggests the spindle-like grains of the o -HMO film must have aligned along specific crystallographic directions of the LAO substrate and the growth might have been accompanied by significant uniform strain. From the previous analyses, we schematically depict the elongated axis and short axis of the grains as being along a - and c -axis of o -HMO, respectively. Perhaps, the most significant implication of the present results is that it allows us to probe the physical properties of the o -HMO along different major crystal orientations.

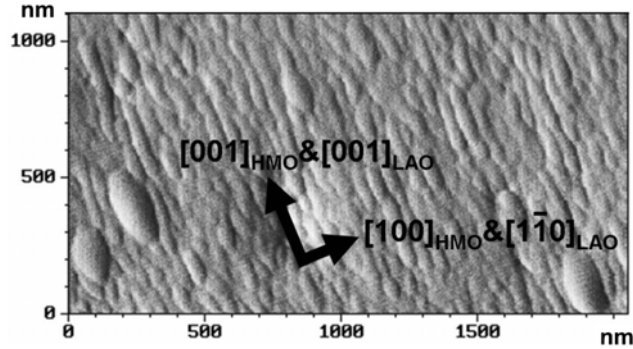


Figure 4.2 The AFM image of a 180 nm-thick *o*-HMO film deposited on LAO(110) substrate. The arrows indicate the growth direction of *o*-HMO grains.

Fig. 4.3(a) shows the temperature dependent magnetization ($M(T)$) behaviors probed by the zero-field-cooled (ZFC) scheme with an 100 Oe field applied along different crystal orientations. As is evident in Fig. 4.3(a), all the three ZFC $M(T)$ curves clearly exhibit an ordering transition near 42 K, which is consistent with the recent neutron diffraction results [11,12,16] and can be assigned as the usual *AFM* ordering of Mn moment for *o*-HMO. Another feature to be noted in Fig. 4.3(a) is the significantly larger magnetization level along the *b*-axis over the whole temperature range. According to the neutron diffraction results [12], the magnetic ordering of the Mn^{3+} ions is uniaxial, and the moments are parallel to the *b* direction, making the *b*-axis the easy axis in the *Pbnm* group symmetry setting. Thus explains that, in the entire temperature range, the magnetization along the *b*-axis is larger than that along *a*- or *c*-axis. At lower temperatures, however, the magnetic moment of Ho^{3+} will eventually come into play below $T = 20\sim 25$ K [12]. The latter might account for the enhancement of the *a*-axis magnetization for $T < 25$ K. Finally, we note that around 30 K an interesting anomaly in the *c*-axis $M(T)$ curve signifying a second ordering transition is clearly observed. Although, it is tempting to identify it as the lock-in temperature (T_L) of the incommensurate-commensurate transition to conform to previous theoretical [6] and experimental [7] anticipations, there are, nevertheless, several points needed to be clarified. Firstly, this second ordering occurs only along the *c*-axis and is undetectable in either *a*- or *b*-axis, which is in contrast to the generally conceived scenario of regarding the collinear Mn^{3+} moments being aligned within the *a-b* plane (*Pbnm* space group setting). Secondly, the ordering temperature (30.4 K) is much higher than the Ho^{3+} moments ordering temperature (11-15 K) [7,12], thus preventing it from being relevant to

Ho³⁺ ordering [7]. Thirdly, despite of the abovementioned inconsistencies, we note that it is, nevertheless, consistent with the neutron diffraction results reported by Brinks et al. (left inset of Fig. 5 in Ref. 11), in that an abrupt increase in magnetic reflection along [001] of *o*-HMO was clearly observed, which disappeared when measured along [011].

In order to further examine this anomalous *c*-axis magnetization, we plot the results measured at 100 Oe and 500 Oe in Fig. 4.3(b) for comparison. As is evident from the results the *AFM* ordering remains around 42 K (see also the 500 Oe FC and ZFC results shown in the inset of Fig. 4.3(b)). However, the 30 K transition has been pushed down to about 26 K with a much broadened feature by merely increasing the measuring field from 100 Oe to 500 Oe. Although field-induced suppression of the lock-in temperature has been observed previously [17], the fields involved, however, were all in the order of Tesla and the suppression was much less significant than the present case. It appears that, whatever this magnetic ordering might be, it is very susceptible to the applied field.

Perhaps, the most intriguing question to be asked here is whether this anomalous *c*-axis magnetic ordering has anything to do with the ferroelectric polarization? According to the recent first-principle calculations [13], in *o*-HMO, the multiferroicity could be driven simultaneously by both lattice and electronic mechanisms, albeit the ordering was assumed to occur within the *a-b* plane (*a-c* plane in *Pnma* space group setting used in Ref. 13). Thus, it could be that the magnetic ordering in *c*-axis somehow distorts the lattice, which in turn induces the lock-in transition in *b*-axis and the associated polarization along *a*- and *c*-axis. In any case, further investigations are certainly needed to delineate these interesting phenomena.

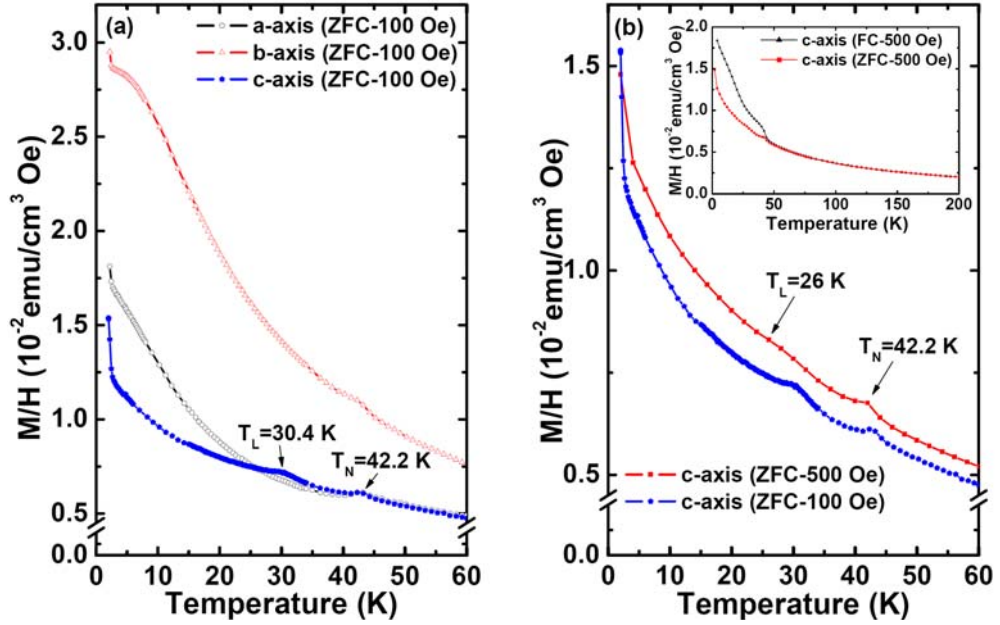


Figure 4.3 (a) The zero-field-cooled temperature-dependent magnetizations (ZFC- $M(T)$) for *o*-HMO film probed along different crystal orientations with an applied magnetic field of 100 Oe. (b) The ZFC- $M(T)$ along the *c*-axis measured at 100 Oe and 500 Oe. The inset in (b) shows full temperature range of the FC- and ZFC- $M(T)$ measured at 500 Oe. Notice the 30 K anomalous ordering along the *c*-axis and the significant suppression of it by applying merely 500 Oe.

4.1.3 Summary

In summary, we have grown *o*-HMO films with well-aligned crystallographic orientations on LAO(110) substrates by PLD. The samples provide the possibility of accessing the orientation-dependent physical properties of this system. The $M(T)$ measurements showed that, in addition to the 42 K *AFM* ordering expected for the *o*-HMO, an anomalous *c*-axis magnetic ordering near 30 K was evidently observed. This ordering temperature, although coincides very well with the lock-in temperature associated with the incommensurate-commensurate magnetic ordering transition revealed by neutron diffraction and dielectric constant anomaly, is, however, very susceptible to applied field. Furthermore, the temperature is well above and should be irrelevant to the ordering temperature of Ho^{3+} moments. Finally, the fact that the ordering occurs along the *c*-axis (in *Pbnm* setting) is surprising and certainly demands further extensive studies.

4.2 Strain-induced effects on antiferromagnetic ordering and magnetocapacitance in orthorhombic HoMnO₃ thin films

In this section, we investigated the magnetic and ferroelectric properties of the *c*-axis-oriented orthorhombic phase HoMnO₃ (*o*-HMO in *Pbnm* symmetry setting) thin films grown on Nb-doped SrTiO₃(001) substrates. The *o*-HMO films exhibit an antiferromagnetic ordering near 42 K, irrespective to the orientation of the applied field. However, an additional magnetic ordering occurring around 35 K was observed when the field was applied along the *c*-axis of *o*-HMO, which was absent when the field was applied in *ab*-plane. The magnetocapacitance measured along the *c*-axis showed that, although there is evidence of dielectric constant enhancement when the temperature is below 35 K, the expected abrupt change in dielectric constant appears at a much lower temperature and reaches maximum around 13.5 K, indicating that the low temperature *c*-axis polarization might be related to the ordering of Ho³⁺ moment. The lattice constant analyses using x-ray diffraction and the observation of a slight magnetization hysteresis suggest that the weak second magnetic transition along the *c*-axis at 35 K might be more relevant to the strain-induced effect on antiferromagnetism.

4.2.1 Directly probing the magnetoelectric coupling in orthorhombic HoMnO₃ thin films

The rich physics and potential practical applications involved in manipulating the coupling between the magnetic and ferroelectric orders existent in multiferroic rare-earth manganites (*RMnO*₃) have evoked tremendous research interest recently [1, 2, 4-5]. Unfortunately, for most hexagonal *RMnO*₃, since the ferroelectricity and magnetism are originated independently, the antiferromagnetic (*AFM*) Néel temperature (T_N) and ferroelectric (FE) Curie temperature (T_C) usually are very far apart (e.g. for *YMnO*₃, $T_C \approx 900$ K and $T_N \approx 70$ K), resulting in virtually no coupling between the two orders. However, very recently it was reported that for orthorhombic *TbMnO*₃, not only $T_C \approx 30$ K is lower than $T_N \approx 40$ K, but also the FE ordering is evidently driven by transition between specific

configuration of magnetic structures [1, 18]. This so-called improper magnetic ferroelectricity [5, 6] is of particular interest because it represents the possibility of manipulating magnetic order (polarization) by applying electric (magnetic) field. Indeed, the switching of the electric polarization by a magnetic field has been demonstrated in single crystal orthorhombic TbMnO₃ [1]. The microscopic origin of ferroelectricity in orthorhombic TbMnO₃ results from a “lock-in” transition of a collinear incommensurate sinusoidal magnetic order to a spiral magnetic order at some temperature below T_N in frustrated magnets [19]. However, the spiral magnetic structure is not the only source of magnetic ferroelectricity. In particular, the magnitude of FE polarization along a -axis (in $Pbnm$ group symmetry setting) in the E -type orthorhombic HoMnO₃ (o -HMO) has been theoretically estimated to be about two orders of magnitude larger than those exhibited in helical magnetic ordering-induced ferroelectricity [6, 13]. However, experimental confirmation of this extraordinary enhancement of the magnetic order-induced FE polarization along a -axis in E -type orthorhombic RMnO₃ has been hampered by the lack of suitable samples available.

For RMnO₃ manganites with the rare-earth ionic size smaller than that of Dy the thermodynamically stable phase are the hexagonal ones [20]. Thus, for example, the o -HMO samples obtained previously were prepared either by the soft chemical procedures [11-12, 14] or by high pressure synthesis [7, 9-10] and were all inevitably polycrystalline in nature. This, in turn, has limited the capability of direct testing on the predicted properties. The temperature dependent FE polarization obtained from the high-pressure synthesis o -HMO samples, though clearly displayed a mild enhancement below the lock-in temperature of Mn³⁺, the magnitude was about 2-3 orders of magnitude smaller than expected [7]. There is, however, an abrupt increase in FE polarization around 15 K, at which the Ho moments rotate in the ab -plane and form a noncollinear magnetic structure. The involvement of the rare-earth moment in inducing the magnetic ferroelectricity, thus, appears to be indispensable [7, 21]. In order to understand these intriguing correlations between the spin, charge and lattice degree of freedoms, it is essential to have the handle of probing the relevant physical properties along specific crystallographic orientations. Very recently we have grown the well-aligned o -HMO thin films on various substrates, which revealed the magnetic ordering anisotropy along the principal crystal axes [22]. However,

the insulating nature of the substrates has been hindering the direct measurement of polarization associated with the magnetic orderings. Here we report an attempt of using the conductive Nb-doped SrTiO₃(001) (Nb:STO) for preparing the epitaxial *o*-HMO thin films. The resultant *c*-axis oriented *o*-HMO film allows direct measurements of the dielectric properties along the *c*-axis and the magnetic property anisotropy along the *c*-axis and in the *ab*-plane. Our data confirm again a possible magnetic ordering transition occurring around 35 K along the *c*-axis as previously delineated in a *b*-axis oriented *o*-HMO film [22]. The lattice constant analyses as well as the hysteretic field-dependent magnetization (*M-H* curve) (see below) suggest that the second Mn³⁺ moment ordering along the *c*-axis might be more relevant to the distortion-induced effect, although in the *E*-type *o*-HMO neither lock-in magnetic ordering nor FE polarization was anticipated to take place along the *c*-axis [6, 13]. Moreover, the results also reveal unexpected FE order appearing along *c*-axis, which peaks around 13.5 K and is indicative of the involvement of the rear-earth moment ordering in stabilizing the FE order [7, 21].

4.2.2 Results and Discussion

Fig. 4.4(a) shows the X-ray diffraction (XRD) θ - 2θ pattern for the obtained *o*-HMO films grown on Nb:STO(001) substrate. The XRD data evidently confirm the formation of the pure orthorhombic HoMnO₃ with the *c*-axis (space group: *Pbnm*) oriented normal to the film surface. The inset of Fig. 4.4(a) displays the rocking curve (ω -scan) of the (004) reflections. The full width at half maximum (FWHM) ($\approx 0.61^\circ$) indicates the good crystalline quality and grain alignment of the *o*-HMO films. To further examine the in-plane texture of the films, we also measured the ϕ -scan around the *o*-HMO (202) reflection. As shown in Fig. 4.4(b), the ϕ -scans display an evenly behaved four-fold symmetry, indicating that the in-plane grain alignment is randomly mixed in the *ab*-plane.

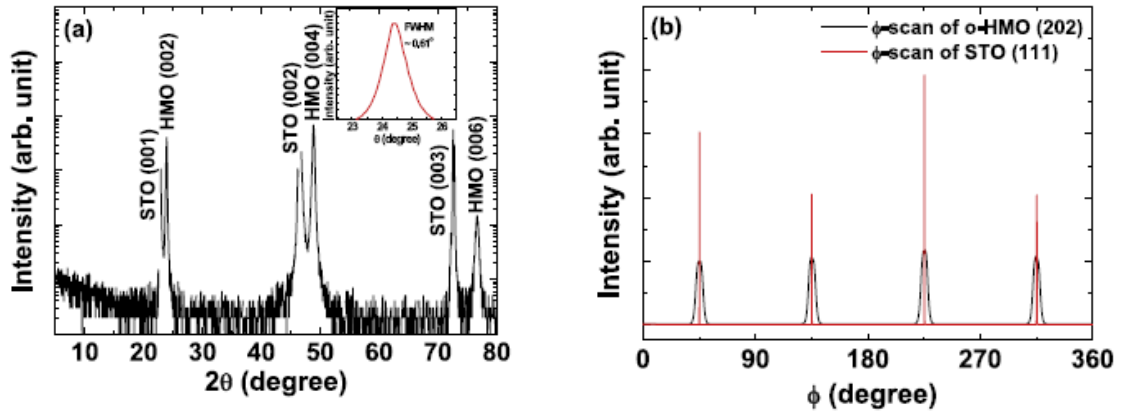


Figure 4.4 The XRD results of the *o*-HMO thin films grown on Nb:STO(001) substrates. (a) The θ - 2θ scans (intensity plotted in logarithmic scale) reveal that HMO films are indeed orthorhombic with nearly perfect *c*-axis oriented characteristic. The inset shows the rocking curve of the *o*-HMO (004) peak. (b) The ϕ -scan plot of the (202) peak of the *o*-HMO films indicates a clear fourfold symmetry, suggesting that the film is well-aligned along (001)-orientation, however, is of *ab* mixing character in film plane.

Figure 4.5(a) shows the temperature dependence of magnetization $M(T)$ for the *o*-HMO measured with an external field of 100 Oe applying either in the *ab*-plane or along the *c*-axis. The zero-field-cooled (ZFC) and field-cooled (FC) $M(T)$ curves all show a clear transition around 43.2 K in both field directions. It is noted that the sharp rise in the magnetization near $T = 43.2$ K in the field-cooled (FC) $M(T)$ curves in both directions is somewhat deviating from the standard *AFM* transitions. One of the possible origins of this magnetization enhancement below the Néel temperature T_N is the uncompensated *AFM* spins existing in the vicinity of the domain boundaries between the *AFM* domains. For instance, weak ferromagnetism is frequently observed in the *AFM* nanoparticles [23-24], due to the significant fraction of uncompensated spins produced by the high surface/volume ratio of the nanoparticles. Alternatively, the weak ferromagnetism can also result from the canted *AFM* state, in that a relatively abrupt magnetization is expected. Either the uncompensated spin or the canted *AFM* state will presumably result in the hysteretic field-dependent magnetization (M - H curve).

In addition to the magnetization enhancement described above, a closer look at the data further reveals that, when the field was applied along the *c*-axis, the ZFC- $M(T)$ clearly exhibits another magnetization anomaly at $T_{MA} \sim 35$ K. This feature, nevertheless, is undetectable in the *ab*-plane ZFC- $M(T)$ (Fig. 4.5(b)). This is consistent with the results

observed in the b -axis-oriented o -HMO films [22], where a similar secondary magnetic ordering was observed around 30.4 K, when the field was applied along the c -axis. According to the neutron diffraction results obtained from polycrystalline o -HMO samples, the Mn^{3+} spin moments exhibit an incommensurate AFM (ICM- AFM) ordering with sinusoidal modulation around 42 K, which locks into a commensurate (CM) E -type at a lower temperature T_L ($T_L \sim 26 - 29.6$ K) with a constant magnetic modulation wave vector ($k_b = 1/2$) propagating along the b -axis [9, 11-12]. Although it is tempting to associate the observed c -axis magnetic ordering anomaly with the lock-in transition between the ICM-CM magnetic structures, since it was not observed in the polycrystalline o -HMO samples and there has been no theoretical model predicting a c -axis magnetic ordering for o -HMO [6, 13, 25], we believe that other origin should be responsible. Moreover, since it occurs at a temperature much higher than that of the rotation ordering of Ho moments [7], thus, the two are probably irrelevant to each other.

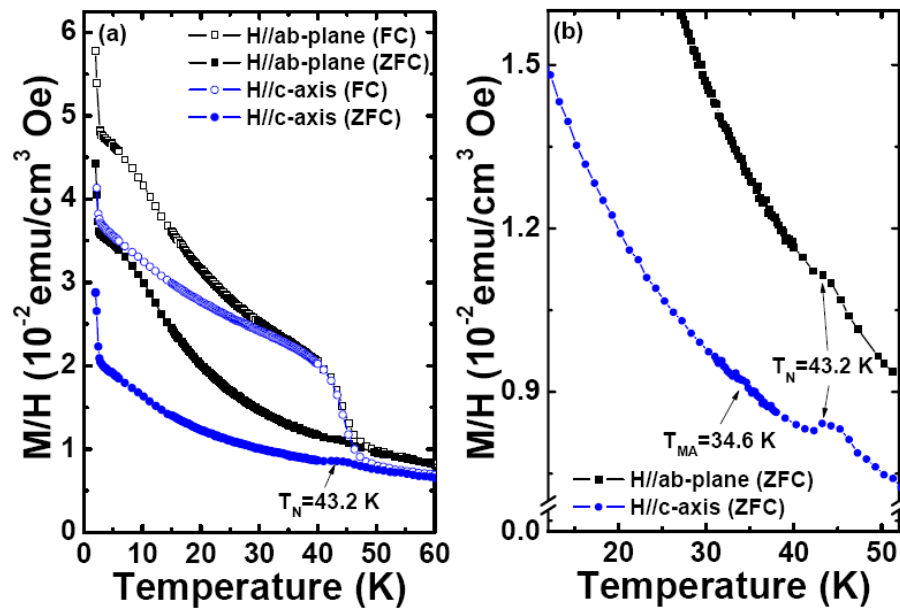


Figure 4.5 The temperature dependent magnetization ($M(T)$) of the o -HMO probed along the c -axis and the ab -plane. (a) The ZFC (solid symbols) and FC (open symbols) $M(T)$'s measured with a magnetic field of 100 Oe applying along the c -axis and in the ab -plane. Both reveal an AFM transition temperature of 43.2 K. (b) The enlarged version of the ZFC curves displayed in (a). A magnetic ordering near 34.6 K is evident in the c -axis.

In order to seek for a reasonable origin, we note that, in addition to being markedly higher than T_L (~ 26 - 29.6 K), T_{MA} (~ 35 K) also appears to be quite sensitive to the film microstructures and/or strain states. To illustrate the latter point, we obtained the respective lattice constants for the present c -axis film and the b -axis films grown on LAO [22] by using the four-circle XRD. The measured lattice constant for a , b , and c were 5.25 (5.28), 5.76 (5.80), and 7.47 (7.51) Å for the c -axis (b -axis) o -HMO films, respectively. Compared to $a = 5.26$, $b = 5.84$, and $c = 7.36$ Å for the bulk o -HMO [14], the b - and c -axis of the films are apparently under compressive and tensile stresses, respectively. It has been proposed [26] that, in the hexagonal phase of HMO, canting of the Mn^{3+} spins out of the basal xy plane can drastically reduce the magnetic symmetry and hence induce magnetoelectric effect. Thus, in order to check whether or not the current c -axis ordering anomaly is resulting from the similar canting effects, we measured the M - H curves at several temperatures below and above the c -axis ordering temperature. As is evident from the results displayed in Fig. 4.6, the M - H curve becomes clearly hysteretic when $T < T_N$ (~ 43 K), indicating a weak ferromagnetism emerges immediately after the system gets into the AFM state. This is also consistent with the magnetization enhancement occurring at T_N as described in the previous paragraph. However, the $M(H)$ loop appears to shrink with decreasing temperature and then remains essentially constant after $T < 30$ K (see Fig. 4.6 and its inset). This indicates that the weak ferromagnetism below T_N might have arisen from the imbalance in the number of “up” and “down” spins [27], instead of the similar canting effects observed in hexagonal HMO [26]. In the latter, the magnetic moment is not expected to decrease with temperature. Since, there exists significant lattice mismatch-induced epitaxial strain in our films which might interrupt the formation of long-range AFM order. The short-range ordering nature of the AFM domains inherent in these frustrated manganites, in turn, gives rise to significant incomplete spin compensation and the sharp magnetization enhancement below T_N . On the other hand, the slight shrinkage of $M(H)$ loop towards $T_{MA} \sim 35$ K may be attributed to the incommensurate AFM to commensurate AFM transition, which, though has been drastically affected by the lattice distortion, could cause some rearrangement of the uncompensated spins.

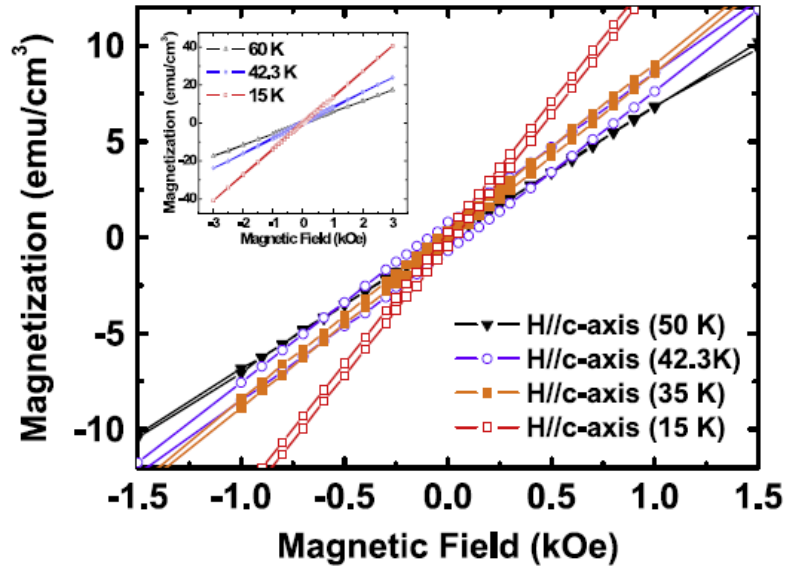


Figure 4.6 The field-dependent magnetization (M - H) measured at four temperatures. The hysteretic behavior exhibited when $T < T_N$ indicates the presence of weak ferromagnetism. The inset shows the results in larger scale.

The other important question to be addressed is: Does any of these magnetic ordering actually lead to the gigantic polarization as expected? Figure 4.7 shows the temperature and magnetic field dependences of the dielectric constant directly measured along the c -axis with the external magnetic field applied parallel to the surface ($\mathbf{H} // ab$ -plane) of the film. It is clear that, when lowering across the AFM temperature (~ 42 K) there is no sign of ferroelectric transition occurring along the measuring c -axis. As the temperature is lowered across T_{MA} (~ 35 K) the relative dielectric constant starts to increase slowly, but no abrupt change is evident. However, with further lowering of temperature, the dielectric constant grows rapidly when $T < 20$ K and reaches maximum around $T = 13.5$ K and appears to be non-hysteretic in temperature (see inset of Fig. 4.7) [28]. Moreover, the enhancement of dielectric constant is drastically reduced with a downshift of the maximum temperature when an external magnetic field was applied. It is noted that similar behaviors have been observed in polycrystalline o -HMO previously and was attributed to transition of Ho moment from b -axis collinear to a noncollinear alignment below 15 K [7, 9]. However, in that the noncollinear structure was expected to give rise to a FE displacement along the a -axis (in $Pbnm$ group symmetry) instead of along c -axis observed here. Moreover, the effect of the applied external field in suppressing the dielectric constant enhancement

observed in the present case apparently is much more drastic than those reported in ref. [9]. The present results, thus, imply that, albeit the strong magnetic effect on the dielectric enhancement (Fig. 4.7), the interplay between the magnetic ordering and the induced FE might be more subtle than previously conceived, in particular when external stress is also coming into play.

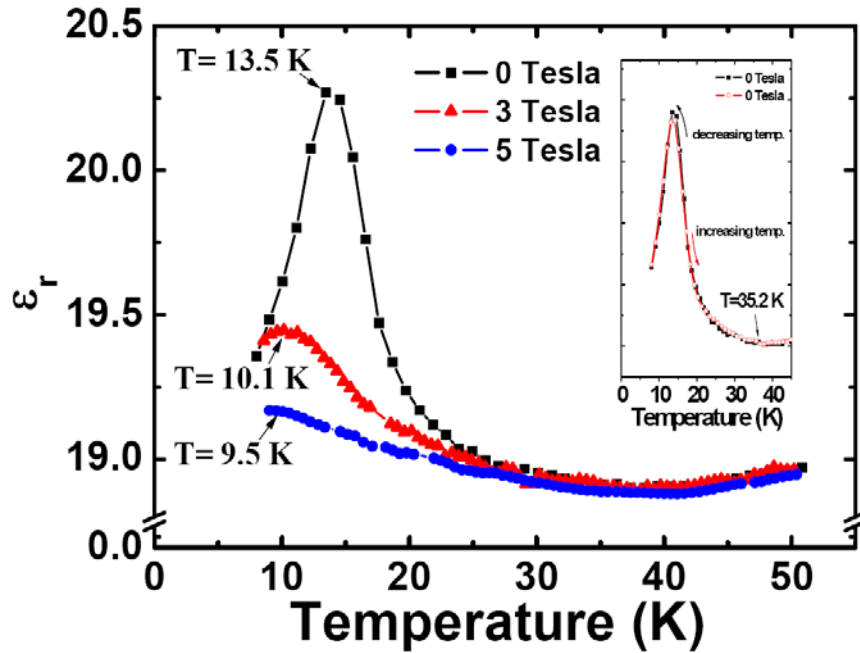


Figure 4.7 The dielectric constant as a function of temperature measured along the c -axis of the o -HMO film. Significant suppression of the enhancement and peak temperature by the applied field are evident. The inset shows that the dielectric enhancement is non-hysteretic in temperature.

Since the current results suggest that T_{MA} is probably the manifestation of the reordering of Mn^{3+} spins due to the compressed b -axis, it is natural to ask: Is the 30-35 K magnetic ordering along the c -axis relevant to the so-called “lock-in” temperature (T_L)? And what role it plays in the magnetic ferroelectricity? Very recently, the microscopic origin of the FE order in E -type orthorhombic HMO has been proposed to be simultaneously originated from two mechanisms: lattice and electronic [13]. For the electronic origin, the magnetic ordering induces hybridization of electronic orbitals, which, in turn, leads to a polar charge distribution [29, 30]. On the other hand, the AFM coupled FM zigzag spin chains within the ab -plane of the o -HMO can lead to buckling distortion of the oxygen octahedral allowing for the formation of a polar displacement along the a -axis [6]. In both

microscopic mechanisms, neither the magnetic ordering nor the induced polarization was expected to take place along the c -axis of o -HMO (in $Pbnm$ space group). Thus, if the 35 K c -axis ordering is relevant, it could be somehow acting as a trigger of the subsequent lock-in ordering transition at a slightly lower temperature. Unfortunately, the availability of either b -axis or a -axis oriented o -HMO films has been limited to non-conductive substrates. Thus, direct measurements of polarization along the other two principal axes are not accessible at present. Finally, we would like to point out that there was no further magnetic ordering transition, except for the AFM ordering near 43 K, observed along either the a - or b -axis, as is evident from Fig. 4.5 or in ref. [22]. The reason might be because that the “lock-in” transition involves mainly the commensuration between the periodicity of magnetic ordering structure and that of the underlying lattice and there is no significant change in the total moments to be resolved in magnetization measurements.

4.2.3 Summary

In summary, we have grown the c -axis oriented orthorhombic HoMnO_3 thin films on conductive Nb-doped $\text{SrTiO}_3(001)$ substrates, which allowed us to perform the direct measurement of orientation-specific magnetic ordering induced ferroelectricity in this material. Surprisingly, the films exhibit an anomalous magnetic ordering around 35 K as well as an abrupt dielectric enhancement starting around 20 K and reaching maximum around 13 K along the c -axis. In addition, the dielectric enhancement and its peak temperature was markedly suppressed when an external magnetic field (in Tesla range) was applied in the ab -plane. We argue that, although the existence of the weak second magnetic ordering, the induced ferroelectricity, and magnetoelectric coupling along the c -axis of the orthorhombic HoMnO_3 are not compatible with most of the available theoretical models proposed, it is evidently demonstrated to be closely related to the strain-induced effect on the ordering of Mn^{3+} moments. Nevertheless, further investigations are certainly needed to delineate how it couples to Ho^{3+} moments to give rise to the dielectric enhancement at lower temperatures.

4.3 Magnetism-induced ferroelectric polarization in the *c*-axis-oriented orthorhombic HoMnO₃ thin films

In this section, the magnetism-induced ferroelectricity in the *E*-type orthorhombic HoMnO₃ (*o*-HMO) films grown on Nb-doped and undoped SrTiO₃(001) substrates were studied. The temperature dependent magnetization in these films evidently exhibits an antiferromagnetic ordering around 44 K and an anomalous second magnetic ordering along the *c*-axis near 35 K. Interestingly, at this anomalous transition temperature, an associated ferroelectric polarization was probed by the *P-E* hysteresis measurements, indicating the intimate coupling between the ferroelectric response and the reordering of Mn spins, which has never been disclosed previously by dielectric constant measurements.

4.3.1 Introduction

Magnetoelectric materials exhibiting symmetry-breaking magnetic transformation-induced improper ferroelectricity have attracted much interest due to the intriguing fundamental physics involved and their promising multifunctional application potential for next generation electronics [1-5]. Among the known multiferroic materials, the rare-earth perovskite manganites $RMnO_3$ ($R=Y, Ho, Er$ and Yb) have drawn enormous attention recently [7-8, 31]. In particular, Picozzi *et al.* [13] have theoretically proposed that the quantum-mechanical effects of electron orbital polarization manifested in the orthorhombic HoMnO₃ (*o*-HMO) with *E*-type magnetic structure might result in polarization orders of magnitude larger than those exhibited in helical magnetic ordering-induced ferroelectricity. Unfortunately, under ambient conditions, the stable structure of $RMnO_3$ compounds with smaller *R* ions (i.e., $R=Ho-Lu$) is hexagonal, thus the metastable bulk orthorhombic phase can only be prepared by means of high-temperature high-pressure synthesis [7-9, 32] or the citrate-based soft chemistry method [11-12]. For these samples, the neutron scattering [12] showed that *o*-HMO indeed exhibited an incommensurate (ICM) antiferromagnetic (*AF*) transition around 42 K and at a somewhat lower temperature (~26-29.6 K) the magnetic order locks into a temperature-independent commensurate (CM) wave vector as expected. However, pyroelectric current measurements

on bulk polycrystalline *o*-HMO revealed only a minute ferroelectric polarization ($P \approx 90 \mu\text{C}/\text{m}^2$). Furthermore, the results also demonstrated a strong dependence of polarization on the applied magnetic field below the ordering temperature of the Ho, suggesting the possible involvement of Ho moments in the development P [7, 9]. The discrepancies were ascribed to the unavailability of single crystalline samples. Thus, in order to clarify some of the outstanding issues and gain more insight toward understanding the intriguing correlations between the spin, charge, and lattice degree of freedoms, it is essential to obtain samples capable of revealing the relevant physical properties along the distinctive crystallographic orientations. As a result, alternative ways of preparing orientation-specific orthorhombic RMnO_3 thin films have received extensive attention lately [18, 22, 31-35].

Very recently, in consistent with those reported on bulk *o*-HMO samples [7,9], we have observed a distinct peak in the temperature dependence of the dielectric constant in the *c*-axis oriented *o*-HMO films at temperatures near the spin-reorientation transition of Ho [33]. Similar observations were reported subsequently in the *a*-axis oriented *o*-HMO films [35]. These results, instead of confirming the unprecedented Mn-moments ordering-induced ferroelectricity expected by several theoretical proposals [13, 36], have indicated otherwise and suggested the ordering of Ho-moments might be more relevant [7, 9, 33, 35]. The apparent discrepancies are puzzling and required further clarifications. In this study, we performed polarization measurements on the *c*-axis-oriented *o*-HMO films grown on Nb-doped SrTiO_3 (Nb-STO) substrates by pulse laser deposition (PLD). We observed a clear ferroelectric polarization intimately associated with a weak anomalous magnetic transition occurring in the *c*-axis magnetization. This is in sharp contrast to that displayed in dielectric constant measurements. In particular, it appears that the compressive epitaxial strain along the *b*-axis of the *o*-HMO films might have prominent influences on the ICM to CM magnetic structure transition, which might have eventually led to an unexpected magnetoelectric polarization along the *c*-axis of this system.

4.3.2 Results and Discussion

Fig. 4.8(a) shows the θ - 2θ XRD patterns for the as-deposited *o*-HMO films on STO(001) substrates. Only the diffraction peaks corresponding to (00 l) family of planes of *o*-HMO are observed, indicating the formation of a pure *o*-HMO with the *c*-axis (space group: *Pbnm*) oriented normal to the film surface. The inset of Fig. 4.8(a) shows that a full width at half maximum in the rocking curve of the (004) peak is about 0.72° , indicating a reasonably good crystalline quality. To further investigate the in-plane texture of the films, we measured the ϕ -scan around the *o*-HMO (202) reflection to confirm the epitaxial growth of the films. As shown in Fig. 4.8(b), a primary four-fold symmetry is observed, indicating that the films were indeed epitaxial and well-aligned with the substrate. The additional small peaks appearing in between the primary peaks are presumably due to lattice planes with diffraction angles very close that of the *o*-HMO(202) planes, as has been pointed out previously in *o*-YMnO₃ films [34]. From the XRD, we obtained the lattice parameters for the present *o*-HMO/STO(001) film to be $a = 5.251 \text{ \AA}$, $b = 5.767 \text{ \AA}$, and $c = 7.464 \text{ \AA}$, respectively. Compare to $a = 5.257 \text{ \AA}$, $b = 5.835 \text{ \AA}$, and $c = 7.361 \text{ \AA}$ for the bulk *o*-HMO, it is clear that the film is nearly relaxed along the *a*-axis but is significantly strained along the *b* and *c* directions, even at a thickness of 180 nm. The values of the lattice parameters are essentially the same as that reported in Ref. 16 and are consistent with the assertions made by Rubi *et al.* [37]. The inset of Fig. 4.8(b) shows the AFM image of surface morphology of the *o*-HMO film. It appears to consist of uniform, but slightly elongated, spherical shaped grains with an average grain size of about 45 nm and a root-mean-square surface roughness of 3.2 nm. The fact that no micro-cracks, voids or pinholes were observed suggests that the rather significant strain accompanying film growth must have been quite uniform.

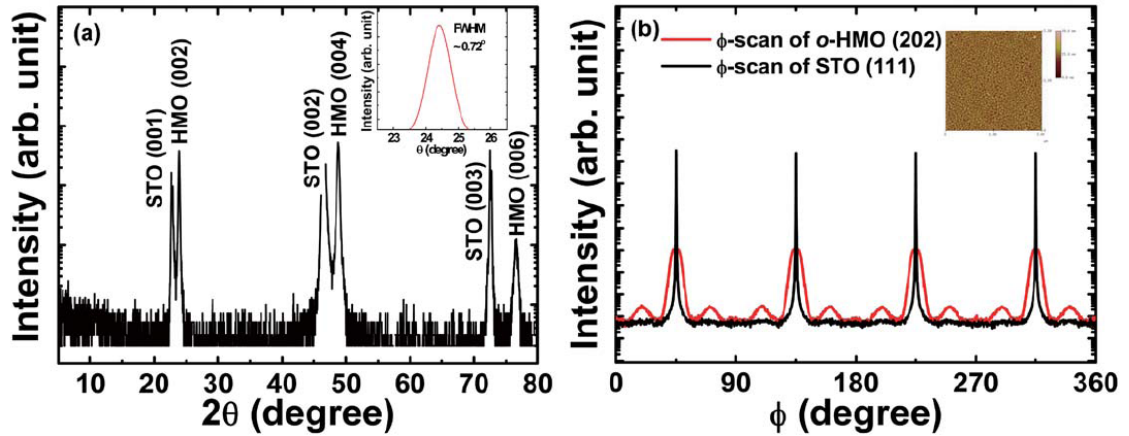


Figure 4.8 The XRD diffraction patterns of the *o*-HMO thin films grown on STO(001) substrates. (a) The typical θ - 2θ scans (intensity plotted in logarithmic scale) reveal that HMO films are indeed orthorhombic with nearly perfect *c*-axis oriented characteristic. The inset in (a) shows the rocking curve of the *o*-HMO (004) peak. (b) The azimuthal ϕ -scans (intensity plotted on a logarithmic scale) of the (202) peak of the *o*-HMO films, displaying the nearly ideal alignment of crystallographic orientations between film and substrate. The inset of (b) is a $2 \times 2 \mu\text{m}^2$ AFM topographic image of a 180 nm-thick *o*-HMO film deposited on STO(001) substrate.

Previously, it has been suggested that epitaxial strain existing in substrate-stabilized orthorhombic YMnO_3 (*o*-YMO) films may modify the magnetic structure, and hence the accompanying induced magnetoelectric effect [18, 34]. We suspect that similar effects might be also prevailing in the current *o*-HMO films. Fig. 4.9(a) shows the typical temperature dependent magnetization ($M(T)$) curves probed by the zero-field-cooled (ZFC) scheme with an external field of 100 Oe applied either in the *ab*-plane or along *c*-axis of the *o*-HMO films. As is evident in Fig. 4.9(a), both of the two ZFC $M(T)$ curves clearly exhibit an ordering transition near 44 K (see also the FC and ZFC results with an applied magnetic field of 500 Oe along the *c*-axis shown in the inset of Fig. 4.9(a)), which is in agreement with previous reports [11, 12, 18, 32, 34-35] and can be attributed to the usual *AF* ordering of Mn moment for *o*-HMO. Another feature to be noted from the $M(T)$ curves displayed in Fig. 4.9(a) is the significantly larger magnetization level along the *ab*-plane than that in the *c*-axis direction over the entire temperature range. According to the neutron diffraction results [12], the magnetic ordering of the Mn^{3+} ions is uniaxial and the moments are parallel to the *b* direction, making *b*-axis the easy axis. At lower temperatures, where the magnetic moment of Ho^{3+} eventually comes into play below $T = 20\sim 25$ K, which has been found to

order in the (110) planes [12]. Both facts, thus, might explain the more favorable magnetization when probed in the ab -plane. On the other hand, the dramatic increase in the magnetization around $T = 2$ K has been suggested to result from the metamagnetic transition of Ho^{3+} ions [12]. Finally, we note that around 35 K there exists a small but noticeable anomaly in the c -axis $M(T)$ curve signifying a possible magnetic transition which is undetectable when the field is applied in the ab -plane (Fig. 4.9(a)). To better visualize this small anomaly, two c -axis $M(T)$ curves obtained by applying different magnetic fields are compared in Fig. 4.9(b). As is evident from the results that, when the applied field strength was increased from 100 Oe to 500 Oe, the weak anomalous magnetic transition has slightly changed from 34.2 K to 33.6 K (see also the 500 Oe ZFC results for HMO/Nb-STO film shown in the lower-left inset of Fig. 4.9(b)), while the AF ordering remains essentially unchanged around 44 K. In fact, for the general results reported here, both films can be regarded as identical in magnetic properties. These present data confirm again a lock-in-like magnetic ordering occurring around 35 K as previously delineated in a c -axis oriented o -HMO film [33]. We note that the neutron diffraction results reported by Brinks *et al.* (left inset of Fig. 5 in Ref. 11) also indicate a similar secondary magnetic ordering near 30 K along [001] of o -HMO. Perhaps, the most significant implication of the present results is that the Mn atoms with antiparallel spins along the b -direction might have been drastically affected by lattice distortion, which has eventually led to an unexpected second magnetic ordering with higher temperature along the c -axis of o -HMO.

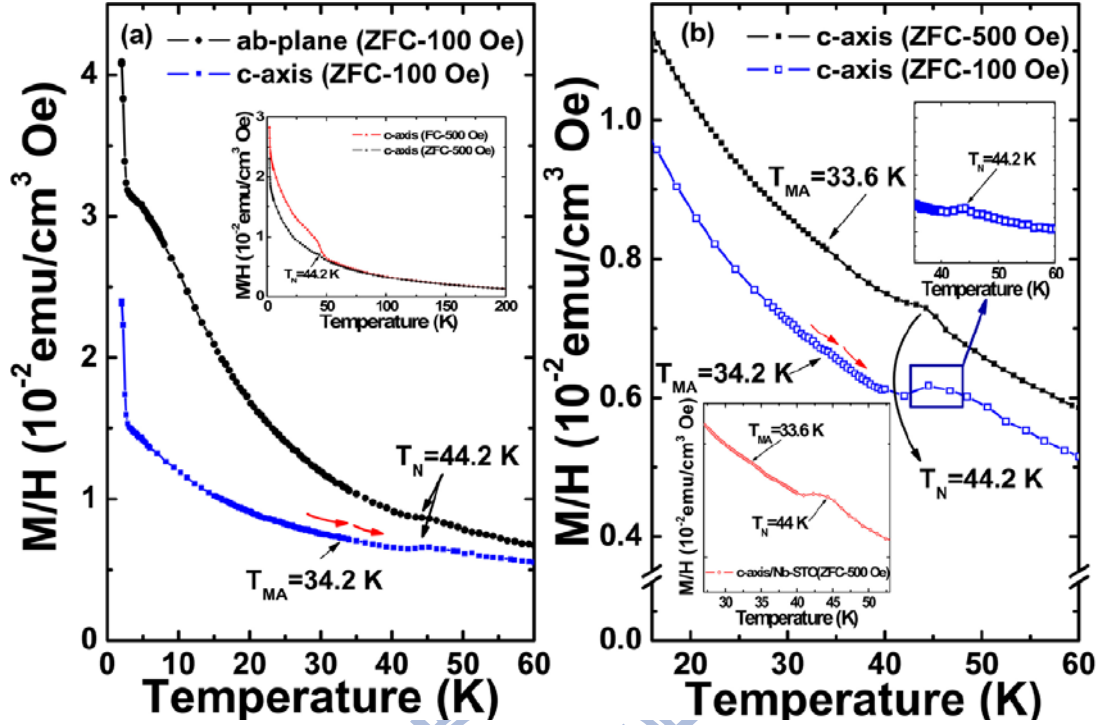


Figure 4.9 (a) The zero-field-cooled temperature-dependent magnetizations (ZFC- $M(T)$) for *o*-HMO film probed along the *c*-axis and the *ab*-plane with an applied magnetic field of 100 Oe. Both reveal an AF transition temperature of 44.2 K. The inset in (a) shows the FC- and ZFC- $M(T)$ over the whole temperature range measured along the *c*-axis at 500 Oe. (b) The ZFC- $M(T)$ along the *c*-axis measured at 100 Oe and 500 Oe. (For the sake of clarity the 500 Oe curve is slightly shifted.) The 0.2 K difference seen in T_N for the 100 Oe and 500 Oe results is mainly due to different measuring temperature intervals used during measurements. As shown in the upper-right inset, when we change the temperature interval from 2 K to 1 K and re-measure part of the 100 Oe curve (indicated by the square frame), it evidently displays exactly the same T_N as seen on the 500 Oe curve measured with the same temperature interval. The lower-left inset shows that the similar feature also occurs for *o*-HMO/Nb-STO film with a magnetic field of 500 Oe.

The other important question to be asked here is: Does this weak second magnetic transition along the *c*-axis around 35 K have anything to do with ferroelectric polarization? Here, we report an attempt to address this issue by using the conductive Nb-doped SrTiO₃(001) substrates for preparing the epitaxial *o*-HMO thin films [33]. To further clarify the coupling between the electric and magnetic ordering, measurements of polarization versus electric field (P - E) hysteresis loops with E parallel to *c*-axis were carried out at cryogenic temperatures using a closed cycle refrigerator system ($T_{\text{lowest}} = 13$ K). Fig. 4.10

shows the P - E hysteresis loops measured at several temperatures below and above the c -axis ordering temperature with a field value of $E_{\max} = 10$ kV/cm at $f = 1$ kHz. The results indicate that a weak ferroelectric behavior starts to emerge below 40 K and which appears to grow with decreasing temperature. In particular, we note that near the magnetic anomaly temperature ($T_{MA} \sim 35.1$ K), the P - E loop appears to exhibit some kind of “training effect”, that is the area of the loop grows with cycles of measurement (not shown). Nevertheless, the loop size ceases to grow and remains essentially constant as those obtained at lower temperatures (see the 20 K and 13 K curves in Fig. 4.10). Moreover, in these preliminary measurements, all of the P - E hysteresis loops show lack of the typical saturating behaviors for ferroelectricity, indicating that there might be significantly contributions from the leakage current at higher fields [38]. Since the resistivity of the films is about 10^{10} Ω -cm [39], the leakage current in the present measurement configuration could be believed to arise primarily from the contact property asymmetry-induced polarization dependent leakage [38], instead of from the films.

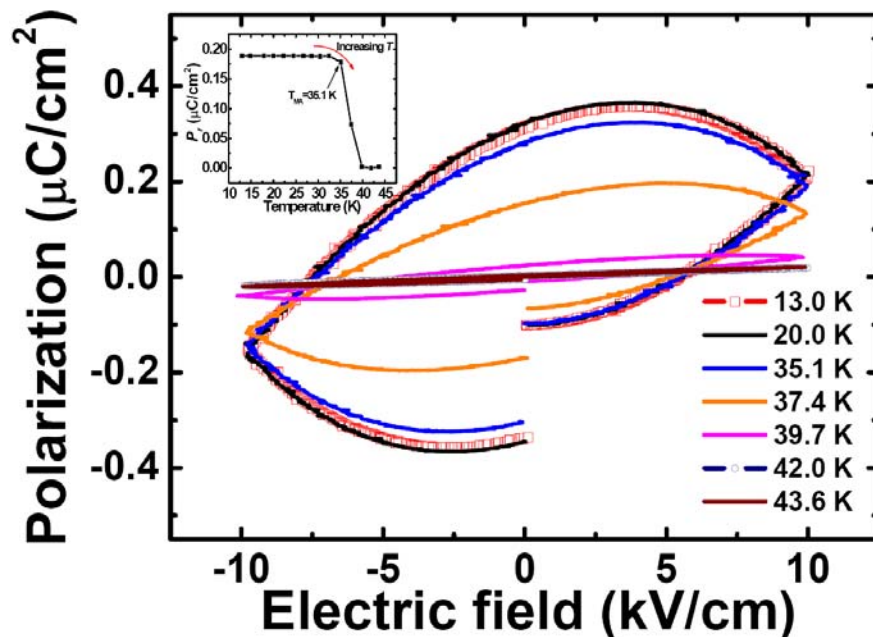


Figure 4.10 P - E hysteresis loops of the o -HMO thin film grown on Nb-doped $\text{SrTiO}_3(001)$ substrates measured at various temperatures. The inset shows the remnant polarization obtained by pulsed polarization measurement at various temperatures.

In order to reduce the effects of the leakage [40] and to delineate the close relation between T_{MA} and the measured c -axis polarization, we show, in the inset of Fig. 4.10, the temperature variation of switching polarization ($\Delta P=2P_r$). Here P_r is the remnant polarization obtained by pulsed polarization measurement [41]. The results again indicate that the primary ferroelectric transition is taking place around 35 K, which corresponds intimately to T_{MA} seen in Fig. 4.9(b). It strongly suggests that the steep rise in the polarization at lower temperatures is most likely due to the reordering of Mn spins. Furthermore, another important consequence of the P - E hysteresis loops is that the switched polarization is not significantly influenced by the magnetic moment of Ho^{3+} even at 13 K. It is also interesting to note that the magnetic transition-induced polarization probed by the P - E hysteresis measurements appears not to correlate with the $\varepsilon(T)$ results obtained from the polycrystalline o -HMO bulk samples [9] and epitaxial films [33, 35]. According to the recent theoretical calculations by Picozzi [13] and co-workers [36], the primary origin of polarization in o -HMO is more relevant to the asymmetric electron hopping of orbitally polarized e_g states of Mn^{3+} ions, which is intimately relating to the in-plane zigzag spin arrangement in the AF - E configuration, rather than resulting from the ionic displacement typical for “standard” dielectrics. The abovementioned deviations between the polarization and dielectric measurements, thus, might result from similar origin. Finally, we would like to point out the current results have beyond any doubt revealed a sizeable ferroelectric ordering closely related to an anomalous magnetic transition occurring along the c -axis, which are at variance with what have been expected for the AF - E -type o -HMO perovskites. We believe that the significant strain introduced to stabilize the growth of the desired phase is playing a crucial role. On the other hand, the present results also imply a possible route to engineer these materials for harvesting the intriguing emergent properties in these AF - E -type perovskites.

4.3.3 Summary

In summary, we have performed polarization measurements on the c -axis oriented o -HMO thin films grown on Nb-doped SrTiO₃ substrates. It is found that the compressive epitaxial strain along the b -axis of the o -HMO films might have prominent influences on the transition to a commensurate magnetic structure, which has eventually led to an unexpected second magnetic ordering along the c -axis near 35 K. Interestingly, a ferroelectric (FE) polarization probed from the P - E hysteresis measurements was also evidently observed at this anomalous temperature, indicating the intimate coupling between the FE response and the reordering of Mn spins in o -HMO. Since it was not observed in the dielectric constant measurements performed on polycrystalline and similar thin film o -HMO samples, it is suggestive that the primary origin of polarization in o -HMO is more relevant to the asymmetric hopping of e_g -orbital electrons of Mn³⁺ ions rather than resulting from the ionic displacement typical for “standard” dielectrics.



4.4 Magnetic and electric properties of the a -axis-oriented orthorhombic HoMnO_3 thin films

In this section, we have successfully prepared the a -axis-oriented orthorhombic HoMnO_3 (o -HMO) thin films by pulsed laser deposition on Nb-doped $\text{SrTiO}_3(110)$ single crystal substrates. The near perfectly aligned film growth orientation with the substrate allows us to study the magnetic transitions along the respective crystal orientation. The marked anisotropic behaviour of magnetic ordering probed along different crystallographic orientations appears to intimately relate to the respective ordering of moments arising from Mn and Ho ions.

4.4.1 Introduction

Multiferroics are scarce materials that can provide two or more switchable states, *i.e.* polarization, magnetization, and strain [42] and be interdependent between the corresponding ordered phases. Among various multiferroic materials, the orthorhombic phase rare-earth manganites (RMnO_3 with $R = \text{Ho, Er, Tm, Yb, and Lu}$) are expected to exhibit an incommensurate antiferromagnetism (IC- AFM) to E -type AFM transition with an induced ferroelectric polarization to accompany the magnetic transition [6, 13, 36, 43]. However, direct demonstration of these fascinating phenomena has been hindered by the challenges in obtaining samples with the desired phase and, especially with definite crystallographic orientations, namely single crystals. Indeed, previous measurements performed on bulk polycrystalline orthorhombic HoMnO_3 (o -HMO) revealed only a minute ferroelectric polarization ($P \approx 90 \mu\text{C}/\text{m}^2$) with evidences suggesting the possible involvement of Ho moments in the development of P [7, 9].

In trying to clarify some of these seemingly disputable issues, we have recently succeeded in preparing orientation-specified o -HMO thin films on various substrates [22, 33, 44]. These films, in addition to exhibiting the IC- AFM transition with $T_N \sim 42 \text{ K}$ and expected magnetoelectric effects, have displayed distinctive magnetic transition anisotropies at lower temperatures, which are believed to arise from the strain-induced effect on the IC- AFM to commensurate E -phase AFM transition. However, owing to the overwhelming paramagnetic background from the Ho moments, the conclusions drawn

from the temperature dependent magnetic susceptibility, $\chi(T)$, need further experimental supports. Moreover, as pointed out by Muñoz *et al.* [12], the smaller size of the rare-earth ion radius may also affect the magnetic ground states of $RMnO_3$ (i.e. $R= Y, Ho, Er$ etc.) manganites due to the tilting of the MnO_6 octahedra and presence of the Jahn-Teller distortion.

Recently, it has also been suggested that epitaxial strain existing in substrate-stabilized orthorhombic $YMnO_3$ (*o*-YMO) films may modify the magnetic structure, and hence the accompanying induced magnetoelectric effect [34, 45]. In previous reports [22, 33, 35, 44], the *o*-HMO films were fabricated with either *a*-, *b*- or *c*-axis perpendicular to the film surface. However, the analysis of the impact of the lattice distortion on the magnetic properties of these orientation-specified *o*-HMO thin films remains to be unraveled. Another open question of current interest is how the introduction of the epitaxial strains would affect the magnetic lock-in transition temperature of the *o*-HMO system. On the other hand, it is also interesting to investigate the role of Ho moments, when coupled with the lattice strain, in shaping the eventual magnetic structure and the associated magnetoelectric effect in these multiferroic perovskite manganites.

In this paper, we have investigated the characteristics of the HMO films grown on 0.5 %-Nb:SrTiO₃(110) (Nb:STO(110)) substrates. The compressive in-plane stresses, resulting from the film/substrate epitaxial relations, have indeed led to marked anisotropic characteristics in magnetic transitions when probed by applying the field along various crystallographic orientations of these *a*-axis-oriented *o*-HMO films.

4.4.2 Results and Discussion

For rare-earth manganites with chemical composition $RMnO_3$, it is known that the crystal structure of $RMnO_3$ transforms from orthorhombic to hexagonal as the ionic size of the rare-earth elements gradually decreases from Nd to Ho. Unfortunately, $HoMnO_3$ is located near boundary between hexagonal and orthorhombic structure. Thus, in order to stabilize the phase and epitaxially grow *o*-HMO films with controllable orientations, it is crucial to select the suitable substrates. In this study, we chose the Nb:STO(110) substrates. The lattice constants along the $[1\bar{1}0]$ and $[001]$ directions of Nb:STO are 5.523 Å and 7.810

Å, respectively, thus are quite suitable to accommodate the bc -plane of o -HMO. Fig. 4.11(a) shows the results of the θ - 2θ scans for the o -HMO films grown on Nb:STO(110) substrates. As is evident in figure 4.11(a), the diffraction pattern reveals pure $(l00)$ peaks without discernible secondary phases, indicating that the films are perfectly epitaxial growth with a -axis perpendicular to the surface of substrates. The inset of Fig. 4.11(a) shows that a full width at half maximum in the rocking curve of the (200) peak is around 0.011° , indicating a reasonably good crystalline quality. Furthermore, as shown in Fig. 4.11(b), the ϕ -scans of the (110) and (020) reflections for the as-deposited o -HMO films and substrates exhibits a clear twofold symmetry, suggesting that the films were indeed of pure orthorhombic structure and well-aligned with the substrate. We note that the nearly perfect epitaxial relation between o -HMO(110) and Nb:STO (020) peaks shown in Fig. 4.11(b) is also consistent with the expected lattice mismatches of 5.75 % along the [001] direction and -5.66 % along the $[1\bar{1}0]$ direction for growing o -HMO on the Nb:STO(110) substrates. The lattice constants obtained here are $a = 5.277 \text{ \AA}$, $b = 5.752 \text{ \AA}$, and $c = 7.478 \text{ \AA}$, respectively. Compare to $a = 5.257 \text{ \AA}$, $b = 5.835 \text{ \AA}$, and $c = 7.361 \text{ \AA}$ for the bulk o -HMO, it is clear that the film is under tensile strain within the ac -plane and compressive strain along the b -axis, even when its thickness reaches 100 nm. The crystalline quality of the obtained o -HMO films thus allows us to directly probe the physical properties of the films along the three principal crystalline axes.

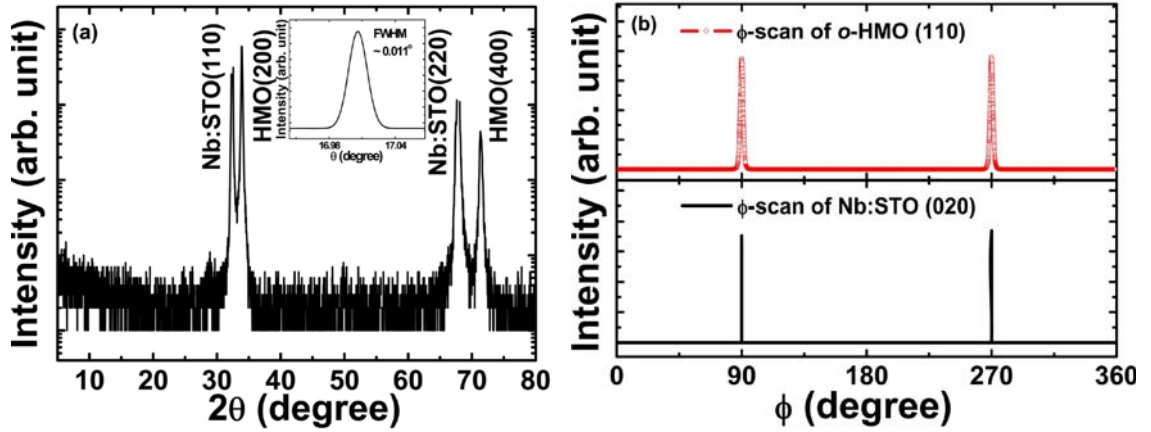


Figure 4.11 (a) The XRD θ - 2θ scan of the *o*-HMO thin film grown on Nb:STO(110) substrate, showing that the film is single-phase *a*-axis-oriented orthorhombic perovskite manganites (in *Pbnm* space group settings). The inset in (a) shows a rocking curve measured around the *o*-HMO (200) peak. (b) The ϕ -scans of the same film displayed in (a), showing the nearly perfect in-plane alignments between film and substrate.

When the IC-*AFM* to CM-collinear *E*-phase transition takes place [12], the commensurate magnetic wave vector will propagate along the *b*-direction with the magnetic moments of Mn ions configuring anti-parallel to each other. Consequently, one expects that some extrinsic effects might arise due to the *b*-axis compressive strain. With this in mind, we first made careful characterizations on the magnetic properties of these *a*-axis-oriented *o*-HMO films.

As shown in Fig. 4.12, the results of temperature dependent magnetization [$M(T)$] measured along the respective principal crystalline axis exhibit apparent anisotropic characteristics in terms of temperatures at which the magnetic structure transition occurs as well as the magnitude of susceptibility itself. We first note that, the expected Néel temperature at 44 K [12, 35] for the *AFM* transition can be clearly identified in each curve [see also the temperature derivative of magnetization, dM/dT , shown in the inset of Fig. 4.12]. Furthermore, we have pointed out that, for *o*-HMO films, the *b*-axis (in *pbnm* group symmetry setting) is the easy axis which explains the larger *b*-axis magnetization observed over the entire temperature range [22, 33, 44]. On the other hand, as is evident from the inset of Fig. 4.12, the weak lock-in-like magnetic transition ($T_{MA} \sim 35$ K) identified in the dM/dT of the *c*-axis was attributed to the compressive strain resulting from the epitaxial film growth [33, 44].

Finally, as can be seen in Fig. 4.12, we note that around 25 K there exists a broad but noticeable peak in the c -axis $M(T)$ curve signifying another possible magnetic ordering which is undetectable when the field is applied either in the a -axis or along the b -axis. To better comprehend this broad anomaly, the c -axis $dM(T)/dT$ curve probed by an applied magnetic field of 1000 Oe is obtained and displayed in the inset of Fig. 4.12. It is evident that, by increasing applied field strength from 100 Oe to 1000 Oe, the broad anomalous magnetic transition around 25 K remains essentially unchanged with the AFM ordering being kept around 44 K. According to the neutron diffraction results [12], at $T = 20\sim 25$ K, the magnetic moments of Ho^{3+} eventually come into play and appears ordered in the ab -plane. This observation explains the larger magnetization background along the b -axis over the entire temperature range probed. Moreover, perhaps the most significant implication of the present results is that the Ho atoms with parallel spins along the b -axis might have been drastically distorted by epitaxial strain, which has eventually led to a previously undisclosed magnetic ordering along the c -axis of o -HMO.

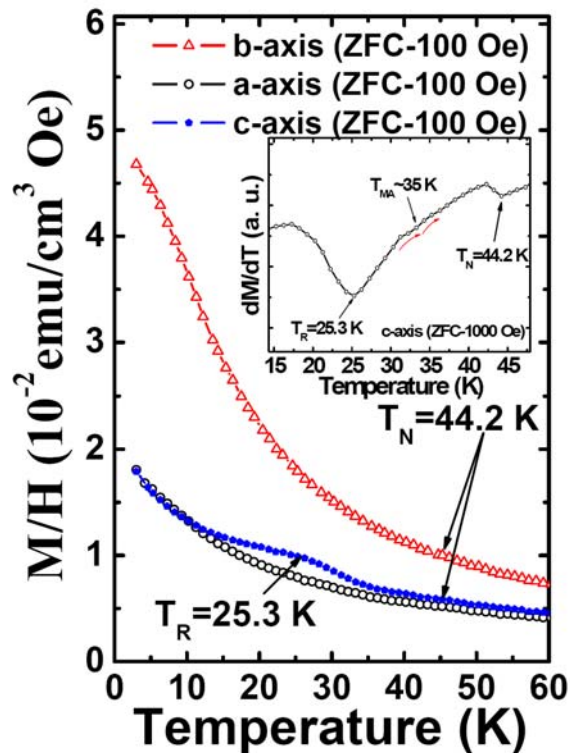


Figure 4.12 The zero-field-cooled (ZFC) $\chi(T)$ of the o -HMO films probed along the respective crystalline axis with an applied field of 100 Oe. The inset shows the temperature-dependence of first derivative of magnetization with respect to T measured with a 1000 Oe magnetic field along the c -axis.

In order to further check whether or not the current c -axis ordering anomaly is indeed a result of similar canting effects, it is essential to delineate the magnetic moment configuration of the rare-earth ions. Fig. 4.13 shows the magnetization as a function of applied magnetic field (M - H) hysteresis loops of the o -HMO films measured at several temperatures below and above where the c -axis ordering occurs. As is evident from the results displayed in Fig. 4.13, the M - H loop becomes clearly hysteretic when $T < 25$ K, indicating the occurrence of a weak ferromagnetism after the Ho^{3+} moments start to participate in the AFM state. This is also consistent with the magnetic anomalous transition occurring at $T \sim 25$ K when the magnetic moments of Ho atoms become ordered in the (110) planes. In this scenario, the observed second reordering ($T_{MA} \sim 35$ K) along the c -axis may be relevant to the IC-commensurate AFM transition [33, 44], which has not been drastically affected by the distortion-induced canting. Therefore, it is indicative that the canted AFM -induced ferromagnetism is in fact more pronounced when the system is in the commensurated AFM state. The current results further suggest that the lattice mismatch induced strain can strongly alter the magnetic properties of the as-grown o -HMO films.

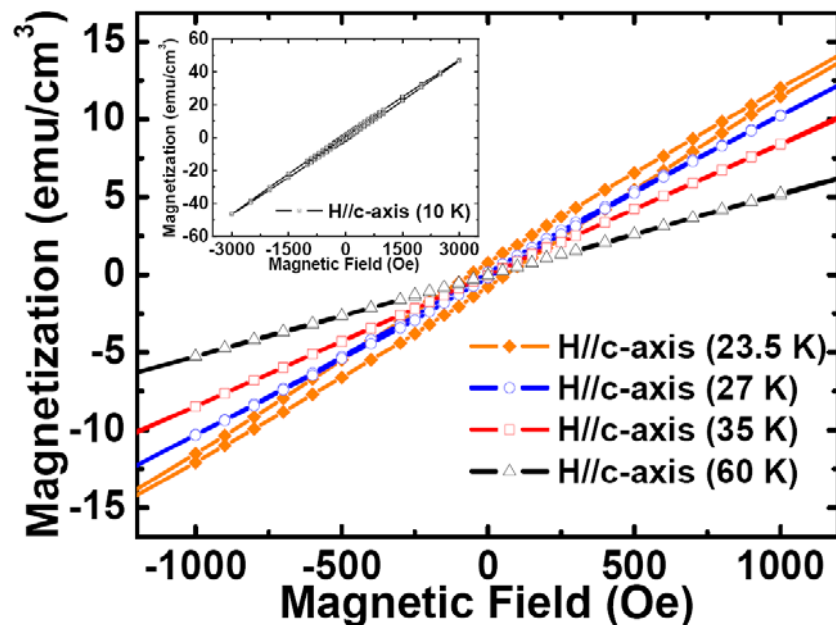


Figure 4.13 An enlarged vision of magnetic-field dependent magnetization (M - H) curves measured at 60, 35, 27, and 23.5 K. The inset shows a clear hysteretic behaviour displayed at 10 K indicating the presence of weak ferromagnetism.

Fig. 4.14 shows the temperature dependence of the dielectric constant directly measured along the a -axis by a gold pad as the top electrode and Nb:STO(110) substrate as the bottom electrode. It is clear that, when lowering across the AFM temperature (~ 44 K) there is no sign of ferroelectric transition occurring along the measuring a -axis. As the temperature is lowered across $T \sim 35$ K the relative permittivity starts to increase slowly, but no steep change is evident (see also the lower-left inset of Fig. 4.14(a)). Therefore, we associate the temperature of the gentle increase of $\epsilon_r(T)$ with T_{MA} and we suggest that the weak second magnetic transition along the c -axis near 35 K might be more relevant to the distinct anomaly in the dielectric constant. The behavior is similar to that found in the c -axis-oriented o -HMO thin films reported previously [33]. Moreover, with further lowering of temperature, we note that the dielectric constant reaches maximum around $T = 13.5$ K and appears to be non-hysteretic in temperature. In order to establish the correlation of the magnetic order and dielectric anomalies and, in particular, the ferroelectric hysteresis observed below T_{MA} , we have measured the polarization versus electric field (P - E) hysteresis loops with E parallel to a -axis between 13 and 40 K.

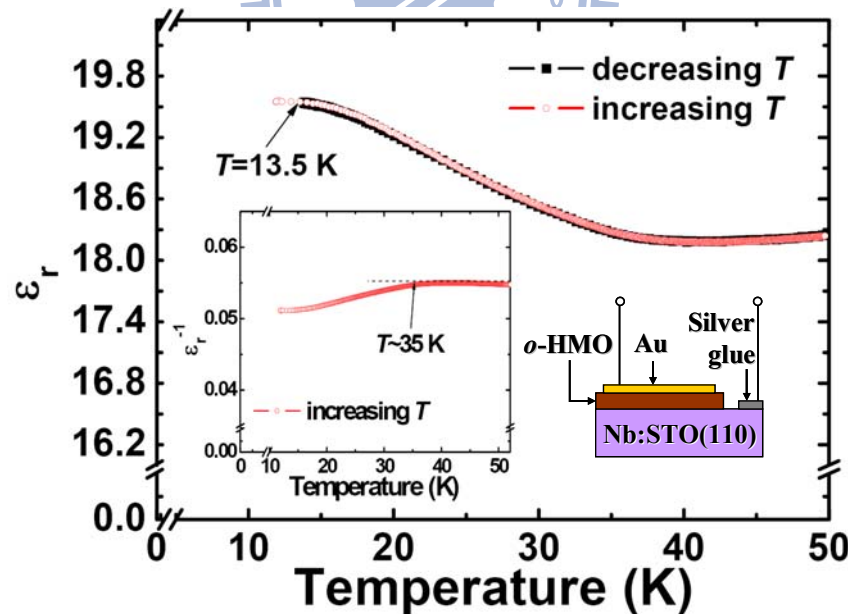


Figure 4.14 The dielectric constant (ϵ_r) as a function of temperature for o -HMO film evaluated from our measurements when cooling (closed symbols) and warming (open symbols) the sample. The left inset shows the temperature-dependent inverse relative permittivity. The right inset shows the schematic cross-section view of the survey.

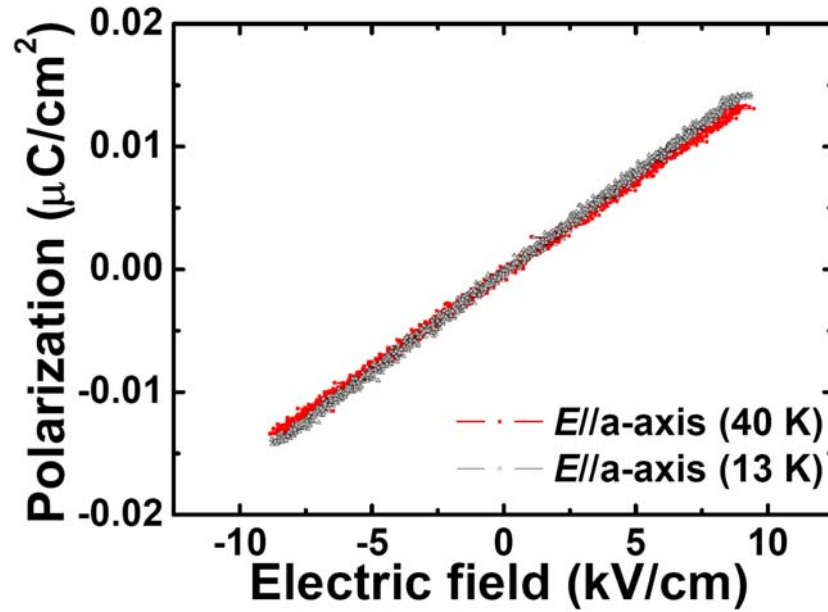
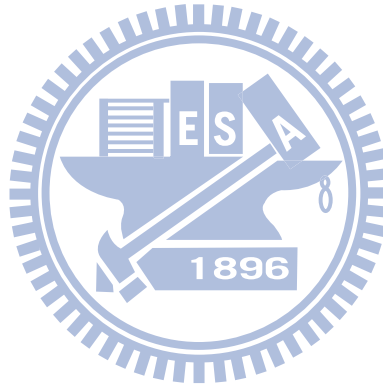


Figure 4.15 The electric-field dependent polarization (P - E) hysteresis loops for the o -HMO/Nb:STO(110) measured at 40, and 13 K.

P - E characteristics measured by applying a field value of $E_{\max} \sim 10$ kV/cm with a frequency of 1 kHz at different temperatures are shown in Fig. 4.15. It can be clearly seen from Fig. 4.15 that a quasi-linear ferroelectric behavior displays below Néel temperature and which appears to increase this slope of P - E curves with decreasing temperature (not shown). However, when lowering across the dielectric anomalous temperature ($T_{MA} \sim 35$ K), there is none-hysteretic behavior in loop shape as expected ferroelectricity along the measuring a -axis, even when its temperature reaches 13 K. Perhaps the difference between the experiment and theoretic prediction can be explained in terms of restricted strain effect from XRD results discussed above. In this scenario, our current results maybe suggest that the relative permittivity anomaly could be relevant to the consequence of the presence of the unanticipated spontaneous polarization along the c -axis. Although commensurated AFM -induced ferroelectricity in polycrystalline samples of the E -type phase had also been observed recently [46], these spontaneous polarization involved, however, were all less ten times than the presupposed value [6, 13, 36, 43]. On the contrary, maybe of greater relevance here is that the strain induced by substrate, and the resulting change of bond angles and distances, could modify some magnetic interactions, eventually altering the orientation of ferroelectricity to fit the available result [46].

4.4.3 Summary

In summary, we have successfully grown the orthorhombic *a*-axis-oriented HoMnO₃ films on the Nb-doped SrTiO₃(110) substrates. It is found that the behaviors of the orientation-dependent $M(T)$ curves are significantly different. In addition to the 44 K *AFM* ordering, a weak lock-in transition around 35 K was evidently observed with the field parallel to the *c*-axis. Furthermore, the epitaxial strain inherent in these strain-stabilized films appears to introduce significant effects to the magnetic transitions. Several unprecedented observations have been revealed in the present study. In particular, it is argued that, due to the epitaxial strain-induced distortion on the Ho moments aligning along the *b*-axis, a previously undisclosed magnetic ordering near 25 K along the *c*-axis of *o*-HMO is introduced.



References

- [1] T. Kimura, T. Goto, H. Shintani, K. Ishizaka, T. Arima, and Y. Tokura, *Nature (London)* **426**, 55 (2003).
- [2] N. Hur, S. Park, P. A. Sharma, J. S. Ahn, S. Guha, and S. -W. Cheong, *Nature (London)* **429**, 392 (2004).
- [3] W. Eerenstein, N. D. Mathur, and J. F. Scott, *Nature (London)* **442**, 759 (2006).
- [4] D. I. Khomskii, *J. Magn. Magn. Mater.* **306**, 1 (2006).
- [5] S.-W. Cheong and M. Mostovoy, *Nat. Mater.* **6**, 13 (2007).
- [6] I. A. Sergienko, C. Sen, and E. Dagotto, *Phys. Rev. Lett.* **97**, 227204 (2006).
- [7] B. Lorenz, Y. -Q. Wang, and C. W. Chu, *Phys. Rev. B* **76**, 104405 (2007).
- [8] F. Ye, B. Lorenz, Q. Huang, Y. Q. Wang, Y. Y. Sun, C. W. Chu, J. A. Fernandez-Baca, P. Dai, and H. A. Mook, *Phys. Rev. B* **76**, 060402(R) (2007).
- [9] B. Lorenz, Y. Q. Wang, Y. Y. Sun, and C. W. Chu, *Phys. Rev. B* **70**, 212412 (2004).
- [10] J.-S. Zhou and J. B. Goodenough, *Phys. Rev. Lett.* **96**, 247202 (2006).
- [11] H. W. Brinks, J. Rodríguez-Carvajal, H. Fjellvåg, A. Kjekshus, and B. C. Hauback, *Phys. Rev. B* **63**, 094411 (2001).
- [12] A. Muñoz, M. T. Casáis, J. A. Alonso, M. J. Martínez-Lope, J. L. Martínez, and M. T. Fernández-Díaz, *Inorg. Chem.* **40**, 1020 (2001).
- [13] S. Picozzi, K. Yamauchi, B. Sanyal, I. A. Sergienko, and E. Dagotto, *Phys. Rev. Lett.* **99**, 227201 (2007).
- [14] J. A. Alonso, M. J. Martínez-Lope, M. T. Casais, and M. T. Fernández-Díaz, *Inorg. Chem.* **39**, 917 (2000).
- [15] S. C. Chae, Y. J. Chang, S. S. A. Seo, T. W. Noh, D.-W. Kim, and C. U. Jung, *Appl. Phys. Lett.* **89**, 182512 (2006).
- [16] A. Muñoz, J. A. Alonso, M. T. Casais, M. J. Martínez-Lope, J. L. Martínez, and M. T. Fernández-Díaz, *J. Phys.: Condens. Matter* **14**, 3285 (2002).
- [17] T. Kimura, G. Lawes, T. Goto, Y. Tokura, and A. P. Ramirez, *Phys. Rev. B* **71**, 22425 (2005).
- [18] X. Martí, V. Skumryev, V. Laukhin, F. Sánchez, M.V. García-Cuenca, C. Ferrater, M. Varela, and J. Fontcuberta, *J. Mater. Res.* **22**, 2096 (2007).

- [19] M. Mostovoy, Phys. Rev. Lett. **96**, 067601 (2006).
- [20] T. Goto, T. Kimura, G. Lawes, A.P. Ramirez, and Y. Tokura, Phys. Rev. Lett. **92**, 257201 (2004).
- [21] O. Prokhnenko, R. Feyerherm, E. Dudzik, S. Landsgesell, N. Aliouane, L.C. Chapon, and D.N. Argyriou, Phys. Rev. Lett. **98**, 057206 (2007).
- [22] T. H. Lin, C. C. Hsieh, H. C. Shih, C. W. Luo, T. M. Uen, K. H. Wu, J. Y. Juang, J.-Y. Lin, C. H. Hsu, and S. J. Liu, Appl. Phys. Lett. **92**, 132503 (2008).
- [23] Steen Mørup, Daniel E Madsen, Cathrine Frandsen, Christian R H Bahl, and Mikkel F Hansen, J. Phys.: Condens. Matter **19**, 213202 (2007).
- [24] Airat Khasanov, Jian He, Jay Gaillard, Keqin Yang, Apparao M. Rao, C. Michelle Cameron, J. M. Schmeltzer, John G. Stevens, and Amar Nath, Appl. Phys. Lett. **93**, 013103 (2008).
- [25] S. Picozzi, K. Yamauchi, G. Bihlmayer, and S. Blügel, Phys. Rev. B **74**, 094402 (2006).
- [26] B. Lorenz, A.P. Litvinchuk, M.M. Gospodinov, and C.W. Chu, Phys. Rev. Lett. **92**, 087204 (2004).
- [27] L. Néel, C. R. Acad. Sci. Paris **252**, 4075 (1961).
- [28] Our preliminary electric field dependent polarization measurements performed on these films, though still suffered from leakage current problem, have clearly shown ferroelectric polarization emerging at $T \sim 36.2$ K (slightly higher than the ICM-CM transition temperature) and saturated for $T < 20$ K.
- [29] H. Katsura, N. Nagaosa, and A. V. Balatsky, Phys. Rev. Lett. **95**, 057205 (2005).
- [30] C. Jia, S. Onoda, N. Nagaosa, and J. H. Han, Phys. Rev. B **74**, 224444 (2006).
- [31] D. Rubi, Sriram Venkatesan, B. J. Kooi, J. Th. M. De Hosson, T. T. M. Palstra, and B. Noheda, Phys. Rev. B **78**, 020408(R) (2008).
- [32] M. Tachibana, T. Shimoyama, H. Kawaji, T. Atake, and E. Takayama-Muromachi, Phys. Rev. B **75**, 144425 (2007).
- [33] T. H. Lin, H. C. Shih, C. C. Hsieh, C. W. Luo, J.-Y. Lin, J. L. Her, H. D. Yang, C.-H. Hsu, K. H. Wu, T. M. Uen, and J. Y. Juang, J. Phys.: Condens. Matter **21**, 026013 (2009).
- [34] C. C. Hsieh, T. H. Lin, H. C. Shih, C.-H. Hsu, C. W. Luo, J.-Y. Lin, K. H. Wu, T. M. Uen, and J. Y. Juang, J. Appl. Phys. **104**, 103912 (2008).

- [35] T. C. Han, and J. G. Lin, Appl. Phys. Lett. **94**, 082502 (2009).
- [36] K. Yamauchi, F. Freimuth, S. Blügel, and S. Picozzi, Phys. Rev. B **78**, 014403 (2008).
- [37] D. Rubi, C. de Graaf, C. J. M. Daumont, D. Mannix, R. Broer, and B. Noheda, Phys. Rev. B **79**, 014416 (2009).
- [38] René Meyer, Rainer Waser, Klaus Prume, Torsten Schmitz and Stephan Tiedke, Appl. Phys. Lett. **86**, 142907 (2005).
- [39] The resistivity of the film increases from $10^9 \Omega\text{-cm}$ at room temperature to over $10^{10} \Omega\text{-cm}$ near 13 K.
- [40] M. A. Zurbuchen, T. Wu, S. Saha, J. Mitchell, and S. K. Streiffer, Appl. Phys. Lett. **87**, 232908 (2005).
- [41] Y. H. Chu, Q. Zhan, C.-H. Yang, M. P. Cruz, L. W. Martin, T. Zhao, P. Yu, R. Ramesh, P. T. Joseph, I. N. Lin, W. Tian, and D. G. Schlom, Appl. Phys. Lett. **92**, 102909 (2008); J. Li, H. Liang, B. Nagaraj, W. Cao, Chi H. Lee, and R. Ramesh, J. of Lightwave Technology **21**, 3282 (2003).
- [42] N. A. Spaldin, and M. Fiebig, Science **309**, 391 (2005).
- [43] C. Y. Ren, Phys. Rev. B **79**, 125113 (2009).
- [44] T. H. Lin, C. C. Hsieh, C. W. Luo, J.-Y. Lin, C. P. Sun, H. D. Yang, C.-H. Hsu, Y. H. Chu, K. H. Wu, T. M. Uen, and J. Y. Juang, J. Appl. Phys. **106**, 103923 (2009). =44
- [45] X. Marti, I. Fina, V. Skumryev, C. Ferrater, M. Varela, L. Fábrega, F. Sánchez, and J. Fontcuberta, Appl. Phys. Lett. **95**, 142903 (2009).
- [46] S. Ishiwata, Y. Kaneko, Y. Tokunaga, Y. Taguchi, T.-H. Arima, and Y. Tokura, Phys. Rev. B **81**, 100411(R) (2010).

Chapter 5

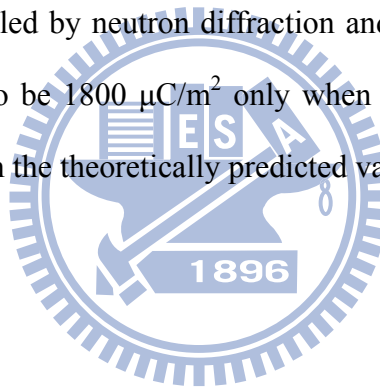
Summary and conclusions

We have prepared a series of well-textured (200)-, (020)- and (00 l)-oriented multiferroic orthorhombic HoMnO₃ (o -HMO) thin films, the intrinsically anisotropic physical property of the system unambiguously shows some salient features never being seen before. The prominent experimental observations and conclusions presented in this dissertation are summarized as follows.

1. o -HMO thin films with (200)-, (020)-, and (00 l)-orientations were successfully grown on Nb-doped SrTiO₃(110), LaAlO₃(110) and Nb-doped and undoped SrTiO₃(001) substrates by using pulsed laser deposition (PLD). The results demonstrate that the strain between film and substrate can serve as an alternative in transforming the thermodynamically stable hexagonal HoMnO₃ into the orthorhombic phase, which previously could only be obtained with high-pressure and high temperature syntheses.
2. The temperature dependent magnetization evidently displays an antiferromagnetic (AFM) ordering near 44 K for the o -HMO, irrespective to the direction of applied field.
3. The $M(T)$ measurements showed also that, the theoretically expected lock-in transition was clearly observed at around 30-35 K when magnetic field was applied along the c -axis and was undetectable along a - and b -axis.
4. The c -axis oriented o -HMO thin films on conductive Nb-doped SrTiO₃(001) substrates allowed us to perform the direct measurement of orientation-specific magnetic ordering induced “ferroelectricity” in this material. The films exhibit an

anomalous magnetic ordering around 35 K as well as an abrupt dielectric enhancement starting around 20 K and reaching maximum around 13 K along the *c*-axis.

5. Moreover, as is evident from current results displayed in *a*-axis-oriented *o*-HMO thin films, the *M-H* loop becomes clearly hysteretic when $T \sim 25$ K, indicating the origin of the observed additional magnetic ordering along the *c*-axis may be due to strain-induced canted *AFM* state instead of the commensurated lock-in transition conceived previously.
6. This primary spontaneous ferroelectricity, although coincides very well with the lock-in temperature associated with the incommensurate-commensurate magnetic ordering transition revealed by neutron diffraction and dielectric constant anomaly, is, however, estimated to be $1800 \mu\text{C}/\text{m}^2$ only when the electric field is along the *c*-axis and is smaller than the theoretically predicted values.



Biographical notes

Personal Data:

Name: Tjung-Han Lin

Sex: Male

Date of Birth: January 18, 1982

Education:

2000/09 ~ 2004/06 Fu Jen Catholic University, Taipei, Taiwan BS. degree in Physics.

2004/09 ~ 2006/06 National Chung-Cheng University, Chiayi, Taiwan MS. degree in Physics.

2006/09 ~ 2010/07 National Chiao-Tung University, Hsinchu, Taiwan Ph. D degree in Electrophysics.

Publication List:

(A) Regular paper

1. T. H. Lin*, C. C. Hsieh, H. C. Shih, C. W. Luo, T. M. Uen, K. H. Wu, J. Y. Juang, J.-Y. Lin, C.-H. Hsu, and S. J. Liu, "Anomalous magnetic ordering in *b*-axis-oriented orthorhombic HoMnO₃ thin films", Appl. Phys. Lett. **92**, 132503 (2008).
2. T. H. Lin*, H. C. Shih, C. C. Hsieh, C. W. Luo, J.-Y. Lin, J. L. Her, H. D. Yang, C.-H. Hsu, K. H. Wu, T. M. Uen, and J. Y. Juang, "Strain-induced effects on antiferromagnetic ordering and magnetocapacitance in orthorhombic HoMnO₃ thin films", J. Phys.: Condens. Matter. **21**, 026013 (2009).
3. T. H. Lin*, C. C. Hsieh, C. W. Luo, J.-Y. Lin, C. P. Sun, H. D. Yang, C.-H. Hsu, Y. H. Chu, K. H. Wu, T. M. Uen, and J. Y. Juang, "Magnetism-induced ferroelectric polarization in the *c*-axis-oriented orthorhombic HoMnO₃ thin films", J. Appl. Phys. **106**, 103923 (2009).

4. C. C. Hsieh*, T. H. Lin, H. C. Shih, C.-H. Hsu, C. W. Luo, J.-Y. Lin, K. H. Wu, T. M. Uen, and J. Y. Juang, “Magnetic ordering anisotropy in epitaxial orthorhombic multiferroic YMnO₃ films”, *J. Appl. Phys.* **104**, 103912 (2008).
5. H. C. Shih*, T. H. Lin, C. W. Luo, J.-Y. Lin, T. M. Uen, J. Y. Juang, K. H. Wu, J. M. Lee, J. M. Chen, and T. Kobayashi, “Magnetization dynamics and the Mn³⁺ *d-d* excitation of hexagonal HoMnO₃ single crystals using wavelength-tunable time-resolved femtosecond spectroscopy”, *Phys. Rev. B.* **80**, 024427 (2009).
6. C. C. Hsieh, T. H. Lin, H. W. Chang, C. W. Chang, W. C. Chang*, and C. C. Yang, “Effect of dopants on the soft magnetic properties and high frequency characteristics of FeCoBM (M= Ti, Nb, Hf, and Ta) thin films”, accepted by *Journal of Nanoscience and Nanotechnology*, (2010).

(B) Conference

7. T. H. Lin*, C. C. Hsieh, H. C. Shih, C. W. Luo, T. M. Uen, K. H. Wu, J.-Y. Lin, C.-H. Hsu, and J. Y. Juang, “Effects of compressive epitaxial strain in the *b*-axis on the magnetization response of orthorhombic HoMnO₃ thin films”, *J. Phys.: Conf. Series* **150**, 042114 (2009).
8. C. C. Hsieh*, T. H. Lin, H. C. Shih, J.-Y. Lin, C.-H. Hsu, C. W. Luo, K. H. Wu, T. M. Uen, and J. Y. Juang, “Electronic structure and magnetic anisotropies in orthorhombic multiferroic YMnO₃ thin films”, *J. Phys.: Conf. Series* **150**, 042062 (2009).
9. H. C. Shih*, T. H. Lin, C. C. Hsieh, J. M. Lee, C. W. Luo, J.-Y. Lin, T. M. Uen, J. Y. Juang, K. H. Wu, and J. M. Chen, “Ultrafast dynamics of the Mn *d-d* transition on hexagonal HoMnO₃”, *J. Phys.: Conf. Series* **150**, 042180 (2009).
10. T. Y. Tsai, T. H. Lin, S. Slowry, C. W. Luo, K. H. Wu, J.-Y. Lin, T. M. Uen, and J. Y. Juang*, “Magnetic transition anisotropies in orthorhombic LuMnO₃ and HoMnO₃ multiferroic thin films” *J. Phys.: Conf. Series* **200**, 012210 (2010).

Acknowledgements

“無為而治，則無不治。”此為余博班求學之所悟。

而此論文得以付梓，還要感謝固態實驗室研究群(莊振益 老師、溫增明 老師、吳光雄 老師、林俊源 老師、以及 羅志偉 老師)的大力支持及材料所 朱英豪 老師提供的寶貴意見。

再者，非常感謝昌學長、維仁學長、以及璨耀學長一路上不斷給予鼓勵與指導，此論文是用你們對我的關心所堆積出來的，謝謝您們！還有益「濕」益友同學：訓全，很開心在研究所的時光有你的陪伴；在實驗過程中，更要謝謝無數多的學弟妹們。我會帶著大家的友情繼續加油。

最後，僅以此論文獻給我最親愛的家人，是你們給我無憂無慮的求學生涯。在此誠摯地祝福各位平安喜樂。
-感謝老天，一旨承運；感謝師長，一直教誨；感謝父母，一路相挺。

